Dissertation
submitted to the
Combined Faculty of Mathematics, Engineering and Natural Sciences
of Heidelberg University, Germany
for the degree of
Doctor of Natural Sciences

Put forward by

M.Sc. Felix Nüßlein
born in Gunzenhausen

Oral examination: 30th April 2024

Storage ring experiments on the stability of negative ions in the gas phase

Referees:

apl. Prof. Dr. Andreas Wolf
Prof. Dr. Thomas Pfeifer

Speicherring-Experimente zur Stabilität negativer Ionen in der Gasphase

Studien an negativen Ionen (Anionen) von Molekülen und Clustern gehören zum experimentellen Kernprogramm des kryogenen Speicherrings CSR in Heidelberg. Im Rahmen dieser Arbeit wurden Entwicklungen für die nächste Generation solcher Experimente gemacht und die intrinsische Stabilität des Vinylidin-Anions H_2CC^- im elektronischen und Vibrations-Grundzustand wurde untersucht. Die experimentellen Entwicklungen umfassen einen neuen Ionenquellen-Aufbau für Experimente zur Stabilität kalter Cluster-Anionen (z.B. Al_4^-), einen elektrostatischen Strahlführungs-Aufbau zur effizienten und flexiblen Versorgung des CSR mit Strahlen verschiedener Ionenquellen, sowie Verbesserungen an diagnostischen Methoden zur empfindlichen und genauen Charakterisierung des Ionenertrages von Ionenquellen. Für die Vinylidin-Studie speicherten wir H_2CC^--Ionen für bis zu 3300 s in der kalten (< 10 K) Vakuum-Umgebung des CSR ($\sim 10^3$ cm^{-3} Restgasdichte) und verfolgten die Zeitabhängigkeit der Anzahl gespeicherter Ionen mit Hilfe von Photodetachment. Intrinsisch stabile isobare Ionen (CN^-), die als Referenz gleichzeitig gespeichert und beobachtet wurden, erlaubten es uns, eine effektive H_2CC^--Lebensdauer von $\gtrsim 10^4$ s zu bestimmen. Diese Lebensdauer ist um einen Faktor $\gtrsim 100$ größer als die von einem anderen Speicherring-Experiment bei Raumtemperatur gemessene Lebensdauer. Basierend auf unseren Ergebnissen vermuten wir, dass diese Diskrepanz von Photodetachment von H_2CC^- durch das Schwarzkörper-Strahlungsfeld des Raumtemperatur-Experimentes herrührt.

Storage ring experiments on the stability of negative ions in the gas phase

Studies on negative ions (anions) of molecules and clusters are one of the core experimental programs at the Heidelberg Cryogenic Storage Ring (CSR) facility. Within this work developments for the next generation of such experiments have been undertaken and the intrinsic stability of the vinylidene anion H_2CC^- in its electronic and vibrational ground state has been studied. The experimental developments include a new ion source setup for stability experiments on cold anionic clusters such as Al_4^-, an electrostatic beamline setup for efficiently and flexibly supplying the CSR with beams of various ion sources, and improvements on diagnostic methods allowing to characterize the output of ion sources with high sensitivity and precision. For the vinylidene study, we stored H_2CC^- ions for up to 3300 s in the radiatively cold (< 10 K) and ultrahigh-vacuum (rest gas density $\sim 10^3$ cm^{-3}) environment of the CSR, and tracked their time-dependent abundance in the storage ring using photodetachment. By means of intrinsically stable isobaric ions (CN^-), stored and monitored at the same time as reference, we found an effective H_2CC^- lifetime of $\gtrsim 10^4$ s. This lifetime is a factor $\gtrsim 100$ larger than the H_2CC^- lifetime reported by a room-temperature storage ring experiment. Based on our results, we assume that this discrepancy results from photodetachment of H_2CC^- by blackbody radiation in the room-temperature experiment.

Contents

List of Figures

List of Tables

Acronyms

CED Collisional Electron Detachment
COMPACT Cold Movable Particle Counter
CSR Cryogenic Storage Ring
CSR-ReMi CSR Reaction Microscope

DAQ Data AcQuisition

EA Electron Affinity

ISO-ToF Isochronous Time-of-Flight
ISTB Ion Source Test Bench

LPD Laser Pulse Delay
LVAP Laser VAPorization

MCP MicroChannel Plate
MISS Metal Ion Sputter Source
MR-ToF Multi-Reflection Time-of-Flight

Nd:YAG Neodymium-Doped Yttrium Aluminum Garnet
NICE Neutral Imaging in Cold Environment

OD Opening Duration
OPO Optical Parametric Oscillator

PES PhotoElectron Spectroscopy

RTE Room-Temperature Equivalent

SNR Signal-to-Noise Ratio

ToF Time-of-Flight

UV	UltraViolet laser
VIS	VISible laser

Chapter 1

Anions in the gas phase

Negative ions (anions) play an important role in space and on Earth. For instance, anionic hydrogen H^- is the most important educt for the formation of H_2 present in interstellar gas clouds. Furthermore, H^- dominates the visible opacity of stars, including the Sun (Millar, Walsh, and Field 2017). Anions are also relevant for the chemistry happening in the ionosphere of Earth (Pegg 2004). In the field of nuclear fusion, strong beams of anions are neutralized efficiently and subsequently injected into the fusion reactor for heating and current drive (Fantz et al. 2007). In accelerator-based analysis of samples for rare isotopes, production of anionic beams from the sample and subsequent conversion to positive ion beams help to remove unwanted contaminant species (Fifield 1999). Anions are also relevant for industrial applications, where they play a role in plasma etching (Pegg 2004).

In this chapter, we give a short overview of anions in the gas phase. We discuss how they form and give criteria for their observed stability (section 1.1). We then describe how they can be destroyed (section 1.2). Lastly, we introduce experimental methods for studying anions in the gas phase and conclude with a recent experimental example (section 1.3).

1.1 Formation and stability of anions

Anions form by attachment of an extra electron to an atom or molecule. The energy by which the extra electron is bound is called Electron Affinity (EA) and defined as the energy difference between the anion and the neutral:

$$\mathrm{EA} = E(\mathrm{neutral}) - E(\mathrm{anion}) \tag{1.1}$$

For $\mathrm{EA} > 0$ the anion lies energetically below the neutral and is considered to be intrinsically stable (Rienstra-Kiracofe et al. 2002). If at all, a particle with $\mathrm{EA} < 0$ supports a bound electron only temporarily, as is for instance the case for the metastable He^- ion (Pedersen et al. 2001).

Assuming that prior to the attachment process to the neutral the incident electron has the kinetic energy E_e, the total energy $E_e + \mathrm{EA}$ is released during its capture. This energy can either be dissipated radiatively by means of a photon (radiative attachment) or by collision with a third body participating in the attachment process, i.e., another neutral or charged particle. In the case of molecules the excess energy may also be dissipated by breaking up the bond between the molecular constituents (dissociative attachment). For laboratory gas-phase experiments with anions, so-called ion sources employ these attachment mechanisms combined with dedicated technical methods in order to produce anions from solid, liquid or gaseous educts (Duncan 2012; Kebarle and Verkerk 2009; Middleton 1989).

The observed lifetime of an anion in the gas phase is not only dependent on its intrinsic stability, but also on its environment. For instance, if the electron is only weakly bound, it may already be detached at room temperature by absorption of infrared photons from the ambient blackbody radiation field (Müll et al. 2021). Also, the observed anion lifetime is limited by the residual gas density of its environment, as it can lose its electron after collision with a residual gas particle. The presence of an external electrical field can also reduce the observed anion lifetime (Pegg 2004). In order to increase the observed lifetime and enable experiments in laboratory environments, it is thus advisable to reduce the vacuum pressure as far as possible, to suppress the blackbody radiation, and to conduct experiments in field-free areas (Hahn et al. 2016).

1.2 Decay of anions

The processes by which anions decay are essentially the inverse of the formation processes outlined in the previous section 1.1. The anion emits its excess electron after having absorbed an amount of energy above a threshold energy E_{th}. The necessary energy may be delivered by a photon (photodetachment), or a collision with a third body. In addition to electron detachment, molecular anions may also decay by dissociation.

The electron detachment efficiency and its energy dependence are quantified by the cross section parameter. Single electron detachment cross sections commence at zero

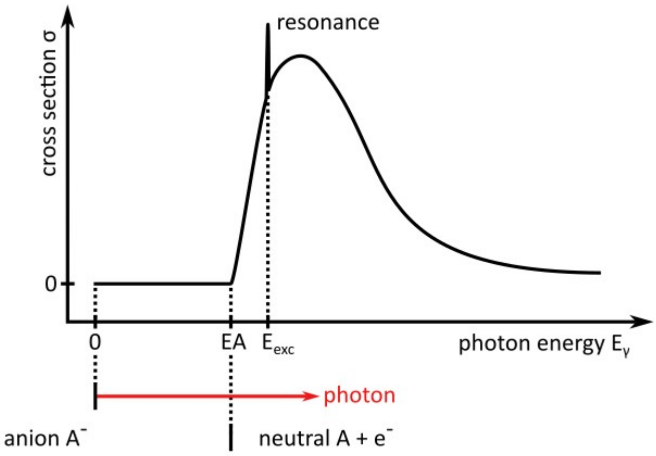

Figure 1.1: Schematic of a typical non-resonant photodetachment cross section. In addition, a resonance peak at the energy E_{exc} of an excited state above the photodetachment threshold (EA) is depicted.

at the threshold energy, rise until they culminate in a maximum, and decrease again monotonically (Pegg 2004).

A typical non-resonant single-electron detachment cross section is sketched in figure 1.1 for the case of photodetachment. Here, the threshold energy $E_{\mathrm{th}} = \mathrm{EA}$ is the electron affinity. The energy dependence of the photodetachment cross section σ near the threshold is described by the Wigner law

$$\sigma(E_\gamma) \propto (E_\gamma - \mathrm{EA})^{l+1/2}, \tag{1.2}$$

where E_γ is the energy of the incoming photon and l is the angular momentum of the emitted electron (Pegg 2004). For $l = 0$, the Wigner law simplifies to

$$\sigma(E_\gamma) \propto \sqrt{E_\gamma - \mathrm{EA}}. \tag{1.3}$$

Above E_{th}, non-resonant detachment is not the only possible detachment channel. The electron may also be detached after resonant excitation of the anion, e.g., to an excited electronic or vibrational state (DeVine et al. 2018; Pegg 2004). In addition to the non-resonant cross section, a resonance manifests itself in the observed cross section as narrow peak at the excited state energy (e.g., E_{exc} in figure 1.1). The excited state decays spontaneously by means of autodetachment.

As mentioned in section 1.1, collisional electron detachment after collision with particles of the residual gas is another decay process relevant for the observed lifetime of anions in laboratory vacuum environments. Abbreviated as CED, it is especially relevant when the anions are accelerated to high kinetic energies, as is the case for experiments on fast beams of anions (Hahn et al. 2016). In contrast to the photodetachment cross section, the threshold behaviour for this process is not well understood

(Pegg 2004). The CED cross section not only depends on the kinetic energy of the projectile anion and the target gas particle, but also on the respective species (Hernández and Hinojosa 2018; Jalbert et al. 2014). For gas-phase anion experiments, the gases most relevant as targets are N_2, O_2 and H_2 (Cox 2002; Hahn et al. 2016). Experimentally, the CED cross section thus has to be determined as a function of the kinetic energy of the anion of interest and individually for each target gas (Hernández and Hinojosa 2018; Jalbert et al. 2014).

1.3 Experiments with anions

Most experiments on gas-phase anions investigate their structure and dynamics by destroying them. Due to the high resolution and the availability of photons within a broad spectral range, photodetachment is the preferred means of anion destruction (Pegg 2004). Apart from the photodetachment cross section, photodetachment experiments allow to measure the electron affinity (DeVine et al. 2017), the lifetime of metastable states (Müll et al. 2021), and to observe the internal dynamics of molecules interacting radiatively with their environment (Meyer et al. 2017). Furthermore, photodetachment-based experiments allow to infer information about the structure and stability of molecules (DeVine et al. 2017).

One way to study anions in the laboratory is to confine them locally in a vacuum by means of electric or magnetic fields, and to overlap them with a beam of photons, which is usually provided by a laser. The experimental signal is obtained by collecting the emitted electron, the resulting neutral, or both. If required, state-specific information is obtained by variation of the photon energy.

As anion numbers and their photodetachment cross sections are typically very small, the efficiency can be increased by means of detectors capable of counting single particles. Photodetached electrons can be collected with high efficiency, as they are light compared to the neutrals and may be directed easily by means of weak electric and magnetic fields. Using fast anion beams for photodetachment allows to efficiently collect the resulting neutrals within a small solid angle downstream of the ion-photon interaction region. When compared to simple crossed-beam experiments, multi-pass experiments allow to study anion numbers and cross sections orders of magnitude smaller, as the ion beam passes through the interaction region many times. One class of multi-pass experiments are storage rings, where the anion beam revolves on a closed orbit (Pegg 2004). The continuous recycling (see chapter 3) allows to monitor the time evolution of the state populations in the stored anion ensemble. For instance, metastable states decay (Müll et al. 2021), and anions of molecules may equilibrate radiatively with their environment (Schmidt et al. 2017).

In addition to the photodetachment signal, the detector downstream of the interaction region acquires noise in the form of neutrals due to CED of fast anions. One way to improve the Signal-to-Noise Ratio (SNR) is to enhance the signal by increasing the photon density in the interaction region. This is achieved by means of pulsed lasers, which deliver short ($\leq$ ns) photon pulses with photon densities orders of magnitude higher than continuous-wave lasers. Neutral photodetachment events are then only expected within short time windows on the order of the laser pulse duration. At the same time the high photon density leads to a strongly increased instantaneous photodetachment event rate within these windows (Pegg 2004).

Another way for improving the SNR is to suppress the absolute CED-induced noise by reducing the residual gas density. One way to achieve this is by cooling the chambers of the experimental apparatus to very low temperatures (possibly down to ~ 4 K). This is done by the CSR (Hahn et al. 2016) discussed in chapter 3. Most components of the residual gas then freeze out at the chamber walls. As a result, the residual gas density reduces by orders of magnitude. Due to the reduced overall CED-induced losses, the observed lifetime of the stored anions increases drastically to up to several thousand seconds (Hahn et al. 2016). This allows to study slow processes, e.g., the cooling of molecular rotations (Meyer et al. 2017) or the decay of very long-lived metastable states (Müll et al. 2021).

A recent example for a photodetachment experiment on gas-phase anions is the work by Müll 2023, which studied the cooling behavior of isolated molecular systems stored over long timescales in a cryogenic electrostatic storage ring. Ensembles of internally hot negative aluminum clusters were exposed to a radiatively cold and ultra-high vacuum environment for up to 2000 s. During exposure, the internal energy distribution of the cluster ensemble was interrogated by means of photodetachment. The observed radiative cooling behaviour of the clusters, which prevailed even at the longest exposure times, was interpreted to be the result of a statistical process known as internal vibrational redistribution. The study for the first time demonstrated that this process plays a role for the cooling of isolated molecular systems on timescales orders of magnitude higher than previously known (Bull et al. 2019; Makarov, Malinovsky, and Ryabov 2012; Stockett et al. 2020). In chapter 3 we present experimental developments made with the goal to enable further studies on negative aluminum clusters.

Chapter 2

Vinylidene stability and isomerization

In this chapter we introduce the vinylidene molecule H_2CC and its role in chemical physics research on molecular stability and isomerization (section 2.1). Discussing experimental studies on the vinylidene anion H_2CC^-, we give an overview of the current state of knowledge on the vinylidene stability (section 2.2). Finally, we motivate a H_2CC^- stability experiment (section 2.3), which employs a cryogenic electrostatic storage ring and is presented in chapter 4.

2.1 The vinylidene molecule

The vinylidene molecule is an isomer of acetylene. Both molecules have the sum formula C_2H_2, but differ with respect to the position of a single hydrogen atom. Acetylene is arranged linearly (denoted HCCH). For vinylidene, both hydrogen atoms are attached to one of the carbon atoms (denoted H_2CC). While acetylene was detected in space (Ridgway et al. 1976) and plays an important role in combustion technology (Singh et al. 2021), vinylidene is of interest as an intermediate in chemical reactions (Laufer 1980; Skell, Villaume, and Fagone 1972). Furthermore, from the view of chemical physics vinylidene is interesting because it isomerizes to acetylene via migration of one of the hydrogen atoms, which is referred to as 1,2-hydrogen shift (Schaefer 1979). As vinylidene is structurally not too complex, it serves as a model system for studying this process (DeVine et al. 2017; Jensen, Pedersen, and Andersen 2000; Li et al. 2017).

A schematic energy diagram of the hydrogen migration process is depicted in figure 2.1. The scheme is partly based on quantum chemical calculations performed by

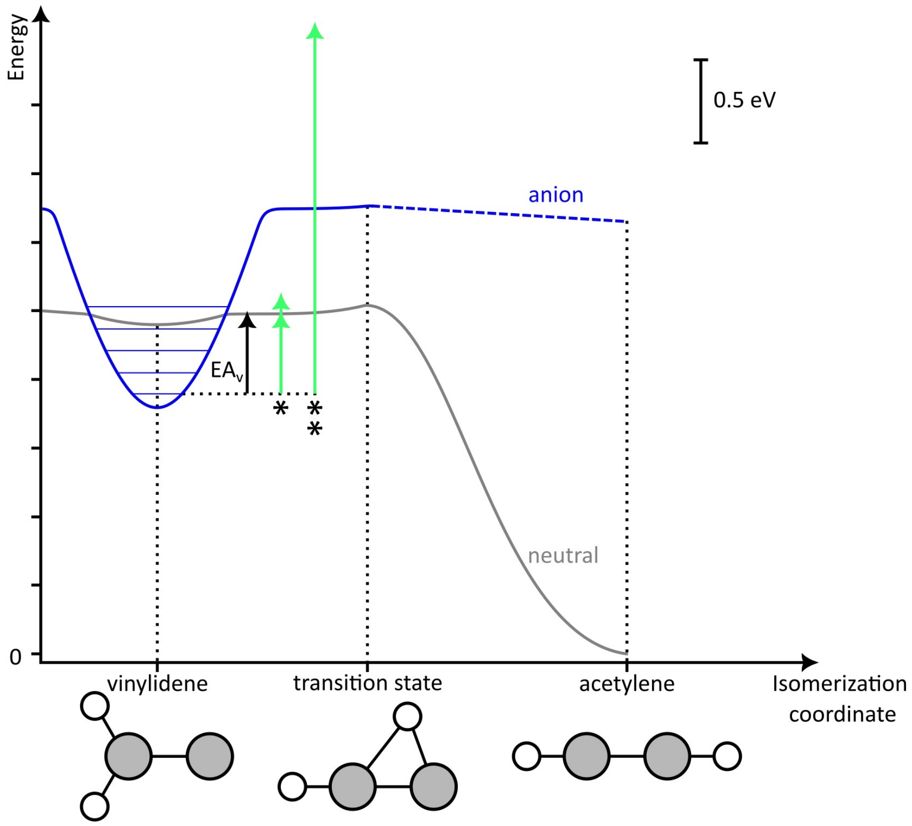

Figure 2.1: Schematic one-dimensional potential energy surfaces of the vinylidene-acetylene system for the anion (blue) and the neutral (gray). The isomerization coordinate corresponds to the migration of a hydrogen atom from one carbon atom to the other. The states in the well of the blue curve symbolize the vibrational states of the CH_2 rocking mode (ν_6) of H_2CC^-. The electron affinity EA_v of vinylidene is depicted as black arrow. The green arrows indicate photodetachment close to ($*$) and far away ($**$) from the EA.

a collaborator (Miliordos 2023). It has been complemented by information on energies available from various other experimental and theoretical studies as cited in the text. We first discuss the neutral C_2H_2 vinylidene configuration, which lies about 1.9 eV above the acetylene configuration. A shallow barrier (≈ 0.13 eV) appears to stabilize vinylidene against rearrangement to acetylene (DeVine et al. 2017) via a transition state for which one of the hydrogen atoms migrates. With the fact in mind that the thermal energy at room temperature ($T = 300$ K) is about $k_B T \approx 26$ eV, it already seems possible that absorption of infrared photons from the ambient blackbody radiation field excite vinylidene enough to initiate isomerization to acetylene, for instance by means of vibrational excitation.

For the anionic molecular configuration the situation looks rather different: The negative acetylene $HCCH^-$ lies energetically higher than its neutral counterpart, and can thus not support a bound electron. In fact, the electronic state of the anion,

Table 2.1: Harmonic frequencies of the H_2CC^- normal vibrational modes as calculated by Guo et al. 2015.

Normal mode	ν_1	ν_2	ν_3	ν_4	ν_5	ν_6
Harmonic frequency (cm^{-1})	2865.9	1502.0	1335.2	764.9	2837.8	876.5

when lying above that of the neutral, is expected to be highly unstable and is in fact better considered as an electron scattering resonance in the neutral molecular structure (e.g. Dressler and Allan 1987). For the anionic vinylidene H_2CC^-, which lies energetically below the vinylidene neutral, the electron is bound by about 0.5 eV (arrow with EA_v in figure 2.1). This seems to be a sufficiently high barrier for stability at room temperature and against isomerization. However, H_2CC^- energetically still lies above the neutral acetylene. In principle, a reaction pathway to neutral HCCH could exist, where tunneling of one hydrogen atom and emission of the electron are involved. This makes H_2CC^- a candidate for a metastable negative ion.

As a molecule with $N_c = 4$ constituents arranged in a non-linear configuration, vinylidene has $3N_c - 6 = 6$ normal vibrational modes (Demtröder 2021). A depiction of these modes can be found, e.g., in Guo et al. 2015. The individual vibrational modes are called CH symmetry stretching (ν_1), CC stretching (ν_2), CH_2 scissors (ν_3), out-of-plane (ν_4), CH asymmetry stretching (ν_5) and CH_2 rock (ν_6). For all modes except for ν_4, the motion of the constituents takes place within the molecular plane (Guo et al. 2015). Calculated values for the harmonic frequencies of these modes are given in table 2.1. Some thermal excitation may play a role, as the frequencies are still comparable to k_BT for 300 K, corresponding to $k_BT/hc = 209$ cm^{-1}. Literature sources relate vinylidene rearrangement by hydrogen migration to the excitation along ν_6, i.e., the CH_2 rocking mode (DeVine et al. 2017; Issler, Mitrić, and Petersen 2023).

While most experimental studies concentrate on the reaction pathway between the neutral isomers in various vibrational excitations (e.g., DeVine et al. 2017; Ervin, Ho, and Lineberger 1989; Levin et al. 1998), there is so far only one experiment interested in the stability of the vinylidene anion in the vibrational ground state. In the next section 2.2 we outline the current level of knowledge on the neutral and anionic vinylidene stability by means of experiments employing the vinylidene anion H_2CC^-.

2.2 Vinylidene anion stability experiments

Experiments investigating the vinylidene anion H_2CC^- may be divided into two groups: The first group of studies focuses on timescales $\ll 1$ s and is mostly interested in deriving properties of the neutral vinylidene. The second group investigates H_2CC^- on timescales $\gg 1$ s and there is in fact so far just a single experiment of this type (Jensen, Pedersen, and Andersen 2000). This type of studies is interested in the stability of H_2CC^- in its vibrational and electronic ground state. In the following, we give an overview of experiments from the first group, and their findings in combination with theory. We then introduce the single, long-timescale experiment of Jensen, Pedersen, and Andersen 2000 and discuss its implications with the current state of knowledge in mind. Based on that, we motivate a new, complementary study which would clarify the open questions.

Experimentally, the vinylidene anion was mostly investigated by means of Photo-Electron Spectroscopy (PES). This technique employs photodetachment of electrons from an ensemble of H_2CC^- ions by means of fixed-energy photons

$$\mathrm{H_2CC^-} + \gamma \longrightarrow \mathrm{H_2CC} + e^- \tag{2.1}$$

in combination with a measurement of the kinetic energy spectrum of the emitted electrons. These electrons serve as probes for the potential energy surface of the neutral molecule in the final channel and deliver information about its vibrational and electronic levels as well as its structure and stability (Ervin, Ho, and Lineberger 1989). If the electron is not emitted directly, but via an intermediate state accessed by photoexcitation, PES can additionally give hints about the reaction pathway between the anion and the neutral (DeVine et al. 2018; Gerardi et al. 2010).

Compared to early PES (e.g., Ervin, Ho, and Lineberger 1989), modern methods increase the amount of collected information by additionally varying the photon energy. In addition, they enhance the effective resolution of the electron spectrometer by improved methods related to the extraction and detection of the photodetached electrons (Cavanagh et al. 2007; Osterwalder et al. 2004). Also, anion samples are now prepared in a more defined way. For instance, confinement in cold (5 K) and buffer-gas-cooled ion traps quenches rotational and vibrational excited state populations of the trapped ion ensemble. The quenching suppresses spectral features such as rotational line broadening or vibrational hot bands, thereby improving the spectral quality (Hock et al. 2012; Weichman and Neumark 2018).

Based on photoelectron spectra from early room-temperature PES experiments on rotationally and vibrationally thermalized H_2CC^- it was assumed at first that the neutral vinylidene isomerizes to acetylene on femtosecond timescales (Ervin, Ho, and Lineberger 1989). However, a complementary (non-PES) experimental study, which allowed a more direct access to the vinylidene structure by a method known as Coulomb explosion imaging, observed the neutral C_2H_2 in the vinylidene configuration even 3.5 µs after photodetachment of H_2CC^- (Levin et al. 1998). More recent PES studies, incorporating the experimental improvements outlined above, did not observe the spectral features on which Ervin, Ho, and Lineberger 1989 had based their lifetime estimate (DeVine et al. 2017, 2016). All these results are conciliated by theory, according to which the neutral vinylidene in its vibrational ground state is expected to have a lifetime of several hundred picoseconds, while higher vibrational states isomerize to HCCH on a femtosecond timescale (Guo et al. 2015; Schork and Köppel 2001; Zou, Bowman, and Brown 2003). If the vibrational excitation is strong enough, the molecular configuration may even oscillate between acetylene and vinylidene. This explains why in the experiment of Levin et al. 1998 C_2H_2 was still found in the vinylidene configuration after 3.5 µs (Hayes et al. 2001).

As mentioned above, photoelectron spectra may also yield information about the reaction pathway between anion and neutral: Using photons with energies rather close to the detachment threshold of H_2CC^- (symbolized by green arrows marked with $*$ in figure 2.1), Gerardi et al. 2010 and DeVine et al. 2018 reported photodetachment of H_2CC^- via an intermediate state, which they suspected to be a vibrationally excited state of H_2CC^- accessed by photoexcitation:

$$H_2CC^- + \gamma \longrightarrow H_2CC^{-*} \longrightarrow H_2CC + e^- \tag{2.2}$$

DeVine et al. 2018 attributed the features to autodetachment from vibrationally excited states of H_2CC^-. The results of both of these experimental studies motivated Issler, Mitrić, and Petersen 2023 to simulate the dynamics of this process on timescales up to 3000 fs after excitation of H_2CC^- along two specific vibrational modes (ν_2 and ν_5). Apart from a non-adiabatic electron detachment process, their simulation also suggested the involvement of adiabatic electron detachment from vinylidene in a T-shaped geometrical configuration, which may be accomplished by excitation along the ν_6 vibrational mode. Issler, Mitrić, and Petersen 2023 hint at a connection to isomerization, as the T-shaped vinylidene geometry is considered to be the initial stage of rearrangement to the linear acetylene (Hayes et al. 2001).

Among studies using the negative vinylidene ion, the stability experiment by Jensen, Pedersen, and Andersen 2000 stands out: As mentioned, H_2CC^- lies above the neutral acetylene (see figure 2.1), but (in its ground vibrational state) is stable against isomerization to acetylene by a ~ 0.5 eV barrier. Hence, it may be considered metastable, and thus have a finite intrinsic lifetime. Only rather summary statements about the real stability of this ion appear to exist in the literature until the turn of the century[1]. Motivated by this open situation, Jensen, Pedersen, and Andersen 2000 posed the question whether on a long timescale H_2CC^- may spontaneously emit its electron in a process involving the isomerization itself, i.e., rearrangement from H_2CC to the

---

[1] See a discussion in Sec II B 1 of Ervin, Ho, and Lineberger 1989 and their reference 23.

linear acetylene HCCH by the migration of a single hydrogen atom. Based on theoretical calculations (Frenking 1983), they suspected that the isomerization process may not necessarily involve a planar motion of the hydrogen atom. It is to be noted here that Jensen, Pedersen, and Andersen 2000 did not speculate whether the electron is emitted prior to or after isomerization to the acetylene configuration.

In their experiment Jensen, Pedersen, and Andersen 2000 stored a beam of electronic and vibrational ground state vinylidene anions in a room-temperature electrostatic storage ring. Trapped on a closed orbit, the ions could be observed for several seconds. While stored, they could decay due to only few processes, including the loss process related to the suspected intrinsic H_2CC^- lifetime. The decay rate due to the intrinsic vinylidene lifetime was derived from the decaying ion beam intensity, corrected for the other loss processes. Instead of employing the electron for probing the neutral vinylidene structure as the PES experiments, they observed the vinylidene anion over the longest time scales possible at that time (~ 10 s), and extended the experimentally explored timescale to up to ~ 100 s by means of calibration measurements. The following loss processes have to be considered:

(**a**) In the employed room temperature storage ring, Collisional Electron Detachment (CED) with the residual gas at a pressure of $\sim 10^{-11}$ mbar was the dominant loss process, limiting the storage time to ~ 10 s.

(**b**) Various intrinsic losses due to the storage ring principle, e.g., intra-beam scattering, tune shifts, or electric field imperfections.

(**c**) Photodetachment by infrared photons of the ambient blackbody radiation.

Jensen, Pedersen, and Andersen 2000 thus eliminated the pressure factor (point **a**) using a calibration measurement: They recorded the observed decay rate of the H_2CC^- ion beam as a function of the pressure in the vacuum chambers of the ring, which they manipulated by letting in small amounts of H_2 gas. By means of linear extrapolation to zero pressure they obtained the CED-free H_2CC^- decay rate.

To take care of the systematic storage ring effects (**b**), their second trick was to determine the CED-free decay rate for an intrinsically stable ion of similar mass (O^-, $m = 16$ u), which they assumed to be subject to the same systematic storage ring effects. Comparison of the extrapolated CED-free rates of H_2CC^- and the reference ion then yielded an effective H_2CC^- decay rate of $k_0 = (0.009 \pm 0.006)\ \mathrm{s}^{-1}$, which corresponds to a lifetime of $\tau_0 = 1/k_0 = 110^{+180}_{-40}$ s. As they estimated the influence of the blackbody-induced decay rate to be negligible ($< 0.001\ \mathrm{s}^{-1}$, **c**), they attributed τ_0 to the intrinsic lifetime of the ground state vinylidene anion.

With their study, Jensen, Pedersen, and Andersen 2000 had hoped to trigger further theoretical work for explaining this long lifetime. They outlined how this may be done using quantum mechanical calculations: To determine a theoretical lifetime value for H_2CC^- in its vibrational and electronic ground state, the reaction pathway from

H_2CC^- to the linear HCCH has to be determined. This requires knowledge of the relevant parts of the anionic and neutral potential energy surfaces.

While, also thanks to PES, the knowledge of the potential energy surfaces has increased steadily (DeVine et al. 2017, 2018; Guo et al. 2015; Han, Li, and Guo 2014), the question on the reaction pathway from H_2CC^- to the linear HCCH is only partially addressed in later literature. Among the accessible publications citing the work of Jensen, Pedersen, and Andersen 2000, we find three works commenting or providing information on the reaction pathway:

- Based on calculations, Glendening and Strange 2002 suggest that the electron is emitted prior to isomerization, but no detailed rate calculations are given.
- With reference to calculations by Chandrasekhar, Kahn, and Ragué Schleyer 1982 on the preferred structure of an anion with sum formula $C_2H_2^-$, Jochim et al. 2019 state in few words that H_2CC^- loses its electron adiabatically and subsequently isomerizes to HCCH. However, no detailed pathway for the inferred adiabatic electron loss process is indicated.
- Finally, there is the above-outlined recent work by Issler, Mitrić, and Petersen 2023 which suggests that, after excitation along specific vibrational modes, H_2CC^- autodetaches its electron adiabatically on femtosecond timescales. Yet, the work does not offer an explanation of the finite intrinsic decay rate from the experiment of Jensen, Pedersen, and Andersen 2000.

At this point, the intrinsic lifetime of the ground-state vinylidene anion appears unclear. Considering the extended range of storage lifetime, improved environmental control, and studies available with newly emerging experimental techniques, more studies are clearly desirable.

2.3 Complementary study on the vinylidene anion stability

Given the open questions from the room-temperature storage ring study by Jensen, Pedersen, and Andersen 2000, and the advances in the storage ring technology since then, we here carry out a new measurement where following points were improved or newly addressed:

(**A**) Intrinsic storage ring losses are not mass-independent, e.g., due to different sensitivity to electric field imperfections. Since the reference ion mass in the previous experiment was $m = 16$ u, such uncertainties can be reduced by using a reference ion closer in mass to the H_2CC^- ion ($m = 26$ u).

(**B**) Also, H_2CC^- and the reference ion were stored subsequently, which involved altering the initial storage conditions by changing the settings of the magnet selecting the ion species from the ion source. In principle this may result in different measured decay rates for the same ion species and storage ring settings. In a new measurement, this effect can be eliminated by storing H_2CC^- and the reference ion at the same time.

(**C**) In Jensen, Pedersen, and Andersen 2000, the influence of the thermal radiation field was only estimated theoretically and not measured by repeating the experiment with significantly suppressed radiation field, e.g., by cooling the ring chambers to liquid-helium temperatures (~ 4 K). Jensen, Pedersen, and Andersen 2000 only cooled their ring to 260 K for extending the pressure-limited direct observation time range. Before comparison to the reference-ion storage time, they measured a (35 ± 3) s lifetime of H_2CC^- in the storage ring.

(**D**) Even though prior to the experiment, Jensen, Pedersen, and Andersen 2000 exhausted the diagnostic potential available at that time[2] (Seiersen 2003), they did not give direct proof that the ions stored at the very time of the experiment were in fact H_2CC^-. Their selecting magnet could not resolve ion species with the same mass, but different composition (isobars). In addition, they themselves observed that under H_2CC^- production settings the ion source is as well capable of producing other isobaric species (Seiersen 2003). For instance, the ion CN^- ($m = 26$ u) may be commonly produced along with H_2CC^- by leaking a small amount of atmospheric air into the source, as we will demonstrate later in chapter 4.

Since the year 2000 electrostatic storage ring technology has improved to the extent that they may now be operated at cryogenic temperatures < 10 K, which dramatically reduces the thermal radiation field and the particle density within their vacuum chambers, thereby increasing the direct observation time range of stored ions up to several 10^3 s. The indirectly measured lifetime of 110 s from the previous experiment can now be observed and confirmed directly (Brandenstein et al. 2023; Hahn et al. 2016; Nakano et al. 2017; Schmidt et al. 2013). With the Cryogenic Storage Ring (CSR) at the Max-Planck-Institut für Kernphysik in Heidelberg we have such a machine in operation. As we will outline later in section 3.2.4, it is the first electrostatic storage ring which can also be operated as a high-resolution mass spectrometer capable of resolving isobaric contaminants in the stored ion beams (Grieser et al. 2022).

Motivated by the yet unexplained result and the critical points of the room-temperature study by Jensen, Pedersen, and Andersen 2000, by the outlined theoretical implications of a reaction pathway from the ground state H_2CC^- to the neutral HCCH, and lastly by the experimental possibilities we have now in hand for studying gas-phase anions

---

[2] Suitable high-resolution mass spectrometry techniques were not yet available (Plaß, Dickel, and Scheidenberger 2013).

by means of the CSR, a complementary study of the intrinsic stability of the ground state H_2CC^- appears particularly attractive within the topic of this thesis. We will present the experimental idea and the results in chapter 4, while the following chapter 3 first considers the cryogenic storage ring CSR and the development of its versatility for negative-ion studies in general.

Chapter 3

Experimental developments

This chapter first addresses the possibilities for experiments with negative gas-phase ions in the Cryogenic Storage Ring (CSR) setup. We then present practical developments made in the context of this thesis with the goal to expand and enhance these opportunities, and give ideas for further improvements.

3.1 The CSR as a tool for studying anions in the gas phase

Motivated by the crucial role of negative ions for physical and chemical processes happening on Earth and in space, researchers around the world build small- and large-scale laboratory setups dedicated to studying the properties of gas-phase anions. The most state-of-the-art experiments, ultracold ultrahigh-vacuum devices, employ quasi-static or static electrical fields for trapping ions almost at rest, or storing them at high velocities on closed orbits (Geistlinger et al. 2021; Nakano et al. 2017; Schmidt et al. 2013).

As one of the latter experiments, the Cryogenic Storage Ring (CSR) at the Max-Planck-Institut für Kernphysik in Heidelberg investigates the interactions of fast beams of atomic and molecular ions with beams of electrons, photons or neutral particles in the gas phase. Among few other storage ring experiments (Brandenstein et al. 2023; Hahn et al. 2016; Nakano et al. 2017; Schmidt et al. 2013), the CSR provides experimental conditions comparable to the environment found in interstellar space: The extremely low gas density allows to observe fast-moving ions over timescales up to hours (Hahn et al. 2016). Furthermore, the low radiation field background lets infrared-active molecular

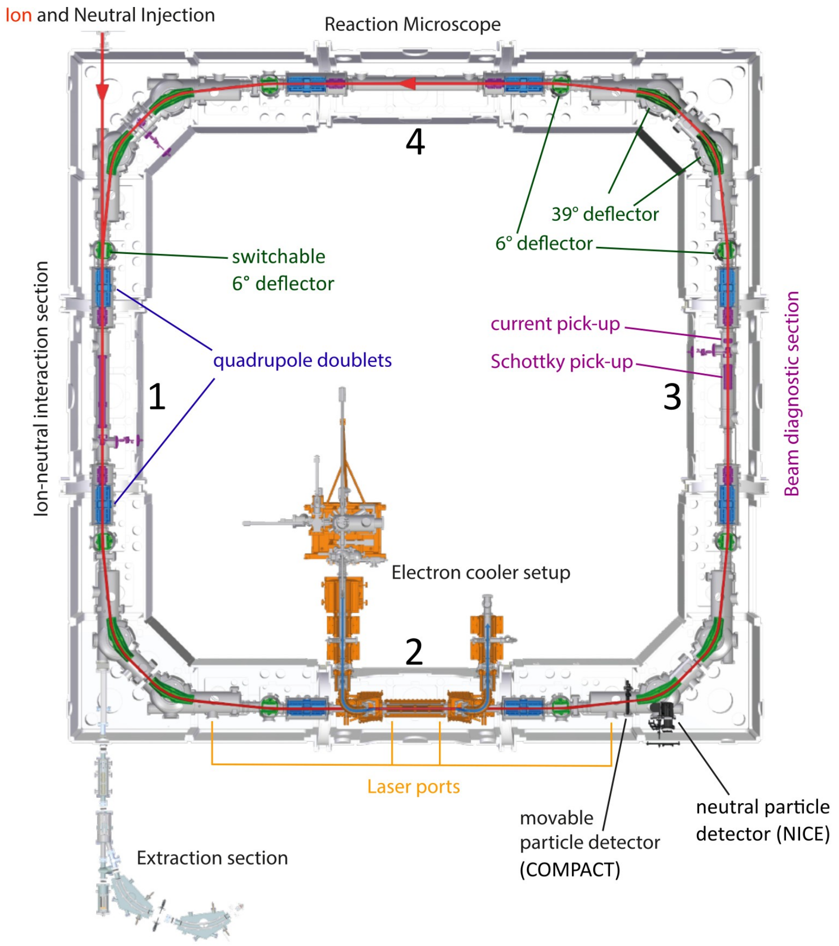

Figure 3.1: Sectional top view of the cryogenic storage ring CSR. The linear sections are numbered with respect to the injection. Figure adapted from Müll 2023.

ions radiatively relax to low internal states (Kálosi et al. 2022; Meyer et al. 2017; O'Connor et al. 2016), thereby creating defined conditions for physical interactions and chemical reactions. As a large-scale facility, the CSR houses several different types of experiments involving in particular collisional and laser interactions of the stored ions. (Hahn et al. 2016).

In the following we introduce the CSR facility in more detail and commit to its experimental capabilities for studying anions in the gas phase. The CSR setup is depicted in figure 3.1. The extremely good vacuum with down to ~ 100 cm^{-3} residual gas density is achieved with a double-walled vacuum chamber design and, after pumping with standard high-vacuum pumps, by cooling the inner vacuum chambers down to the temperature of liquid helium (~ 4 K), thereby freezing out most components of the residual gas at the chamber walls. Furthermore, the low chamber temperatures strongly suppress the ambient blackbody radiation (Hahn et al. 2016).

By means of static voltages applied to the ion-optical elements the ion beam is confined to and revolved on a closed orbit. Each corner section of the CSR features identical sets of ion deflectors with a total deflection angle of 90°, and quadrupole doublets for ion focusing. The fully electrostatic design allows to store ions at given energy independently of their mass-to-charge ratio. The four linear sections provide space for experiments undisturbed by the deflecting and focusing electrical fields (Hahn et al. 2016).

The first linear section accomodates a setup for studying collisions between cold molecular ions and a dilute target of neutral atoms. To this end, stored molecular ions are overlapped with a beam of neutrals at defined relative collision energies. Detectors further downstream in the linear section and the extraction beamline collect neutral and charged reaction products. The incident neutral beam results from atomic anions photodetached by a strong infrared laser further upstream in the transfer beamline (see figure 3.2). So far, the setup was employed to study astrochemically relevant reactions between neutrals and molecular cations (Grussie et al. 2022). In principle, it may also be used for investigating collisions between neutrals and molecular anions, which then decay by the process of associative detachment (Hassan et al. 2022; Jerosimić, Gianturco, and Wester 2018).

The second linear section houses a laser setup. Here, the stored anion beams are brought together with pulsed and continuous-wave laser beams at different overlap angles in order to induce photodetachment or fragmentation. Fast and efficient single-particle detectors further downstream collect neutral (NICE, see Becker 2016) or charged products (COMPACT, see Spruck et al. 2015) of these processes. Coincident operation of the detectors allows to distinguish photodetachment from fragmention. Together with a proper choice of photon energies, these methods yield information about the states populated in the stored anion ensemble. For instance, the CSR laser setup was successfully employed for investigating slow processes such as rotational cooling (Meyer et al. 2017), the decay of long-lived metastable states of atomic anions (Müll et al. 2021) and the cooling of isolated cluster systems (Müll 2023). The laser setup is depicted in more detail in appendix figure A.1 and described in Müll 2023 and Oetjens 2022.

In addition to the laser setup, the second linear section accomodates an electron cooler. This device produces an ultracold electron beam from a photocathode and overlaps it with the stored ion beam, so that electrons and ions collide at defined relative collision energies (Wilhelm 2019). Electron cooling reduces the longitudinal and transversal velocity spread of the ion beam (Wilhelm 2019) and rotationally cools molecular ions by inelastic collisions (Kálosi et al. 2022). At the same time, the electron beam serves as a target, from which the ions may attach an extra electron. Here, the current focus lies on recombination reactions between electrons and molecular cations (Jain et al. 2023; Novotný et al. 2019; Paul et al. 2022), as well as multiply charged atomic cations. In the future, it may also be relevant for investigating the interaction of low-energy electrons with complex biomolecules (Schippers et al. 2019) or the formation

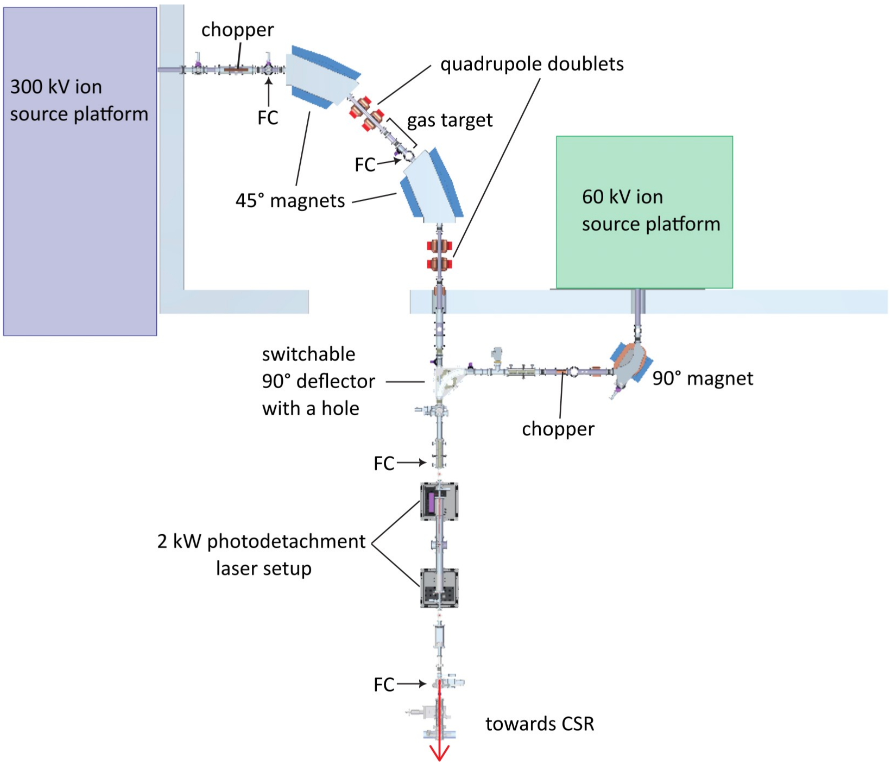

Figure 3.2: The ion supply of the CSR featuring the 300 kV ion source platform (depicted only partially), the 60 kV ion source platform and the transfer beamlines. Movable Faraday cups (FC) are positioned along the beamline for diagnostic purposes. Figure adapted from Müll 2023.

of dianions by electron attachment to singly charged anions (Jin et al. 1994).

The third linear section dedicates to ion beam diagnostics. Capacitive pick-up electrodes nondestructively measure the number of stored ions (current pick-up) and the revolution frequencies of the stored ion species (Schottky pick-up), which allow to infer all present ion species with high precision. This is particularly useful for identifying contaminant ion species by means of the Isochronous Time-of-Flight (ISO-ToF) mass spectrometry technique (Grieser et al. 2022; Hahn et al. 2016).

As of 2023, the fourth linear section houses the worldwide first cryogenic reaction microscope CSR-ReMi, which opens up completely new research opportunities on anions stored in the CSR. It is a combined spectrometer for electrons and ions in which the traversing ion beam can be crossed with a laser beam or a neutral gas jet, which is essentially a dense target of neutral atoms or molecules. Even though the primary objective is to investigate dissociative ioniziation of neutral gas molecules by collisions with the stored ion beam, recent work (Ben-Shabo et al. 2023) has demonstrated that the CSR-ReMi bears also a great potential as a kinetic energy spectrometer for the electrons emitted by stored anions. The electrons may originate from autodetachment, prompt photodetachment by laser irradiation within the CSR-ReMi, or even delayed photodetachment up to milliseconds after absorption of photons elsewhere in the storage ring (Ben-Shabo et al. 2023). In addition, using ultrashort laser pulses allows for time-resolved photoelectron spectroscopy (Schuurman and Blanchet 2022). As the density of the gas target can be controlled, it may be useful for studying collisional electron detachment of stored anions within the kinetic energy range (20–300 keV) of the CSR (Luna et al. 2001).

For supplying its experiments with ions, the CSR has its own infrastructure: The ions are produced by ion sources located in two dedicated setups referred to as ion source platforms (see figure 3.2). Evacuated transfer beamlines transport the ions to the CSR by means of magnetic and electrostatic ion-optical elements. In order to efficiently transfer the ions, they are accelerated up to 60 keV or 300 keV kinetic energy per elementary charge as soon as they leave the respective ion source platform. Diagnostic elements along the beamline (black arrows in figure 3.2) are essential for guiding the beam and also optimizing the transmission. A switchable 90° deflector selects which beam is to be transported further to the CSR (Grussie et al. 2022). In order to store an ion beam in the CSR, it is sliced into an ion pulse by a chopper and injected into the CSR by temporarily ramping down the voltage at its first 6° deflector (see figure 3.1) (Hahn et al. 2016).

While the 60 kV ion source platform is limited to operating one ion source at a time (Grussie et al. 2022), the 300 kV ion source platform is positioned more broadly: It is designed to house multiple sources for ions of atoms and molecules ranging from species with few particles to clusters, or even complex biomolecules (Mishra et al. 2015). The range of possible experiments at this facility strongly depends on the ion sources, ion beam transfer lines and diagnostic equipment for analyzing the intensity and composition of ion beams, in particular for larger molecular and cluster species. This motivates the present study of ion supply techniques for the CSR.

3.2 Developments for the ion supply for the CSR

This section is about practical developments made within the context of this thesis with the intention to improve the supply of CSR experiments with ions qualitatively and quantitatively. Our efforts in this regard concentrate on negative ions: In section 3.2.3 we present a new Laser VAPorization (LVAP) ion source setup for the production of cold cluster anions. We characterized this ion source using the Ion Source Test Bench (ISTB), which is an independent mass spectrometer setup dedicated to analyzing the output of ion sources. As the LVAP ion source typically delivers low-intensity pulses of negative ions, we augmented the ISTB ion detection system as described in section 3.2.1. In order to supply the CSR with cluster anions, the LVAP ion source will be transferred to a dedicated beamline of the 300 kV ion source platform. This beamline was designed by Mishra et al. 2015 with the goal to efficiently and flexibly provide ion beams from different types of sources. We completed the beamline setup, made it operational and present the commissioning results in section 3.2.2. As during the ion transport from the LVAP ion source to the CSR a certain fraction of these ions is lost, we estimated how many ions we can expect to have available for CSR experiments. These results, based on data from sections 3.2.1 and 3.2.2, are included in section 3.2.3. To analyze the output of the LVAP ion source once it provides the CSR with cold cluster anions, the CSR may be employed as a high-resolution mass spectrometer using a technique developed by Grieser et al. 2022. In section 3.2.4 we describe this method and how we augmented it to identifying contributions by excited-state anions to photodetachment-induced detector signals.

3.2.1 Ion source test bench

The Ion Source Test Bench (ISTB) is a mass spectrometer setup built (Nüsslein 2018) for the purpose of characterizing a wide variety of ion sources independent of the CSR facility, and before they are operated on the CSR high voltage ion source platforms (see figure 3.2). It has been improved continuously with the goal to take mass spectra of pulsed ion sources with comparably low ion output, such as the LVAP ion source (section 3.2.3). Three modifications are relevant in the context of this thesis. After briefly introducing the ISTB setup (section 3.2.1.1), we address these modifications in sections 3.2.1.2–3.2.1.4 and discuss their implications. Finally, we try to scale between the yield of the ions of interest obtained at the ISTB and the number of ions we can expect to have available for experiments at the CSR (section 3.2.1.5).

3.2.1.1 The beamline setup

Figure 3.3 a) gives an overview of the ISTB mass spectrometer setup. For an ion source attached to the ISTB, we choose as example the Laser VAPorization (LVAP) ion source. Its ion beam (red) is focused by an electrostatic einzel lens and sent through

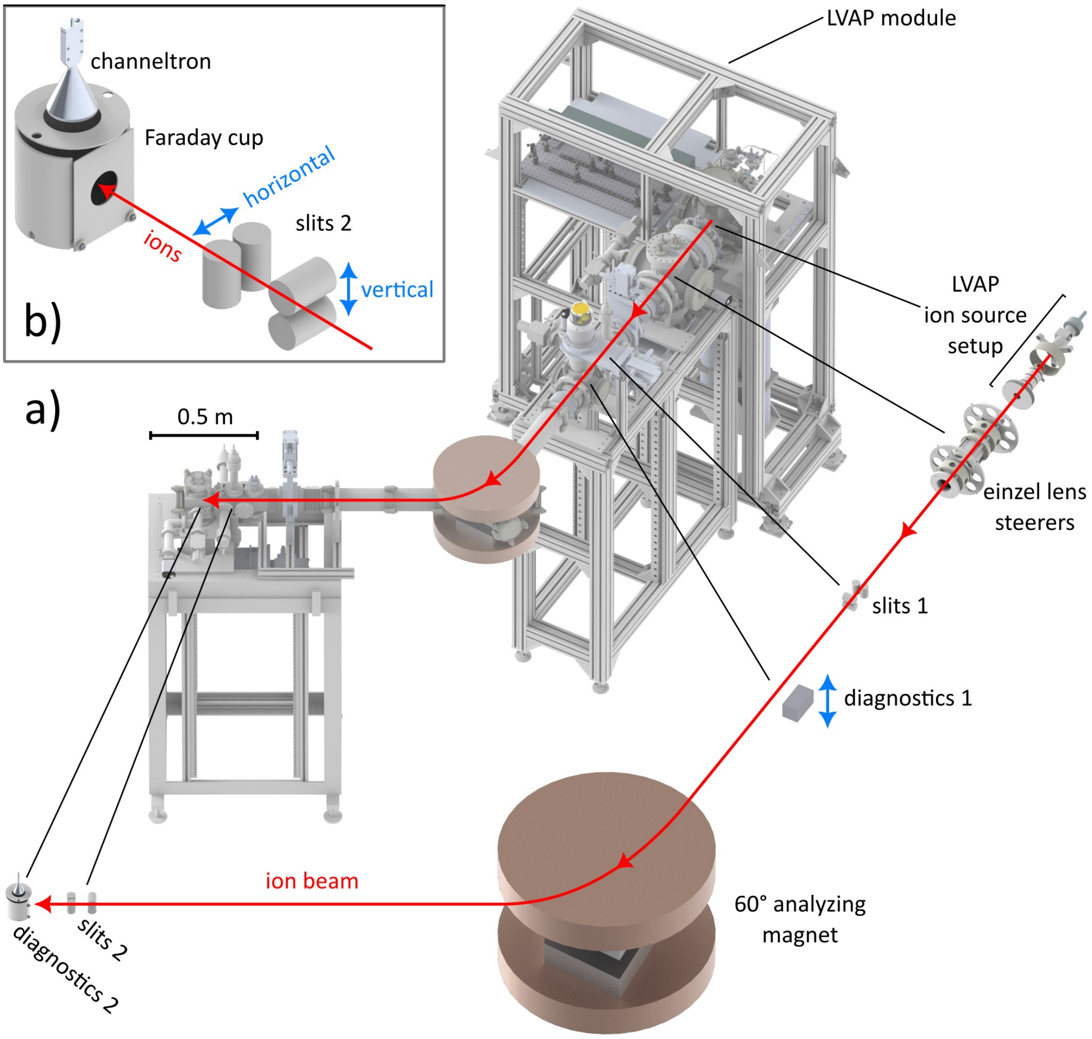

Figure 3.3: a) Overview of the ISTB with the Laser VAPorization (LVAP) ion source attached: The figure shows the vacuum chambers and the supporting racks of the mass spectrometer setup as well as a hauled-out and zoomed view of the relevant ion optical elements and detectors. Straight black lines indicate their position within the setup. Distances and dimensions are depicted to scale. The supporting rack of the analyzing magnet is not shown. b) Detailed view of slits 2 and diagnostics 2.

the field of a 60° analyzing magnet. The intensity of the transmitted ion beam is then measured destructively (diagnostics 2). We obtain mass spectra by ramping the magnet coil current and measuring the ion signal as a function of the magnetic field B. The mass-to-charge ratio

$$\frac{m}{q} = \frac{(Br_{\mathrm{B}})^2}{2U_{\mathrm{src}}} \tag{3.1}$$

then results from the magnetic field, the bending radius r_{B} of the magnet, and the voltage U_{src} applied to the ion source for accelerating ions with charge q to the final kinetic energy $E_{\mathrm{kin}} = qU_{\mathrm{src}}$ (Demtröder 2017). The magnetic field is measured by a Hall probe located between the magnet pole shoes. Nonlinear magnetic field effects due to the spatially varying saturation of the iron yoke are corrected by calibrating the total effective bending magnetic field against the field strength measured by the probe. A mass spectrum with known masses serves as basis for this calibration (Nüsslein 2018).

Mechanical slits (slits 1 and 2) limit the ion path through the spectrometer. Electrostatic steerers (vertical and horizontal) adjust the ion beam path if necessary. A movable Faraday cup (diagnostics 1) determines the total ion beam intensity from the ion source. Figure 3.3 b) shows a more detailed view of slits 2 and diagnostics 2: The horizontal slit pair of slits 2 (blue arrow) defines the mass resolution of the spectrometer. The Faraday cup is sensitive to ion beam currents $\gtrsim 30$ pA, while the channeltron detects ion beam currents $\lesssim 30$ pA down to single particles. If the channeltron is active, the Faraday cup serves as a converter plate, i.e., incoming ions are converted into electrons which are then detected by the channeltron. For more details on the setup refer to Nüsslein 2018.

3.2.1.2 Total ion yield of ion sources

In order to characterize an ion source for the overall intensity and time structure of its output, we added the Faraday cup (diagnostics 1) before the 60° analyzing magnet. For instance, the time structure of the total ion output of the LVAP ion source is depicted in figure 3.4 a) for positive ion source polarity and 5 keV ion kinetic energy. The cations were produced by pulsed laser ablation from a solid aluminum target and flushed to the ion source acceleration stage by a dense He gas pulse provided by a pulsed valve (details in section 3.2.3). The depicted cation pulse culminates at about 230 nA and has a duration of about 100 µs. The ion source output for reversed polarity is shown in figure 3.4 c). Here, the source was operated to produce cluster anions. The anion pulse peaks at about -120 nA current and lasts for about 200 µs. We attribute the longer pulse duration compared to figure 3.4 a) to the opening duration of the pulsed valve, which was set to be twice as large. The pulse duration and intensity may now be optimized further by changing ion source parameters and observing the Faraday cup signal. The Faraday cup thus complements the ISTB by offering direct diagnostics and optimization of the ion extraction.

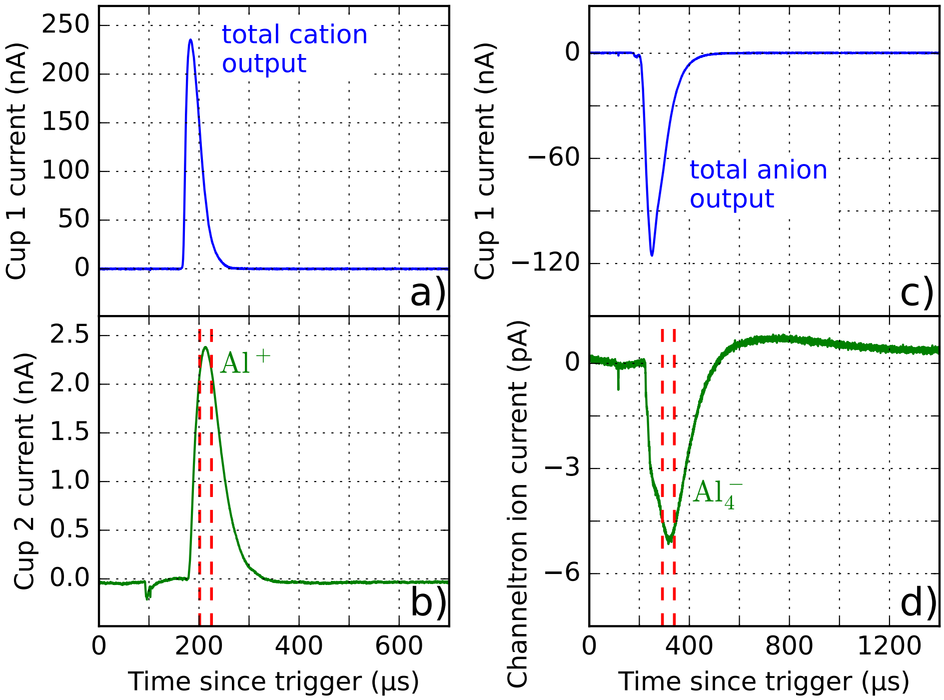

Figure 3.4: a)–d) Example time traces of 5 keV cation and anion LVAP ion source pulses detected with the diagnostic elements of the ISTB (figure 3.3). a) and c) Respective total cation and anion output at the Faraday cup before the analyzing magnet (diagnostics 1). b) Al^+ ions transmitted through the analyzing magnet and recorded with the Faraday cup of diagnostics 2. d) Al_4^- ions recorded with the channeltron of diagnostics 2. Here, the horizontal and vertical opening $[x, y]$ of the slits was set to $[2\text{ mm}, 2\text{ mm}]$ (slits 1) and $[2\text{ mm}, 2\text{ mm}]$ (slits 2). Each time trace is the mean of 32 individual samples. The red dashed lines in b) and d) indicate the respective fraction of the ion pulse which can be stored in the CSR for 300 keV ion kinetic energy. This will be discussed in section 3.2.1.5 and figure 3.5.

3.2.1.3 Sensitivity gap between particle counting and ion current measurement

The yield of ion sources operated or foreseen to be operated at the CSR facility lies in the range of pA to µA (Heinicke and Baumann 1969; Menk et al. 2018; Middleton 1989). While the Faraday cups of the ISTB (diagnostics 1 and 2) and their readouts[1] have an acceptable signal-to-noise ratio for ion currents $\gtrsim$ 30 pA, the channeltron (diagnostics 2) can count single particles up to a rate of 10 MHz corresponding to an ion current of 1.6 pA (Nüsslein 2018). The resulting sensitivity gap poses an obstacle for characterizing ion sources for which the output lies exactly in that gap. For instance, this is the case for certain configurations of the LVAP ion source (see section 3.2.3). In Nüsslein 2018 a first attempt was made to close this sensitivity gap.

---

[1] Fast current amplifier DLPCA-200, FEMTO Messtechnik GmbH.

Here, we now complete this endeavor: We operate the channeltron in a mode with lower amplification voltage, where it can sustain a higher rate of impinging ions, and thus a higher number of ions per incoming LVAP ion pulse. At the same time, single-particle impacts are not amplified enough to be counted individually. However, the channeltron still resolves the temporal envelope of the ion pulse as a whole. The envelope can thus be used to quantify the number of impacting ions. The signal of the entire incoming ion pulses is amplified, converted to a voltage signal and read out with a digital oscilloscope[2]. For technical details, refer to appendix A.2. An example for the resulting ion pulse signal is shown in figure 3.4 d), where the mean channeltron signal of an impinging pulse of Al_4^- ions is shown as a function of time. For comparison, the cup signal of Al^+ ions measured with the Faraday cup (diagnostics 2) is given in figure 3.4 b). It becomes apparent that apart from the actual Al_4^- ion peak in the range 200–500 µs the signal features a long positive tail, which extends over a time of $>$ 900 µs after the zero-crossing. We observed that the tail amplitude scales with the amplitude of the ion peak. It is not present in the cup signal and most likely inherent to the working principle of the channeltron: As the channeltron signal is the result of electron avalanches triggered by the incoming ion pulses, the tail is likely a result of the replenishing process of these electrons. The tail intensity may be related to the incoming charge. Note that the spikes at about 100 µs result from electronic switching noise of the LVAP ion source laser. The vertical scale in figure 3.4 d), i.e., the absolute incoming ion current was determined in a calibration process detailed in appendix A.2: Using carbon clusters C_n^- at various ion pulse intensities (see figure 3.15), we measured the channeltron amplification factor of the incoming ion current as function of its amplification voltage. Starting at a current accessible to both the channeltron and Faraday cup (0.5 nA), we increased the channeltron gain, thereby bridging the sensitivity gap down to a current of 0.5 pA. The corresponding count rate (3 MHz) lies well within the single-particle counting regime of the channeltron.

3.2.1.4 Mass spectra of pulsed ion sources

The third modification is related to the read-out and timing of the available signals. Compared to ion sources delivering a continuous current of ions, taking mass spectra of pulsed ion sources is more involved: The readout of magnetic fields and current signals has to be synchronized with the ion pulses. Furthermore, as the signals of ion pulses may differ in their time structure, they have to be integrated within defined time windows instead of taking the peak value of each ion pulse. For the ISTB, this is now possible based on a solution with LabView software and a digital oscilloscope[2]. Based on a trigger signal delivered by the ion source, one can define fixed time windows within which the diagnostics readout signal, e.g., the cup or channeltron signal as in figure 3.4 c) and d), is integrated. The integral values are then recorded as a function of the magnetic field and thus yield mass spectra. As the integration borders are variable

---

[2] PicoScope 5444B, 200 MHz, Pico Technology Ltd.

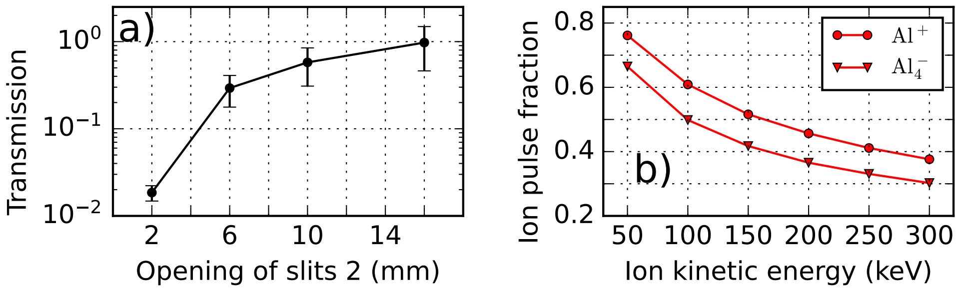

Figure 3.5: a) Transmission through the ISTB mass spectrometer depending on the horizontal and vertical opening $[x, y]$ of slits 2 (see figure 3.3 b). Here, the effective open area of the slits is a square, i.e., $x = y$. b) Maximum fraction of the ion pulses from figure 3.4 b) and d) which can be stored in the CSR plotted against the ion beam kinetic energy. The rightmost data points result from the slices indicated by the red dashed lines in figure 3.4 b) and d). The fractions for lower kinetic energies are also estimated by means of these figures.

with respect to the initial trigger signal, features such as the positive tail in figure 3.4 d) can be excluded from the integration. Also, if the signal features allow for it, the signal offset can be subtracted instantaneously by not only integrating over the ion pulse, but also over a dedicated subsequent time window of equal duration.

3.2.1.5 Number of ions to be expected for CSR experiments

As mentioned above the resolution of a mass spectrometer depends on the opening of the horizontal slits behind the analyzing magnet (see figure 3.3 b). A smaller opening gives a better mass resolution, but may at the same time go at the cost of transmitted ions. While for mass spectra a good resolution is relevant, a high ion number is better for the statistical quality of experiment data. At the ISTB we require well-resolved mass spectra, but at the same time we want to estimate how many ions at best we have available for experiments at the CSR.

To address this, we determined the transmission through the ISTB mass spectrometer as function of its slits settings after the magnet (slits 2). As ion source we employed the LVAP ion source (section 3.2.3). To mimic the situation with mostly round beam apertures at the CSR ion source platforms, we set slits 2 to a quadratic open area. Using mass-selected pulses of anions (as in figure 3.4 d), we first determined the relative transmissions. By means of different ion species, we estimated the systematic transmission uncertainty. As the magnet cuts a multi-species ion pulse down to only one species, it does not allow to determine the absolute transmission, which requires a reference measurement before the magnet. Hence, we also adjusted the LVAP to produce mostly a single ion species, i.e., Al^+ at $> 96\%$ relative abundance (see appendix figure A.8). The resulting transmission values and their corresponding systematic uncertainties are plotted in figure 3.5 a). The transmission through the setup increases drastically for a larger slit opening. We already gain an order of magnitude in the first opening step. If we take the transmission for the largest and smallest slit opening (16 mm and 2 mm) and consider the error bars, we get at least 20 times more ions.

One has to keep in mind, though, that not necessarily all ions of an ion pulse can be stored on the closed CSR orbit after gated injection (see section 3.1). The fraction of stored ions is given by the CSR orbit circumference $C_{\mathrm{CSR}} = 35.12$ m, the initial ion kinetic energy E_0 after production by the ion source, the final ion kinetic energy E_1 after acceleration by the high voltage ion source platform, the ion pulse duration t_0 and the ion mass m: While the initial pulse length is $s_0 = t_0\sqrt{2E_0/m}$, acceleration elongates it by a factor of $s_1/s_0 = \sqrt{E_1/E_0}$. For instance, the 5 keV bunches of Al^+ ($m = 27$ u) and Al_4^- ($m = 108$ u) in figure 3.4 b) and d) elongate from about 30 m to more than 200 m length if they are accelerated to 300 keV kinetic energy. The injected fractions are indicated by red vertical lines in figure 3.4 b) and d). The corresponding ion pulse fractions are given in figure 3.5 b), where they are also estimated for lower ion kinetic energies. Note that the ion pulse shape is taken into account as well. The maximum stored ion pulse fraction increases for lower ion kinetic energy and lower ion pulse duration. In combination with the transmission estimate from above we thus get > 6 times more ions than in the well-resolved mass spectra with low transmission settings.

3.2.1.6 Conclusion

The described improvements of the ISTB enable us to measure absolute ion currents of pulsed ion sources in an intensity regime previously not accessible to its detector sensitivity, i.e., ion currents from 0.5–500 pA. Also, we estimated how many more ions than in mass spectra obtained for typical ISTB settings we can expect to have available for CSR experiments. Note that the transmission factors of the setup on the 300 kV ion source platform and the transfer beamline (see section 3.1) have not yet been taken into account for the calculation of the CSR ion number. We address these points in the context of sections 3.2.2.2 and 3.2.3.4.

3.2.2 Electrostatic branch of the 300 kV ion source platform

The CSR facility features two setups dedicated to supplying the storage ring experiments with ions. One of these is the 300 kV ion source platform sketched in figure 3.6 a). It is an ion source setup on a common-potential high-voltage platform encapsulated in a Faraday cage which is lifted to a voltage of up to ±300 kV, thereby providing ion beams with kinetic energies up to 300 keV per elementary charge. It subdivides into two sections (figure 3.6 a): The so-called *magnetic branch* comes with a single ion source port and a 90° magnet for mass selection. It supplies the CSR with continuous ion beams of atoms and small molecules with ion currents on the order of nA to µA. The more involved part called *electrostatic branch* (figure 3.6 b) can house up to four ion sources at once. Its fully electrostatic design allows for the transmission of ion beams independent of the ion mass. Mass separation then happens further downstream by means of the magnets in the transfer beamline (see figure 3.2) or in the CSR (see section 3.2.4). The electrostatic branch is foreseen to provide the CSR with beams of more complex ion species, such as clusters from a pulsed Laser VAPorization (LVAP) ion source (see section 3.2.3) or biomolecules. As we expect to get comparably low ion currents of these species (< nA), the electrostatic branch beamline is designed to have a high transmission efficiency.

The developments around the electrostatic branch started in 2015 (Mishra et al. 2015). The beamline design is based on simulations by P. M. Mishra and M. Grieser. Ion-optical and diagnostic elements were selected accordingly. The mechanical assembly commenced with the assembly and alignment of the ion-optical elements and their vacuum chambers.

In the course of this thesis, we made the electrostatic branch ready for operation: We completed and assembled the diagnostic elements and built them into the beamline setup. To make two out of the four ion source ports accessible, we added additional ion-optical and mechanical elements. Finally, we commissioned the beamline setup in order to determine if it is suited for operation with the LVAP ion source. In the following, we introduce the electrostatic branch setup, present the commissioning results and compare them to the simulations before concluding with a short summary.

3.2.2.1 The electrostatic branch beamline setup

Here we present the electrostatic branch of the 300 kV ion source platform. Figure 3.6 b) shows a technical view of the electrostatic branch in its current development stage, where the ion source (IS) ports 1 and 3 are made available for ion sources. In the hauled-out view of the ion optical elements, the ion beam is depicted in red. Starting at IS 1, it passes through an einzel lens and steerers and is deflected left by an electrostatic

90° cylindrical deflector (CD)[3]. The following electrostatic quadrupole triplet (QT)[4] focuses the ion beam horizontally and vertically and corrects its angle and offset, if necessary. Further downstream, the beam is deflected and focused two more times by identical sets of ion optical elements (CD 2 and QT 2, CD 3 and QT 3), so that it points in the same direction as initally at IS 1. It then passes through the straight port of the (switched-off) 90° magnet, one more quadrupole triplet (QT 4)[4], leaves the Faraday cage and accelerates to its final kinetic energy.

The described 90° deflection steps create space for three more ion sources (IS 2–4). Their ion beams are coupled into the beamline via the straight ports of the deflectors (CD 1–3). While IS 1 is foreseen to house a pulsed Laser VAPorization (LVAP) ion source for the production of cluster ions (see section 3.2.3), IS 3 is a permanently installed Heinicke-type Penning ion source (Heinicke and Baumann 1969), which produces µA cation beams from gaseous educts (Wolf 1995). It provides ion beams for finding the correct settings of the subsequent ion optical elements of the 300 kV ion source platform and the transfer beamline to the CSR (see figure 3.2), which is useful for piloting beams from other ion sources with very low ion yield. Furthermore, its beam is available for testing the ion storage conditions of the CSR. While IS 4 is foreseen to be a compact source for ions of atoms or small molecules, we envisage IS 2 to be an electrospray ion source (Kebarle and Verkerk 2009) for large organic molecules, which may even be equipped with a dedicated mass separation and accumulation stage (Mishra et al. 2015). Alternatively, the electrospray ion source could be combined with an ion mobility spectroscopy setup, which allows to distinguish *isomers* by their collisional cross section with a buffer gas (see contribution by O. Heber and Y. Toker in Zettergren et al. 2021).

In order to detect the ion beams on the way through the electrostatic branch, the setup also features diagnostic elements capable of single-particle counting and measuring µA ion currents. They are located in the straight sections between the 90° deflectors (diagnostics 1 and 2) and at the end of the beamline (diagnostics 3). Diagnostics 2 and 3 are adapted versions of the detectors used at the Ion Source Test Bench (ISTB) (see figure 3.3 b) and elsewhere in the CSR facility. Compared to the ISTB the top part of the Faraday cup can be moved into and out of the ion beam path (blue arrows in figure 3.6). The first detector unit in the beamline (diagnostics 1) is adapted from the detector used in Repp 2012. Figure 3.7 a) shows the relevant components: In addition to current measurements with a Faraday cup and single-particle counting with an MCP detector[5], it is capable of visualizing the ion beam profile via a phosphor screen[6] and

---

[3] Scaled and adapted version of 90° deflector with hole from Grussie 2016 used in CSR transfer beamline (figure 3.2).

[4] Model Quad-60-01, 30 mm singlet electrode length, 11 mm singlet distance, RoentDek Handels GmbH.

[5] Both plates model MCP-25-10-40-Image, active area diameter 25 mm, GIDS GmbH.

[6] P43 phosphor layer with additional Al layer, active area diameter 25 mm, ProxiVision GmbH.

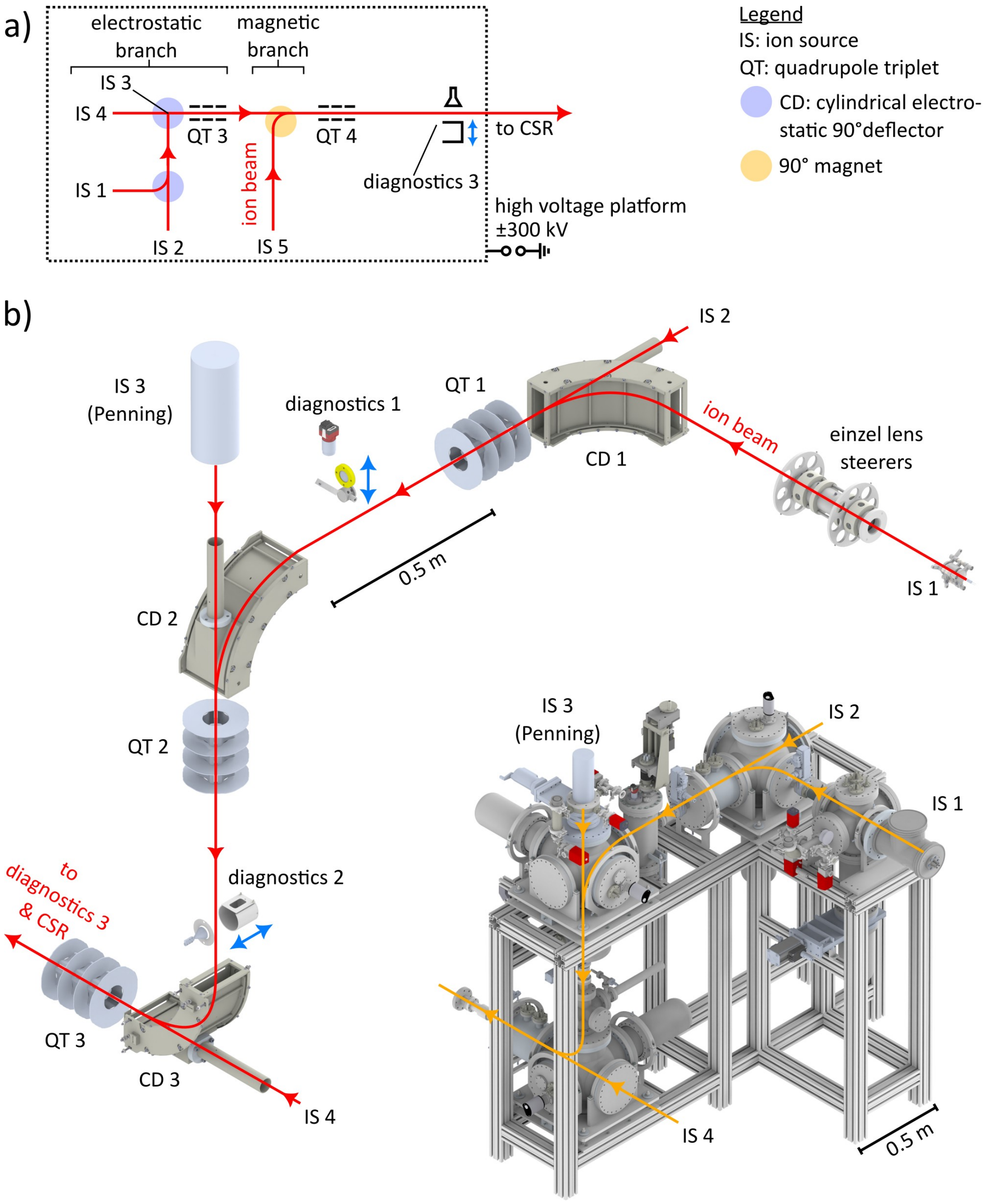

Figure 3.6: a) Sketch of the 300 kV ion source platform of the CSR facility. b) To-scale technical models of the electrostatic branch with ion optical and diagnostic elements and the vacuum chambers (inset) housing them. The red and orange lines with arrows depict possible ion beam pathways. Abbreviations and symbols in a) and b) are explained in the legend. Blue arrows indicate movable components. Diagnostics 3 is located about 1.8 m downstream of the end of QT 3.

a fast camera[7]. An actuator allows to switch between the detection methods or to let the ion beam pass undisturbed.

In addition the dedicated Faraday cups, the electrodes of the 90° deflectors (CD 1–3) are also used for measuring the ion beam current: To this end, the deflecting voltages at the inner and outer deflector plates are switched off, so that the ion beam is dumped at the outer deflector plate. An amperemeter connected to the outer plate measures the ion current. A negative voltage (-120 V) applied to the inner plate confines secondary electrons which result from the ion beam impinging on the surface of the outer plate. The switching between the deflecting mode and the Faraday cup mode is automated and done remotely. It is particularly useful for characterizing the total output of IS 1.

3.2.2.2 Beamline commissioning and results

With all relevant elements introduced, we now discuss the commissioning of the electrostatic branch. We focus on testing the imaging capabilities of diagnostics 1, the horizontal and vertical steering with the first quadrupole triplet QT 1 and the transmission efficiency of the beamline. As copies of diagnostics 2 and 3 are already operational at the ISTB (figure 3.3) and the CSR facility, we forgo detailed tests of their channeltron detectors.

For the commissioning we employ an Ar^+ ion beam from the stationary Penning ion source (IS 3 in figure 3.6) and a Cs^+ ion beam from an aluminosilicate ion source[8] mounted at the IS 1 port. This ion source produces ions via thermionic emission from a heated aluminosilicate substrate (Blewett and Jones 1936). Figure 3.8 shows the ion source with dedicated ion-optical elements for accelerating and focusing the ion beam. The ion output intensity is controlled via the heating (900–1200°C) voltage and current (up to 2 A at 7.6 V). Tests at the ISTB showed that the ion output is variable in the range between 100 s^{-1} ion count rate and 100 pA ion current.

We first test the imaging capabilities of diagnostics 1 with a 2 keV Cs^+ beam for different ion beam intensities: For a low-intensity ion beam ($\sim 10^3$ s^{-1}) and high voltages applied to the MCP detector (1.8 kV) and the phosphor screen (4.7 kV) we see signals of single ions appear as black dots in figure 3.7 b), where the phosphor screen image is depicted with inverted colors. We increase the ion beam intensity (up to 60 pA) and lower the MCP (down to 0.7 kV) and phosphor screen voltages (down to 4.3 kV) in order to avoid damaging the detector. We then optimize the transmission up to diagnostics 2 (behind the first bender) by varying the focusing and steering voltages at all ion optical elements upstream of this diagnostics. As a result, almost 100% of the initial ion current measured at CD 1 arrives at the Faraday cup of diagnostics 1, and about 87% at diagnostics 2. We then have a look at the ion beam profile presented

---

[7] Model 1800 U-040m mono C-Mount, with 25 mm focal length objective, Allied Vision Technologies GmbH.

[8] Model 101139-01 alkali ion source, HeatWaveLabs, Inc.

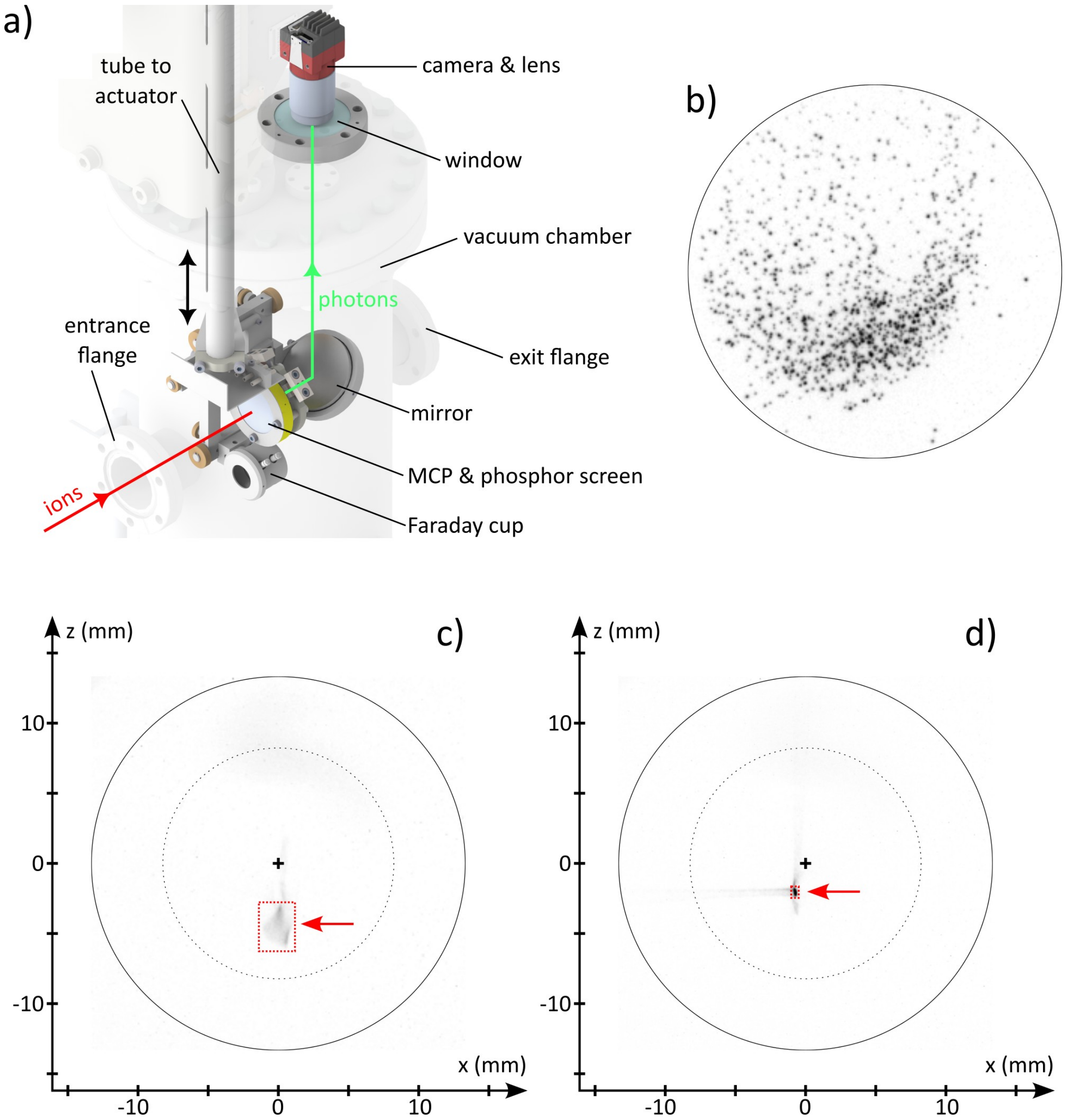

Figure 3.7: a) Movable detector with Faraday cup, MCP plates and phosphor screen for ion beam profile visualization (diagnostics 1 in figure 3.6). If the detector is moved out of the way (black arrow), the ion beam can leave the vacuum chamber via the exit flange. b) First light at the phosphor screen (color displayed inverted) with single-particle amplification at the MCP plates. c) and d) Phosphor screen image with ion current amplification at the MCP plates. While in c) the ion beam transmission was optimized, in d) the beam was focused to appear as small as possible on the phosphor screen. Black full circles indicate the phosphor screen active area (diameter 26.67 mm), black crosses its center, and black dashed circles the Faraday cup aperture (diameter 16.5 mm). The phosphor screen images were captured with 0.5 s integration time of the monochromatic camera. For better visibility, the pixel saturation in b) and c) was increased. Note that the camera images the back of the phosphor screen and the mirror inverts the vertical image axis: If the ion beam in a) hits the detector front side more left [upwards], the ion beam spot in b)–d) moves in positive x [negative z] direction in the camera image.

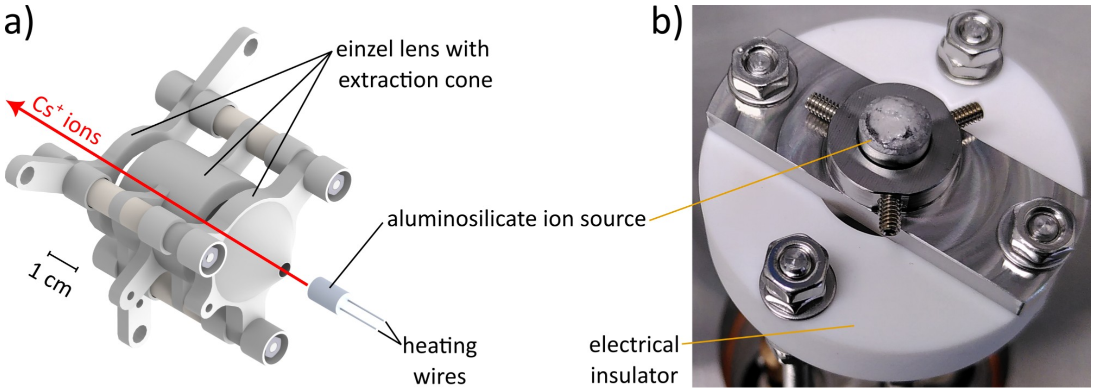

Figure 3.8: Ion source setup used for commissioning the electrostatic branch (IS 1 in figure 3.6). a) To-scale technical model of the aluminosilicate ion source with ion optical elements for acceleration and focusing of the Cs^+ ion beam. While the extraction cone (aperture diameter 4 mm) is grounded, the ion source itself can be lifted to up to +4 kV. b) The ion source mounted in its holder (design adapted from Schotsch 2021). It is electrically insulated against the grounded base flange (background). The emission surface of the ion source has a diameter of about 6 mm.

in figure 3.7 c). It appears as a haze on the phosphor screen because we are no longer in the regime of single-particle amplification. The calibration of the coordinates was performed by means of an image with enough light in the vacuum chamber to make the back of the phosphor screen and its holder visible. The red box around the beam profile has a size of about 2.6 mm × 3.5 mm and is displaced from the center of the phosphor screen (black cross).

Only in a next step, we attempt to focus the ion beam to become as small as possible (figure 3.7 d). The settings of all ion optical elements upstream of diagnostics 1 are changed, while only the deflecting voltage of CD 1 is left unchanged. We also have to change the focusing voltage of the dedicated einzel lens of the ion source (figure 3.8). The resulting ion beam profile features an intense focus with a faint asymmetric cross halo. The pronounced oval-shaped center has a size of about 0.6 mm × 0.9 mm. Here, only about 41% of the initial (CD 1) ion current arrives at diagnostics 1. The displacement with respect to the phosphor screen center appears to be smaller.

The Faraday cup aperture is given for comparison as dashed black circle in figure 3.7 c) and d). Both ion beam profiles are rather small and, despite their displacement, fully enclosed by the Faraday cup aperture once it is in the ion current measurement position. Hence, the difference in transmission efficiency between c) and d) likely results from ion loss on the ion beam path between CD 1 and diagnostics 1.

We now test the steering of the first quadrupole triplet QT 1 by changing the horizontal and vertical steering voltages and determining the position and size of the ion beam profile on the phosphor screen active area. We vary only the steering voltage for one direction at a time and leave the steering voltage for the other direction at 0 V.

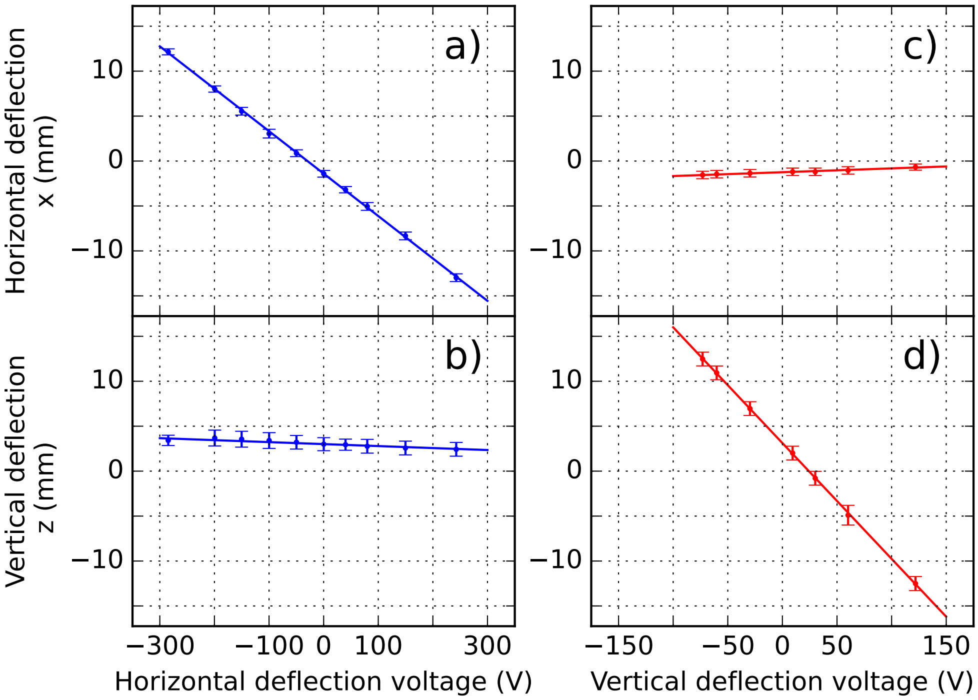

Figure 3.9: Horizontal and vertical position of the ion beam on the phosphor screen plotted against the horizontal (a and b) and vertical (c and d) deflection voltage applied at the quadrupole triplet (QT 1 in figure 3.6). The corresponding coordinate system is given in figure 3.7 c) and d).

All other beamline settings are unchanged. We estimate the position and size of the beam profile on the phosphor screen from the center and dimensions of a rectangular box drawn around it, as in figure 3.7 c) and d). The extracted beam profile positions are plotted against the deflecting voltages in figure 3.9. The blue data set in a) and b) displays the horizontal and vertical position on the phosphor screen as function of the horizontal steering, while the red data set in c) and d) shows the positions for vertical steering. The error bars represent the estimated size of the ion beam profile and the straight lines are linear fits. The strong linear trends of the deflection in a) and d) reveal that the ion beam can be directed well in either direction and close to the borders of the phosphor screen (about ±13.3 mm). From b) and c) we see that unwanted deflection in the direction which is supposed to be unchanged plays only a minor role ($\leq 5\%$). Overall, the required horizontal deflection voltage is about twice as high as the vertical deflection voltage. Also, in either case, the beam profile has an offset of few mm, so that the linear ranges appear to be asymmetric with respect to the phosphor screen center.

Finally, we test the transmission efficiency of the beamline. Here, we start with a

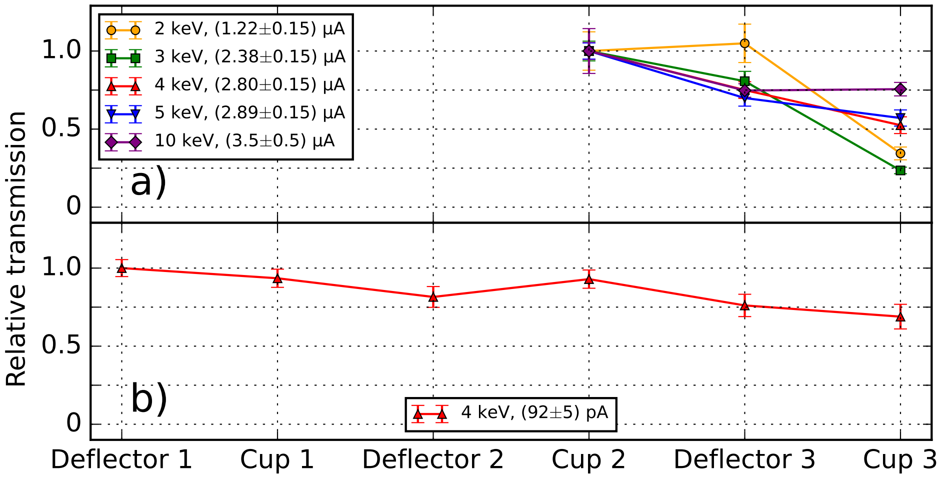

Figure 3.10: Ion beam transmission through the electrostatic branch (figure 3.6) for maximized ion current at cup 3. We used a) Ar^+ from a Penning ion source (IS 3) at various ion beam kinetic energies and b) Cs^+ from an aluminosilicate ion source (IS 1, see also figure 3.8). Along the beamline, the ion current was measured with the various deflectors (CD 1–3) in Faraday cup mode and with the dedicated Faraday cups (diagnostics 1–3). Each data set is scaled by the measured absolute ion beam current of its first data point. The measured current is given in the legend, along with the ion beam kinetic energy.

2 keV beam of Cs^+ from IS 1. A straightforward continuation of the optimization procedure in order to also steer around the third 90° deflector (CD 3) turned out to be not feasible. Instead, to find the correct settings of CD 3 and the subsequent ion-optical elements, we use a 3 µA beam of 5 keV Ar^+ ions delivered by IS 3. The high beam intensity allows us to find and optimize the ion signal at the Faraday cup of diagnostics 3. We repeat the transmission test for lower and higher kinetic energies by scaling and optimizing the beamline settings found for 5 keV. Figure 3.10 a) shows the measured relative ion current along the diagnostic beamline elements downstream of IS 3 for different kinetic energies. The error bars are estimated from the accuracy of the amperemeter. The transmission from diagnostics 2 to diagnostics 3 is best for 10 keV kinetic energy and lower for lower kinetic energy. It is particularly low ($< 40\%$) for ≤ 3 keV kinetic energy, which may explain our failed transmission attempt with IS 1.

With the found beamline settings we start a second transmission attempt with IS 1. As for beam energies > 4 keV we notice electrical breakdowns in the setup of IS 1, we stay at 4 keV. The relative ion currents measured along the beamline from IS 1 to diagnostics 3 are depicted in figure 3.10 b). Of the initial ion current of 92 pA at deflector 1, a fraction of

$$T_{\mathrm{meas}} = (69 \pm 8)\% \tag{3.2}$$

arrives at the Faraday cup of diagnostics 3, which is behind the exit of the electrostatic beamline branch on the platform.

3.2.2.3 Comparison to the simulation

The optimized settings after commissioning and the obtained transmissions can be compared to the available parameters and assumptions of the simulation (model based on electrostatic fields) carried out by P. M. Mishra and M. Grieser (see appendix A.3). The simulation includes all ion-optical elements between CD 1 and diagnostics 3 (see figure 3.6 and appendix figure A.3). The einzel lenses and steerers upstream of CD 1 are thus not included. The ion beam was assumed to consist of 5.1 keV protons and to commence before CD 1. Furthermore, it was assumed to have a Gaussian beam profile and a 2σ emittance of 40 mm·mrad in horizontal and vertical direction. At the position of diagnostics 1–3 the ion beam was focused to be as small as possible using the quadrupole triplets QT 1–4.

The transmission of the simulated 5.1 keV proton beam up to diagnostics 3 was found to be $T_{\mathrm{sim}} \approx 76\%$, which agrees well with the measured 4 keV Cs^+ beam transmission (see equation 3.2). The measured beam profile for a well-focused beam at diagnostics 1 (figure 3.7 d), including the cross-shaped halo, compares well in shape to the simulated beam profile at diagnostics 2 (see appendix figure A.4). Compared to the simulated beam, the Cs^+ beam seems to have a smaller emittance, as it can be focused to a much smaller spot size on the phosphor screen located at the position of diagnostics 1 (factor ~ 10 smaller in either dimension).

According to the simulation, the sizes of the ion beam profiles at diagnostics 1–3 do not vary among each other by more than a factor of 2. With the small Cs^+ beam profile measured at 2 keV kinetic energy in mind, we can thus safely assume that the complete ion beam profile is captured by the Faraday cups[9] and that the measured ion currents along the beamline do not suffer from spatial cut-off by the diagnostic elements themselves.

The asymmetric cross shape of the halo may result from the quadrupoles: The outer part of each quadrupole singlet surface is not bent in a perfect hyperbolic shape and leads to nonlinear contributions to the electrical field as a function of the ion displacement from the center. These contributions result in filamentation of the phase space of the ion beam, i.e., the distribution is distorted as the beam passes through the

---

[9] Diagnostics 1 and 3 have round Faraday cup apertures with diameters 16.5 mm and 14 mm. The cup aperture of diagnostics 2 is rectangular with dimensions 20 mm × 35 mm (width × height). The rectangular CD 1–3 entrance and exit apertures have the dimensions 36 mm × 114 mm.

quadrupole triplet (Grussie 2016). This also manifests in the shape of the ion beam profile.

The < 5 mm displacement of the ion beam profile at the imaging detector of diagnostics 1 is not predicted at this extent by the simulation and likely results from a combination of systematic factors: While the beamline alignment was carried out by means of precision alignment targets and a Taylor-Hobson telescope (method also described in Nüsslein 2018), the vertical alignment in this part turned out to be challenging because of imperfect manufacturing of the stainless steel vacuum chambers in the beamline between CD 1 and 2. Possible misalignment may thus partly explain the vertical component of the beam profile displacement. The potential misalignment of the imaging detector, which was added to the setup much later, introduces another systematic uncertainty. As it was not possible to equip it with a high-precision alignment target, we estimate its alignment precision to be up to 2 mm in either dimension. Nonlinear electrical field components of the ion-optical elements may also influence the ion beam displacement. Considering the narrowest round[10] and rectangular[11] apertures in the beamline and the good agreement between simulated and measured transmission, we conclude that the estimated alignment imperfections of a few mm are still acceptable.

3.2.2.4 Conclusion

We presented the electrostatic branch setup of the 300 kV ion source platform and the results of the commissioning of this fully electrostatic beamline, for which we deployed ion beams of two different ion sources. We found a high transmission efficiency of $T_{\mathrm{meas}} = (69 \pm 8)\%$ (equation 3.2), including the three 90° bends of the setup, which is in agreement with the simulated transmission efficiency. The imaging detector of diagnostics 1 revealed that the used ion beam has a lower emittance, and thus a higher beam quality than assumed in the simulation. Hence, we conclude that for an ion source with good beam quality we get most of the ions to the end of beamline, where they are accelerated to their final kinetic energy and transported to the CSR. In its current state, the electrostatic branch is thus prepared to house the pulsed LVAP ion source for the production of cluster ions (see section 3.2.3).

The electrostatic branch is already being used for CSR ion beam injection in an experimental campaign ongoing at the time of writing of this thesis. From the position of IS 1, a C_{60}^{+} ion source has provided the CSR with up to 180 nA of C_{60}^{+} ions for electron recombination experiments.

---

[10] The beamline tube diameter is ≥ 37 mm.

[11] Rectangular aperture 20 mm × 35 mm (width × height) located before diagnostics 2.

3.2.3 Laser vaporization ion source for the CSR

In the light of recent and ongoing photodetachment studies on ro-vibrationally hot aluminum clusters stored in the CSR (Müll 2023), we are interested in conducting complementary studies for which the clusters are already cold from the beginning of the storage. As shown by Breitenfeldt et al. 2018, cold anionic clusters can be produced by means of a Laser VAPorization (LVAP) ion source. It is a cluster ion source capable of producing cationic, anionic and neutral clusters by combining precooled buffer gas from a pulsed gas valve and laser ablation. It was introduced by the groups of Dietz et al. 1981 and Bondybey and English 1981, and since then adapted to the applications of many other research groups (Duncan 2012).

Here, we present a new version of an LVAP ion source dedicated to supplying the CSR with cold anionic clusters. The ion source design was developed in collaboration[12] with the Niedner-Schatteburg group from the University of Kaiserslautern-Landau (RPTU) and is based on their original design presented, e.g., in Meyer 2014. Instead of the in-house-built pulsed gas valve, the new design also allows the use of a commercial gas pulse valve. After first successful tests (Himmelsbach 2022), we now accelerate ions out of the new ion source and characterize its output with a mass spectrometer.

In the following, we describe how the LVAP ion source produces cluster ions (section 3.2.3.1), present the relevant parts of the new experimental setup (section 3.2.3.2) and discuss anionic mass spectra obtained for two different target materials (section 3.2.3.3). With Al_4^- as example, we try to cultivate a specific cluster species in the spectrum (section 3.2.3.4) and give a short summary (section 3.2.3.5).

3.2.3.1 Cluster ion production principle

Here, we introduce how the LVAP ion source produces cluster ions and summarize the most relevant parameters for cluster production. A schematic LVAP ion source is depicted in figure 3.11: A laser pulse is focused onto a rotating target surface, ablates material and creates a hot plasma plume (Howe 1963; Tremblay et al. 1987). The plasma contains electrons, positive and negative ions and neutrals of the target material (Hettich and Jin 1994) and is overall neutral (Duncan 2012). It is injected into a narrow channel, where it is crossed by an intense and supersonically expanded gas pulse delivered by a pulsed valve. The cold gas pulse takes the hot plasma further along the channel. Three-body collisions, each between a gas particle and two particles of the target material, lead to the formation of clusters, as the gas particle takes away excess binding energy. The cold gas particles further collide with the clusters, thereby taking away translational energy from the clusters and quenching excited vibrational, rotational and electronic state populations. When the gas pulse leaves the channel, it for a second time supersonically expands and cools. Further downstream,

---

[12] See reference 29 in Nüsslein 2018.

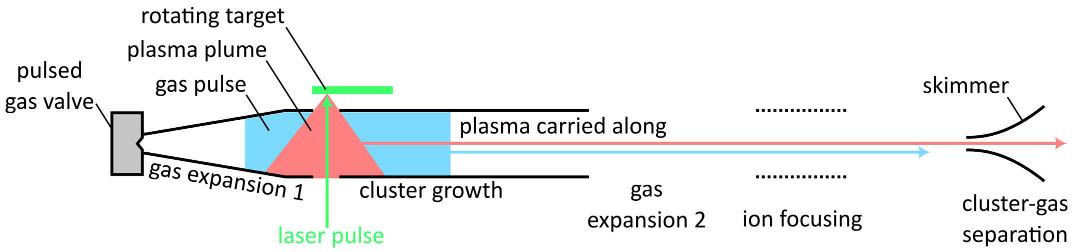

Figure 3.11: Schematic of the ion production principle of the LVAP ion source.

the clusters traverse a skimmer, where they are separated from most of the gas particles. A subsequent experiment then has positive, negative and neutral clusters at its disposal (Duncan 2012). The desired ion polarity may be selected by means of electrical potentials applied to the skimmer and other electrodes available within the ion source setup.

Commonly, this type of ion source uses nanosecond laser pulses for ablation (Duncan 2012). In our experiment we employ a nanosecond pulsed laser as well. The energy contained in the laser pulse is the most important parameter for cluster formation (Duncan 2012). The laser pulse is focused to a spot in order to achieve a high energy fluence at the target surface. Above a critical fluence threshold, which depends on the target material, the laser photon wavelength and the laser pulse duration, material is explosively emitted from the target surface (Lutey 2013). With increasing pulse energy the cluster yield increases and reaches a maximum. As the laser then heats the plasma excessively and thus hampers the cluster condensation, the cluster yield decreases again. The laser pulse energy has to be re-optimized every time another experimental parameter is changed. In order not to drill a hole into the target and hamper efficient material emission, the surface should be continuously refreshed by rotating the target (Duncan 2012).

The choice of the gas and its backing pressure determine how well the clusters are cooled. Light gas particles move faster and therefore have higher collision rates. A higher gas pressure leads to a higher density in the gas pulse and thus a higher three-body collision rate, which favors cluster formation. Cluster condensation works best in the local and temporal maximum of the gas pulse, where the gas density is highest. Consequently, the timing between the laser pulse and the gas pulse is also critical.

Geometrical parameters, such as the length and diameter of the cluster growth channel and the target position relative to the gas flow also play a role for the cluster production. For instance, a longer channel confines the gas and the plasma longer and leads to more collisions, but at the same time more material is lost to deposition at the channel walls. The axial skimmer (figure 3.11) position relative to the subsequent chamber wall and to the nozzle of the pulsed valve is relevant for the transmission efficiency of ions through the skimmer orifice.

Electrical fields in the ion source chamber should be used with care: If applied, they lead to charge separation of the initially neutral plasma so that space charge effects come into play. This is especially relevant in areas with high gas density, where the induced collisions and turbulences heat the clusters and reduce transmission (Duncan 2012).

3.2.3.2 Experimental setup

Based on the principles described in the previous section 3.2.3.1 we introduce here the setup of the LVAP ion source developed for the CSR. Most components are housed in the LVAP module which can be moved between the Ion Source Test Bench (ISTB, section 3.2.1) and the 300 kV ion source platform (section 3.2.2). An overall view of the LVAP module is included in figure 3.3, where it is installed at the ISTB.

The ion source and the electrodes for ion extraction and acceleration are presented in figure 3.12 a). A to-scale sectional view of the components around the vaporization block illustrates the path of the gas, laser and ions (figure 3.12 b). This layout is based on the ion source implemented in the Niedner-Schatteburg group at the University of Kaiserslautern-Landau (RPTU), but developed with respect to a better separation of electrical ion source potentials, a more flexible gas line design, and independent long-term operation on the 300 kV ion source platform for the CSR experimental campaigns.

In the valve module 1a, the present version uses a commercial pulsed valve[13] to produce the short and dense gas pulses from a He gas reservoir with up to 15 bar absolute backing pressure and at up to 5 kHz rate. The Opening Duration (OD) of the valve determines the temporal duration of the gas pulse and is variable from 20–400 µs (Janssen 2021). The commercial pulsed valve replaces the previously used in-house-built valve with significantly larger dimensions (Meyer 2014). It is mounted such that it may be exchanged by the in-house-built valve with relatively low effort, e.g., for performance comparison or troubleshooting purposes. A PTFE gasket (2) and an additional nozzle (3) with a channel diameter of 0.4 mm and a channel length of 19 mm connect the commercial valve to the vaporization block (4).

The focused laser pulse traverses the vaporization block perpendicular to the path of the gas pulse via a dedicated channel with a diameter of 1.5 mm. It ablates a circular track on the rotating target disk (6). Horizontal motion (left-right in figure 3.12 b) of the ablation target unit by means of a nearby motor changes the track if needed. As the continuously operated motor for target rotation would overheat in the vacuum, it is placed on the atmospheric side of the ion source flange and mechanically coupled (Karthein 2015) to a gear attached to the target axis. A PTFE spacer (7) keeps the target holder at a defined distance of about $d_{\text{target}} \approx 1.3$ mm with respect to the hole through which the ablated material enters the vaporization block. If a target disk is glued[14] onto the holder, this distance reduces by the disk thickness and the thickness

---

[13] ACPV2-300, MassSpecpecD BV.

[14] Torr Seal #9530001, Agilent Technologies Sales & Services GmbH & Co. KG.

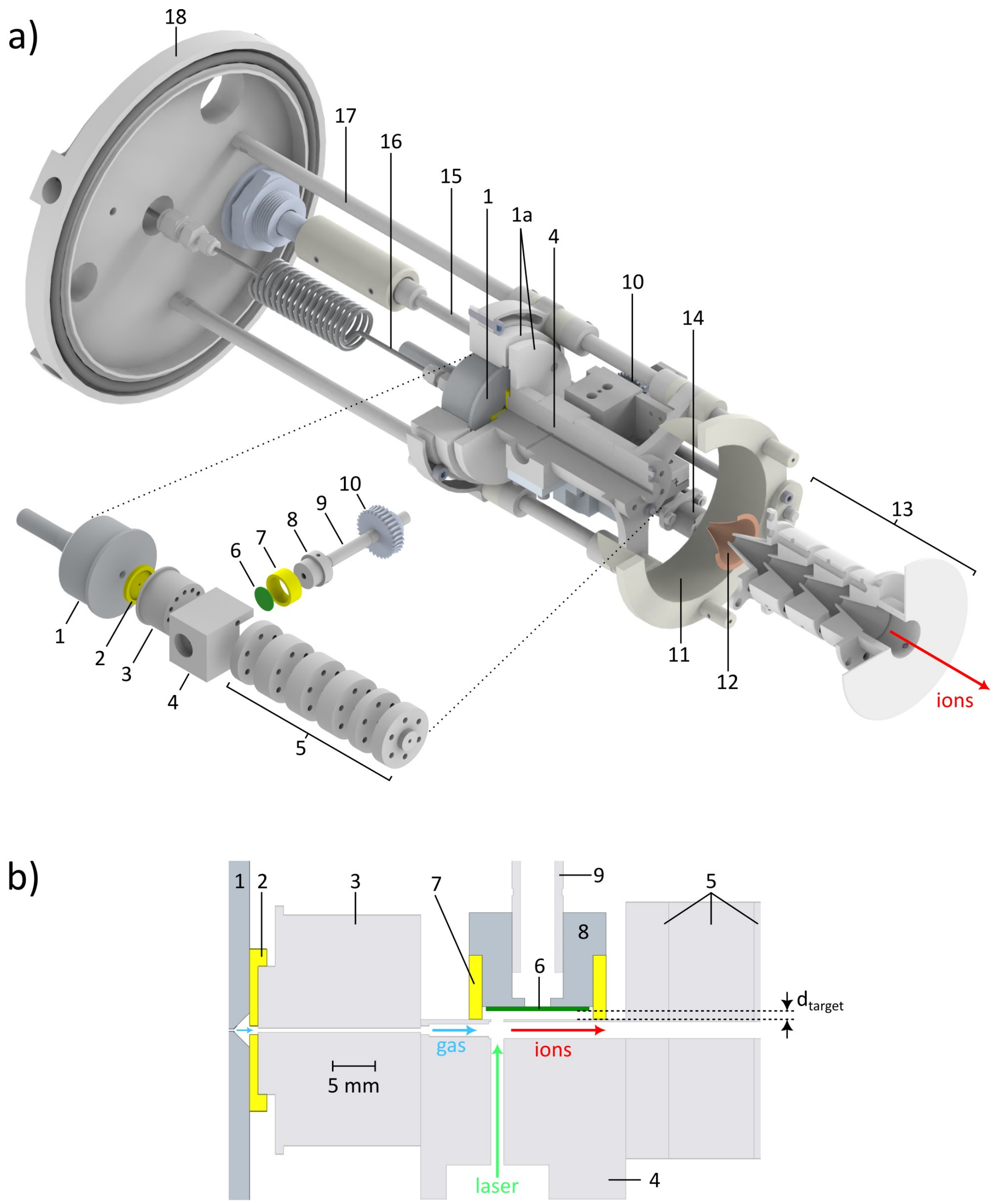

Figure 3.12: a) Sectional view of the LVAP ion source with ion extraction and exploded view of the components directly involved in the cluster ion production (ion source block): (1) pulsed valve (1a) valve module (2) PTFE gasket (3) nozzle (4) vaporization block (5) cluster growth channel block (6) ablation target (7) PTFE spacer (8) target holder (9) tubular rotation axis (10) gear (11) mesh for ion focusing (12) skimmer (13) electrodes for extraction and acceleration (14) translation motor (15) rotary coupling to atmospheric motor for target rotation (16) gas line (17) suspension rod (18) flange. b) To-scale sectional view of the components around the vaporization block (4). The distance between the ablation target and the hole through which the ablation plasma enters the channel is marked by d_{target}.

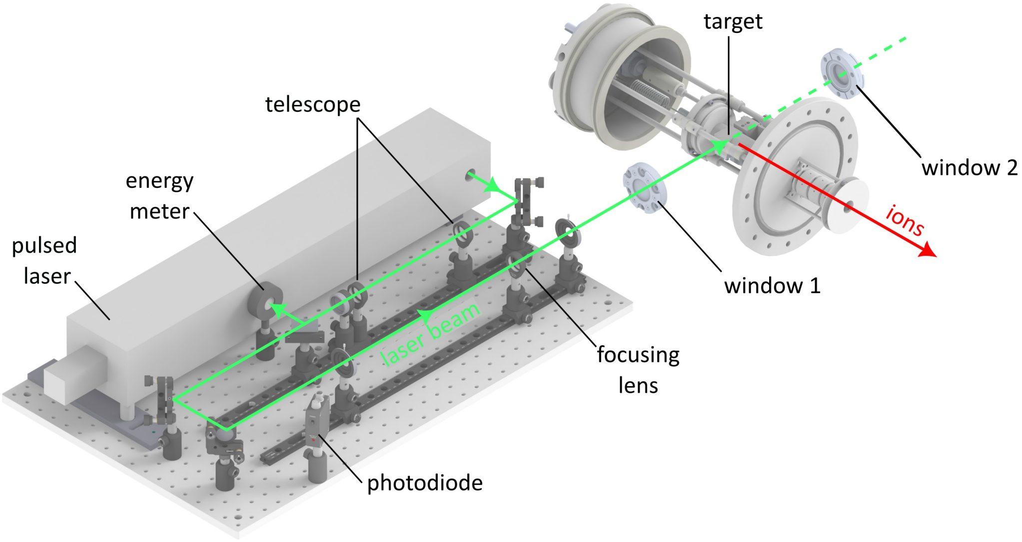

Figure 3.13: Laser setup of the LVAP ion source. For details see the text.

of the glue layer.

After leaving the segmented cluster growth channel (2 mm diameter, 50 mm length), a skimmer[15] (position 12) with 3 mm orifice diameter separates most of the gas from the cluster ions. A set (13) of four cone-shaped electrodes with an orifice diameter of 4 mm extracts the ions and accelerates them gradually (Nüsslein 2018; Schmidt 2018). The last electrode is connected to laboratory ground potential. The ion source can be lifted to a potential with respect to ground, which then defines the final energy of the ions (up to 5 keV). The sign of the extracting and accelerating voltages determines the polarity of the extracted ions. If needed, bias voltages can be applied to the skimmer and the actual ion source unit (exploded view in figure 3.12 a). A voltage applied to the mesh (11) focuses the ion pulse on its way to the skimmer.

Within the LVAP module, the laser setup (see figure 3.13) resides directly next to the ion source vacuum chamber. A Neodymium-Doped Yttrium Aluminum Garnet (Nd:YAG) laser[16] delivers 5 ns laser pulses with up to 130 mJ energy at a wavelength of 532 nm and a pulse rate variable from 1–20 Hz. The pulsed laser beam is widened by an optical telescope and focused with a 400 mm plano-convex lens to an effective spot size of $\sim$ 100 µm at the target. The resulting maximum energy fluence of about $\sim 10^3\ \mathrm{J\,cm^{-2}}$ is far above the calculated ablation threshold of aluminum ($\approx 4\ \mathrm{J\,cm^{-2}}$, Lutey 2013). An energy meter monitors the laser pulse energy. The effective energy at the target is known from a reference measurement behind the focusing lens and after taking into account the transmission factor of the entrance laser window. For alignment and troubleshooting purposes, the laser beam can be coupled out through

---

[15] Model 2 Ni molecular beam skimmer, BEAM DYNAMICS, INC.

[16] SpitLight Compact 200–20 with $M^2 \approx 5$, InnoLas Laser GmbH.

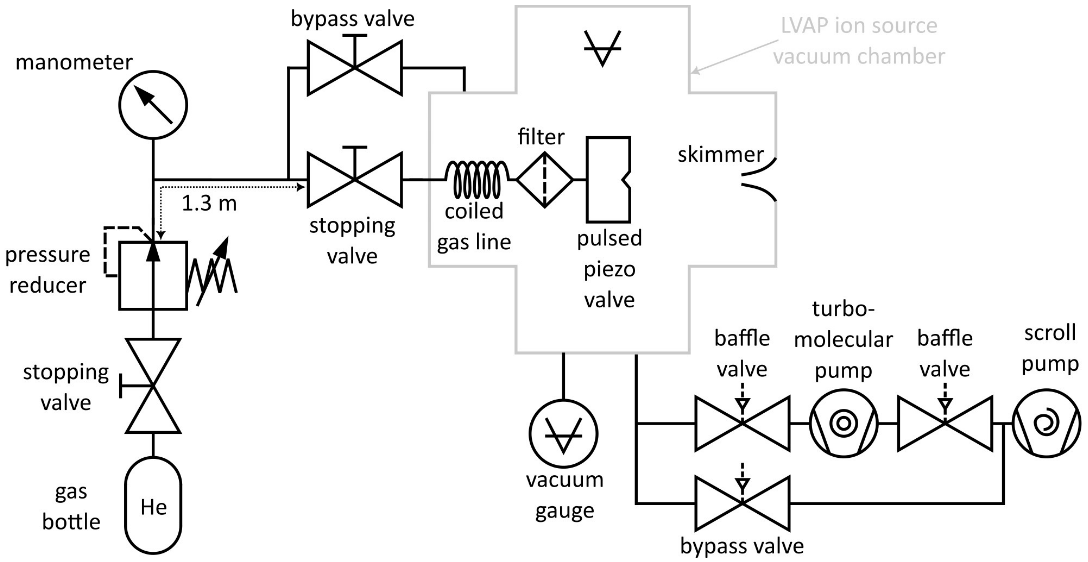

Figure 3.14: Gas line and vacuum setup of the LVAP ion source. For details see the text.

a second window. The ablation target unit is then either removed or positioned such that, without the target disk, the laser beam passes through the target holder and the subsequent tubular rotation axis (position 9 in figure 3.12 b).

A fast photodiode monitors the time structure of the laser pulse and its timing with respect to the trigger of the pulsed valve. It is important to note here that the gas pulse is triggered first and is already in the channel when the laser fires. The laser is thus triggered at a defined time after the pulsed valve trigger. We refer to this time as the Laser Pulse Delay (LPD).

Figure 3.14 sketches the gas line and the vacuum setup of the LVAP source. A thin gas line with a total length of about 2.5 m supplies the pulsed valve with the backing gas. Inside the ion source chamber it features a coiled section of about 0.9 m tube length (see also figure 3.12), where it narrows down to an inner diameter of about 0.9 mm. The coil allows for a flexible longitudinal movement of the ion source block. The gas bottle provides a pressure reducer and a manometer for pressure control. Using the 0.4 m long bypass gas line, the scroll pump can evacuate the pulsed valve body and the gas line until the stopping valve of the gas bottle. Two baffle valves then protect the turbo pump from the high gas load. The skimmer orifice acts as a differential pumping stage, as it is the only connection to the subsequent vacuum chamber during ion source operation. For efficient cleaning of the gas line, a part of it (dotted line with arrows in figure 3.14) can be heated to about 100 °C.

During operation so far, we used 0.5—10 mJ laser pulse energy at the target, 20–170 µs OD of the pulsed valve, 50–150 µs LPD and up to 14 bar absolute backing pressure. The ion production rate is limited by the laser pulse rate. Choosing a 10 Hz production rate turned out to be practical with respect to data acquisition and vacuum pressures in the chamber. Depending on the OD and the backing pressure, we measured $(1.0\text{–}5.5)\times10^{-5}$ mbar in the ion source chamber and $(2.5\text{–}25)\times10^{-7}$ mbar in the subsequent vacuum chamber during ion source operation. With closed pulsed valve, the respective pressures were $(1\text{–}2)\times10^{-7}$ mbar.

3.2.3.3 Anionic mass spectra

Here, we present and discuss example anionic mass spectra obtained at the ISTB (figure 3.3) with the new LVAP ion source (section 3.2.3.2) in the LVAP module. We address mass spectra recorded for two different ablation target materials, namely carbon and aluminum. The *carbon* spectra mainly serve for calibration of the mass spectrometer. Because we had a strong ion signal and clean spectra with this target material from the beginning, little effort was spent on optimization. For the mass spectra recorded with an *aluminum* target, we initially only obtained little signal and found many other components apart from aluminum clusters Al_n^-. In the following, we briefly discuss the carbon spectra. We then elaborate in more detail on the optimization steps towards proper aluminum spectra. We visualize the effect of the final optimization step, which not only allowed us to further increase the ion yield, but also to narrow down the range of possible explanations for the additional components in the spectra. Finally, we assign the components and conclude by comparing the aluminum spectra to the carbon spectra.

The *carbon* spectra are depicted in figure 3.15, where the number of ions is plotted against the mass-to-charge ratio m/q. The parameters of the ion source and the mass spectrometer are given in the caption. It is noteworthy that for optimum ion yield we needed only 0.8 mJ laser pulse energy at the target[17]. This value lies below the range used by Belau et al. 2007 (5–10 mJ for 1.5 mm laser spot size) and is explained by the smaller spot size in our experiment. Also, in this particular setup, the dedicated skimmer was removed, so that the first cone-shaped extraction electrode acted as a skimmer.

For $m/q < 340$ u/e the spectra show clear and distinct peaks mostly appearing every 12 u/e. Due to the limited mass resolution of the mass spectrometer the peaks begin to merge for $m/q > 340$ u/e. The regular spacing allows us to explain almost all peaks by carbon clusters C_n^-. The odd peak at $m/q = 26$ u/e likely results from CN^- or $\mathrm{H_2CC}^-$(masses in table 4.1 in section 4.3.3.2). The carbon anion C^- indicated by the arrow in figure 3.15 b) is not resolved in the spectrum.

As described in section 3.2.1.1, the mass-to-charge ratio results from conversion (see equation 3.1) of the measured magnetic field and a calibration step involving known masses. The carbon spectra yield many peaks which can be clearly assigned even for higher masses. They are thus well suited for the calibration and serve as reference for

---

[17] Flexible graphite foil, $\geq 99.8\%$ purity, 0.5 mm thickness, Merck KGaA

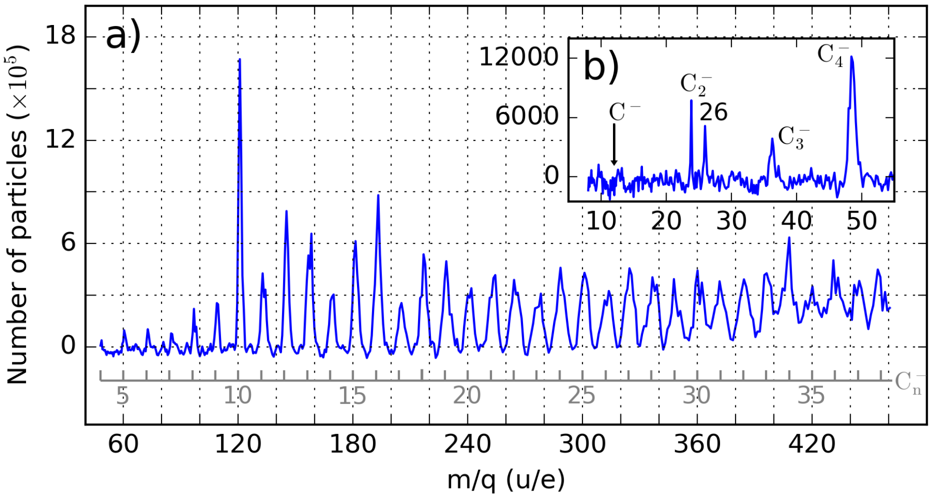

Figure 3.15: Spectra of negative ions produced with an LVAP ion source equipped with a carbon ablation target. The horizontal axes in a) and b) represent the ion mass-to-charge ratio. The grey comb indicates where to expect C_n^- clusters with size n. The spectra were recorded with a) the Faraday cup and b) the channeltron ($U'_\mathrm{in} = 2.7$ kV) of diagnostics 2 of the ISTB. Both spectra were recorded for 5 keV ions, 5 bar He backing pressure, 50 µs opening duration of the pulsed valve, 100 µs laser pulse delay, 0.8 mJ laser pulse energy at the target, 50 mm growth channel length and 49 mm distance between growth channel and skimmer. The horizontal and vertical opening $[x, y]$ of the slits of the mass spectrometer was set to $[20\text{ mm}, 20\text{ mm}]$ (slits 1) and $[8\text{ mm}, 16\text{ mm}]$ (slits 2). Each data point in each spectrum is the mean of 10 individual ion pulses. The vertical axis in b) was calibrated according to the procedure described in section 3.2.1.3 and detailed in appendix A.2.2.

the aluminum spectra. For the calibration we used carbon spectra with better mass resolution (but lower peak intensities) than in figure 3.15.

In contrast to the carbon spectra, we obtained significantly less ion signal when using the *aluminum* target. Hence, we invested significant effort in further optimization. The following steps were most effective: We increased the backing pressure and optimized the Opening Duration (OD) of the pulsed valve, the laser pulse energy at the target, and the Laser Pulse Delay (LPD). Furthermore, we built in a skimmer with a 3 mm orifice (marked red in figure 3.12 a) and reduced the distance between the skimmer and the exit of the growth channel. Contrary to the recommendation by Luria, Christen, and Even 2011[18] we found that the smallest possible distance (4 mm) lead to the highest ion yield. Also, we moved the ablation target as close as possible towards the hole through which the plasma enters the channel (figure 3.12 b).

Apart from increasing the cluster yield, the last step mentioned above also helped

---

[18] Place skimmer at ∼ 1000 nozzle diameters, i.e., 30 cm here. Smaller distances may cause skimmer clogging by gas.

us in the understanding of the observed aluminum spectra. Other measures taken with this intention did not change the anionic spectra significantly. For completeness, we list them subsequently:

- We re-aligned the laser beam by optimizing the transmitted laser pulse energy behind the second laser window (figure 3.13). In order to exclude contaminations resulting from ablation of material from inside the stainless steel laser channel, we then operated the ion source without ablation target. We did not see an ion signal at the exit of the source, which indicated a successful alignment procedure.
- We removed or cleaned lubricated mechanical parts from inside the vacuum chamber (motor, ball bearings) and removed the PTFE spacer attached to the target holder (position 7 in figure 3.12 b).
- We heated and purged the gas line. Only in the cationic spectra (appendix A.4.2) we observed a reduction of components originating from water.
- For the aluminum spectra we used the target holder itself as ablation target. As it is made of an alloy containing mostly Al and in total a few percent of other elements, we compared these spectra to spectra produced from a high-purity Al target with $\leq 0.001\%$ other elements. While we found clear differences in the cationic spectra (appendix A.4.2), the anionic spectra did not differ significantly.
- Applying bias voltages to the ion source block, the skimmer and the mesh did not improve the ion yield significantly. Wrong polarities evidently block the total ion signal after the ion source completely.

The spectra with aluminum target are presented in figure 3.16. For these spectra we used the aluminum alloy target, while it turned out that high-purity aluminum anion spectra look very similar. The upper spectrum (red) in figure 3.16 a) incorporates all described optimization steps, but was taken for the standard distance ($d_{\text{target}} \approx 1.3$ mm) between the ablation target and the entrance hole (1.5 mm diameter) to the channel (see figure 3.12 b). In the lower spectrum (orange) we reduced this distance to $d_{\text{target}} \approx 0.3$ mm, with the underlying idea to allow more of the plasma plume to enter the channel.

Both spectra in figure 3.16 a) show regularly spaced components within the gray bands. The black comb and dotted vertical lines indicate the position of aluminum clusters. In the upper spectrum, the most abundant pure Al cluster component is Al_6^- with about 1200 ions per source pulse. It is present in the lower spectrum as well, but five times more abundant. Here, the maximum of the aluminum cluster distribution is shifted significantly towards higher cluster size, namely Al_{13}^- with about 10^4 ions.

Within many of the gray bands in the upper spectrum, additional components apart from aluminum clusters are present. We identify two distinct patterns indicated by the gray combs: The dark gray comb (named "$\text{Al}_{\text{n}-2}^- + 51$") starts at $m/q = 51$ u/e

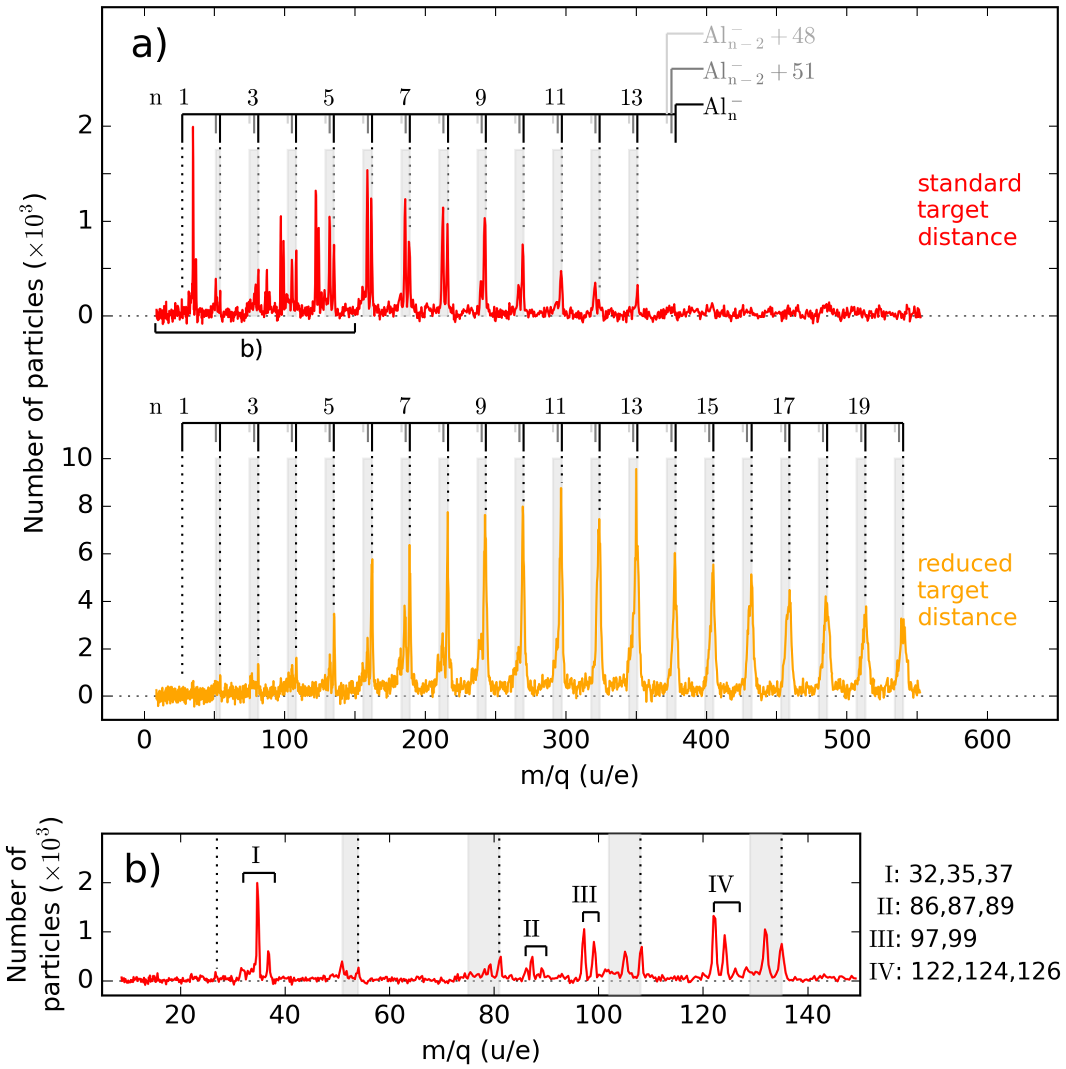

Figure 3.16: a) Spectra of negative ions produced with an LVAP ion source equipped with an aluminum ablation target, which was placed at different distances with respect to the hole through which the plasma enters the channel (see figure 3.12 b). The combs indicate where to expect Al_n^- clusters (black) of size n and other components comprised of $\mathrm{Al}_{\mathrm{n}-2}^-$ and species with either $m/q = 48$ u/e (light grey), or $m/q = 51$ u/e (dark grey). The spectra were recorded for 5 keV ion kinetic energy, 10 bar He backing pressure, 70 µs opening duration of the pulsed valve, 114 µs laser pulse delay, 3.2 mJ laser pulse energy at the target, 50 mm growth channel length and 4 mm distance between growth channel and skimmer. The horizontal and vertical opening $[x, y]$ of the slits of the mass spectrometer was set to [2 mm, 2 mm] (slits 1) and [2 mm, 2 mm] (slits 2). b) Magnified excerpt of the mass spectrum for standard target distance. The assigned mass-to-charge ratios in the respective groups I–IV are stated in the units u/e. The assignment is made in the text. Each data point in each spectrum is the mean of 10 individual ion pulses. The vertical axes were calibrated according to the procedure described in section 3.2.1.3 and detailed in appendix A.2.2. We used 3 kV (red) and 2.85 kV (orange) channeltron input voltage U'_in.

and continues towards higher m/q with more components spaced by 27 u/e, which corresponds to the mass-to-charge ratio of aluminum. The components of this comb significantly contribute to the spectrum and are often more abundant than the neighboring aluminum cluster peaks. In contrast, the components of the light gray comb (named "$\mathrm{Al}_{\mathrm{n}-2}^{-} + 48$") are by far less abundant and appear much less regularly. The upper spectrum also features components not covered by the gray bands, i.e., without the 27 u/e periodic pattern. They are magnified in figure 3.16 b) and appear in four groups.

Comparing the upper and the lower spectrum bears two observations: The non-periodic components outside the gray bands vanish almost completely in the lower spectrum. Furthermore, within the gray bands of the lower spectrum, the aluminum cluster components $\mathrm{Al}_{\mathrm{n}}^{-}$ now dominate in abundance without exception.

As mentioned above, we reduced the target distance in order to bring more ablated material into the channel and enhance the production of aluminum clusters. The observations not only suggest that this idea was a success, but also that the non-periodic components likely do not result from the target, but from somewhere else. The same may be true for the non-aluminum species which we suspect to be contained in the periodic components labeled by "$\mathrm{Al}_{\mathrm{n}-2}^{-} + 48$" and "$\mathrm{Al}_{\mathrm{n}-2}^{-} + 51$". A suggestive explanation for these components would be clusters with two units of Al replaced by O_3 ($m/q = 48$ u/e) or $(OH)_3$ ($m/q = 51$ u/e). As the metal parts of the ion source block (see figure 3.12) were cleaned regularly and thoroughly without a clear effect, the origin of the contaminations likely lies upstream of the point where the gas pulse encounters the plasma plume. Possible candidates responsible for contaminations are thus the PTFE gasket, the components inside of the commercial pulsed valve body, or the long and thin gas line (figure 3.14).

We now assign the unknown components based on species found in the NIST Standard Reference Database (Linstrom 1997). Remarkably we have not found matches in all cases. The suggested assignment is based on the above assumption that the contaminants originate from the PTFE gasket, the pulsed valve or the gas line. With regard to species containing N, O and H, the assignment is supported by traces of water and atmospheric air[19] found in the cationic aluminum spectra (appendix A.4.2). Here, it is important to remember that the overall neutral plasma contains electrons, neutrals as well as cations and anions (section 3.2.3.1). Until charge separation by electrical fields occurs further downstream, all species except for fast electrons (Himmelsbach 2022) are in principle available for chemical reactions, so that cationic and anionic species may form at the same time.

The dark gray comb commences at $m/q = 51$ u/e, which may be explained by $(\mathrm{OH})_3^-$, and continues with $\mathrm{Al}_{\mathrm{m}}(\mathrm{OH})_3^-$. The components of the light gray comb may result from $\mathrm{Al}_{\mathrm{m}}\mathrm{O}_3^-$. Most components of group II–IV from figure 3.16 b) may be

---

[19] Approximate composition (Cox 2002): 78 % N_2, 21 % O_2, 1 % other including water vapor

explained by combinations of Al, O and H, for instance Al_4O^- at $m/q = 124$ u/e. A continuous series of pure water clusters $(H_2O)_k^-$ at $(m/q)_k = k \times 18$ u/e is not visible. The component at $m/q = 89$ u/e may result from $H_9O_5^-$. The peak at $m/q = 122$ u/e is explained by Al_4N^-. In group I, we identify the component at $m/q = 32$ u/e as O_2^-. The ratio of the peaks at $m/q = 35$ u/e and $m/q = 37$ u/e approximately fits the isotopic ratio of ^{35}Cl and ^{37}Cl, which is about 3:1 (Meija et al. 2016). In other anionic spectra obtained with the aluminum target, we consistently observed a ratio around this value, but we did not see these peaks in the cationic aluminum spectra (appendix A.4.2). As neutral chlorine is the element with the largest known electron affinity (≈ 3.6 eV, Rienstra-Kiracofe et al. 2002) and at the same time has a very large ionization energy (≈ 13 eV, Yang et al. 2015) the explanation of the 35 u/e and 37 u/e peaks by Cl^- does not seem implausible.

If we compare the anionic spectra taken for the different target materials, the question arises why the additional components are not visible in the carbon spectrum. For instance, in the carbon spectrum in figure 3.15 b) we would expect to see a peak on the order of 10^4 ions[20] at $m/q = 35$ u/e. On the one hand, one may speculate that the underlying plasma chemistry may be different for carbon. On the other hand, the findings may be explained by the same effect as observed for the aluminum spectra in figure 3.16 a): The abovementioned standard target distance is defined by the PTFE spacer (see figure 3.12). While it is 1.3 mm if the aluminum target holder itself is used for ablation, it is ≤ 0.8 mm if the 0.5 mm thick carbon target is glued onto the target holder. This reduced distance may already sufficiently suppress components not originating from the target material, as observed from comparison of the two spectra in figure 3.16 a).

To summarize, we observed that the LVAP ion source is capable of producing cluster anions from different target materials. While this worked almost effortlessly for carbon, substantial optimization efforts had to be made towards a broad range of aluminum clusters with good abundance.

3.2.3.4 Methods to optimize the Al_4^- cluster yield for the CSR

As small aluminum clusters and in particular Al_4^- are of interest for experiments at the CSR, we attempted to cultivate this species specifically. In the course of the Al_4^- yield optimization, we also learned more about the ion source conditions. In the following, we summarize our findings. Since the cultivation measures are not yet exhausted, we conclude by giving further ideas.

---

[20] The dedicated skimmer together with the smallest possible distance between the skimmer and the end of the growth channel give about a factor 4 more ions after the magnet, while the reduced slit settings for the aluminum spectra give about 20 time less ions (see figure 3.5 a). Application of these factors on the peak at $m/q = 35$ u/e in the upper spectrum in figure 3.16 a) results in the estimated 10^4 ions.

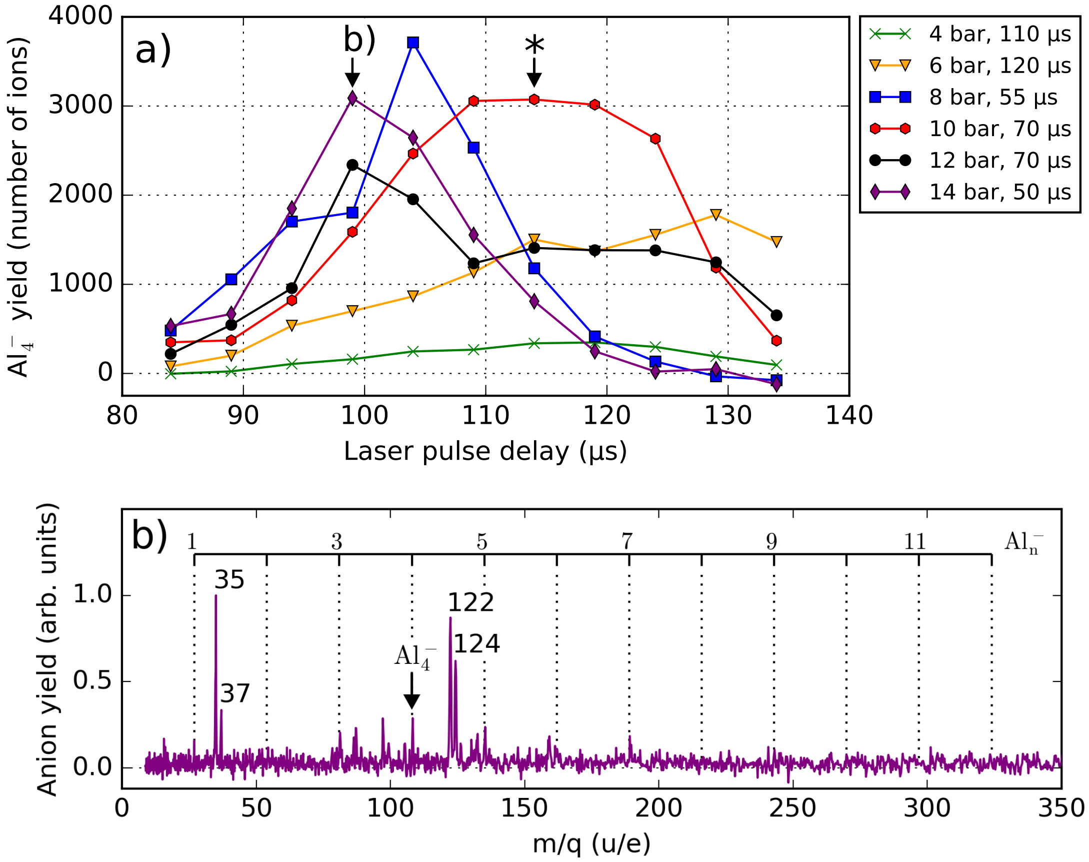

Figure 3.17: a) Number of Al_4^- ions per source cycle against laser pulse delay for 3.3 mJ laser pulse energy at the target. The legend assigns the respective backing pressures and opening durations of the pulsed valve. The mass spectrometer was set to $[x, y] = [2\text{ mm}, 2\text{ mm}]$ (slits 1) and $[2\text{ mm}, 2\text{ mm}]$ (slits 2), and 2.9 kV (6–14 bar) and 3.1 kV (4 bar) channeltron input voltage U'_{in}. The data point marked with a star has the same mass spectrometer and ion source settings as the upper spectrum in figure 3.16 a). b) Mass spectrum taken for the settings of the data point marked with “b)” in a). The four highest peaks are labeled by their mass-to-charge ratios.

For Al_4^- cultivation we employed a fresh target, and started with the ion source and mass spectrometer settings used for the upper aluminum spectrum in figure 3.16 a), i.e., also using the standard target distance ($d_{\text{target}} \approx 1.3$ mm). Using the spectrometer magnet we maximized the Al_4^- signal at the channeltron (see figure 3.3). For fixed laser pulse energy (3.3 mJ), backing pressure and OD of the pulsed valve, we then recorded the Al_4^- yield as function of the relative timing (LPD) at which the laser-ablated material is injected into the gas pulse. We repeated this procedure for different backing pressure and OD settings.

The resulting data sets are plotted against the LPD in figure 3.17 a). The legend states the backing pressure and the OD of the pulsed valve. We observe that almost all data sets feature a similar behaviour: The signal rises, culminates more or less sharply and (except for the 6 bar signal) decreases again. Independent of the backing pressure, signals with similar OD have a similar width. As the OD of the pulsed valve determines the duration of the gas flow, this observation seems plausible. With regard to the maximum yield, we find that most of the high-pressure data sets (8 bar, 10 bar, 14 bar) have the highest yield (> 3000).

For the ion source and spectrometer settings of one of the data points with > 3000 ion yield (marked with "b)") we recorded the mass spectrum presented in figure 3.17 b). Here, it becomes apparent that Al_4^- is now the most abundant Al_n^- cluster species and that, compared to figure 3.16 a), larger cluster species are strongly suppressed. The origin of the other peaks in the spectrum was already discussed above. The four highest peaks in figure 3.17 b) are labeled by their respective mass-to-charge ratios. In the spectra in figure 3.16 we assigned them to $^{35}\mathrm{Cl}^-$, $^{37}\mathrm{Cl}^-$, $\mathrm{Al_4N^-}$ and $\mathrm{Al_4O^-}$, which are either not clusters or based on Al_4 as opposed to other Al_n. Since in figure 3.17 b) we created conditions where clusters except for Al_4^- do not seem to form efficiently, observing the latter two of these components is not surprising.

As clusters condense better for lower temperatures of the ablation plasma, our observations suggest that in figure 3.17 b) the plasma is hotter than in figure 3.16. There, large Al_n^- clusters dominate and even larger clusters form when we inject more material into the gas pulse (standard vs. reduced target distance). Our assumption about the higher plasma temperature in figure 3.17 b) is corroborated by the fact that even He^+ ions, needing very high ionization energy (≈ 24.6 eV, Kandula et al. 2010), are present in the cationic aluminum spectra, which were recorded for comparable ion source settings and are discussed in appendix A.4.2.

It is to be noted that the ion source settings of the spectra with cold plasma (figure 3.16) as well lead to maximum Al_4^- yield > 3000, i.e., comparable to the maximum yield in figure 3.17 a) (data point marked with star). Hence, the Al_4^- peak may be cultivated in a number of ways, and under completely different ion source conditions.

In principle, nothing restrains us now from bringing the LVAP module to the 300 kV ion source platform and installing it at the position of IS 1 (see figure 3.6). As a next step towards optimization, we now estimate the number of ions available for CSR experiments, based on a yield of 3000 ions. Here, we consider several factors: Taking into account

- the increased ion yield (factor 20–50) due to missing slits on the 300 kV ion source platform, estimated from the ion yield with various slit settings of the ISTB (see figure 3.5 a),
- the transmission $T_\mathrm{meas} = (69 \pm 8)\%$ (equation 3.2) of the electrostatic branch of the 300 kV ion source platform,

- the 60% transmission efficiency[21] of the transfer beamline from the 300 kV ion source platform to the CSR (figure 3.2),
- and the injected fraction (30–75%) of a typical LVAP ion pulse (see figure 3.5 b)

we expect to have 2–17 times more ions directly available for CSR experiments compared to the ion numbers from the mass spectra taken with aluminum target at the ISTB (figure 3.16). This corresponds to (6–51)×10^3 Al_4^- ions stored in the CSR. For the experiments with hot aluminum clusters from a MISS ion source we typically stored about 5×10^6 Al_4^- ions and about three times less Al_5^- ions. Compared to these values, the LVAP ion source delivers about two to three orders of magnitude less Al_4^- ions.

The measures described above do not yet exhaust the repertoire of possible improvements:

- Strictly speaking, for each data point in figure 3.17 a) one would have to vary the laser pulse energy systematically.
- Even though the Al_4^- peaks of the two spectra in figure 3.16 a) do not differ significantly in intensity, reducing the target distance would be a logical next step.
- Furthermore, we have not yet investigated the effect of different laser spot sizes on the ablation target. Naively, we would expect more material to be ablated for a larger spot size while keeping the energy fluence constant.
- As a longer growth channel results in larger clusters and more material lost at the channel walls, shortening the channel should favor the formation of smaller clusters and at the same time increase the overall ion transmission through the channel.
- While the bias voltages at the ion source block, the skimmer and the mesh do not significantly improve the total ion output, this may not be the case for the Al_4^- peak alone.
- A more substantial change would be to improve the extraction of the gas pulse from the pulsed valve and its transport to the vaporization block. The current geometry may cause turbulences in the gas pulse, which may negatively affect all subsequent processes. The in-house-built valve appears to be optimized in this regard (shorter distance to target, as depicted in appendix figure A.6). For this reason and due to the lack of performance data in terms of absolute ion output with the in-house-built valve, testing the behavior with this valve is advisable.
- As the CSR stores only a slice of the ion pulse (see figure 3.5 b), trying to shape the pulse in time may be worthwhile.

---

[21] Estimated from measured transmission efficiencies for different ion species (m/q =3–135 u/e) and kinetic energies (50–300 keV).

- Since the pulse rate of the LVAP ion source can be as high as 20 Hz, ion accumulation prior to storage in the CSR may also be considered.
- If the above measures do not lead to a sufficient Al_4^- yield, one may think about using an external electron source as in Weber 2005, which may result in a more than tenfold cluster anion yield.

3.2.3.5 Conclusion

We presented a new LVAP ion source setup dedicated to supplying the CSR with cold cluster anions (section 3.2.3.2). We showed that the new ion source version is capable of producing carbon clusters C_n^- as well as aluminum clusters Al_n^- (section 3.2.3.3). While we obtained carbon clusters almost straightforwardly in significant abundance, we had to make substantial efforts for obtaining a broad range of aluminum clusters with good abundance. We successfully improved the aluminum cluster yield and strongly suppressed additional unwanted peaks in the spectra. Also, we narrowed down the origin of these peaks to specific parts of the ion source setup. In a next step, we may now identify the factual contaminant carriers.

As hot Al_4^- provided by a MISS ion source is currently being studied at the CSR, and we aim at providing cold Al_4^- ions, we cultivated this specific ion species by varying a number of LVAP ion source parameters and estimated the number of cold Al_4^- clusters directly available for CSR experiments (section 3.2.3.4). At present, an improvement of at least a factor of 100 would be needed for efficient measurements at the CSR. Motivated by this result, we assessed that there are still many opportunities for up to order-of-magnitude improvements. A promising next step is to implement the source at the CSR to run further tests, e.g., to verify the ion number estimates and to perform high-resolution mass spectrometry in the storage ring. The next section 3.2.4 discusses the possibilities of such storage ring operation.

3.2.4 Molecule identification by precision mass spectrometry and photodetachment

The CSR can be operated in an isochronous mode, and thus be used as a Time-of-Flight (ToF) mass spectrometer with a mass resolution of $\Delta m/m < 10^{-5}$ (Grieser et al. 2022). This resolution allows to distinguish even molecular isobars in the stored beam, with typical mass differences of $\Delta m/m \leq 10^{-4}$ (Wang et al. 2021). This is very practical for, e.g., characterizing the output of ion sources and identifying possible contaminants of ion beams used for experiments at the CSR. Within this thesis the Isochronous Time-of-Flight (ISO-ToF) mode is used for the H_2CC^- project further discussed in chapter 4. We employ the technique as described by Grieser et al. 2022, though with a different readout, which provides even more information about the stored ion beam.

The idea behind ToF mass spectrometry is a measurement of the time needed for particles of fixed energy E to travel over a fixed distance S. The acquired time T scales with the particle mass m as

$$m = \frac{2E}{S^2}\,T^2. \tag{3.3}$$

If the particle mass is unknown, its flight time can be compared to the flight time T_0 of a reference particle with known mass m_0. The unkown mass m then results from the relation

$$\frac{T}{T_0} = \sqrt{\frac{m}{m_0}}. \tag{3.4}$$

The limiting factor for such mass measurements is the spread of the kinetic energies of the particles, given, e.g., by the varying potential at which the ions are created inside the ion source. Storage rings can overcome the energy spread limitation by isochronous operation. In this mode the storage ring ion-optical elements are adjusted such that the dispersion (orbit length dependence on the particle momentum) compensates the energy effects such that particles of the same mass keep equal revolution time T, independent of their kinetic energy E. Isochronous operation of an electrostatic storage ring was first achieved at the CSR (Grieser et al. 2022) during the H_2CC^- experimental campaign (chapter 4).

The measurement itself is performed by injecting a short ion bunch into the storage ring. The ion bunch fills only a small fraction of the circumference (∼10%). When stored, the ions start to separate by their mass, so that under isochronous conditions multiple bunches arise over many revolutions, one for each particle mass. Measuring the flight times and the separation of the bunches in time then provides the information on the masses of the stored ions.

In Grieser et al. 2022 the time structure of the ion beam is probed by a detector signal, which results from products of neutralization processes of the stored ion beam. These can be induced by collisions of ions with the rest gas (CED) or by continuous-wave

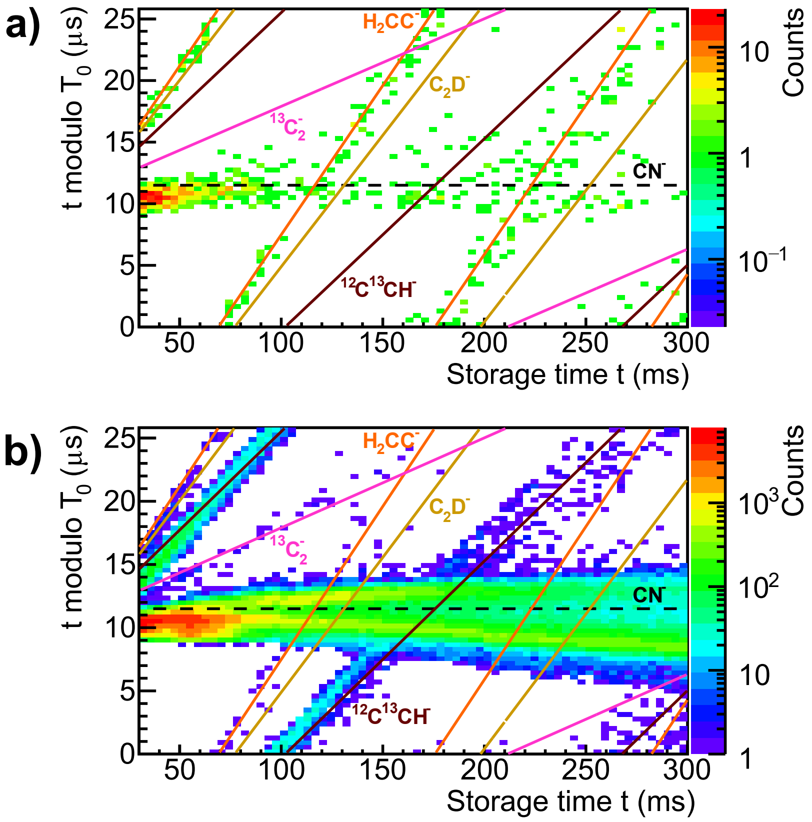

Figure 3.18: ISO-ToF mass spectra for a 250 keV ion beam with $m/q \approx 26$ u/e stored in the CSR. Here, $T_0 \approx 26$ µs is the revolution time of the reference ion CN$^-$ (black dashed line). The solid lines indicate where to expect traces of other ion species. The displayed counts result from a) neutral pulsed-laser photodetachment events recorded with the NICE detector and b) part of the ion beam dumped directly on the COMPACT detector. For more details see the text.

laser irradiation (photodetachment, photofragmentation), and are potentially species-dependent. Here, we use alternative signal sources: On the one hand, we employ pulsed-laser photodetachment for neutralization. On the other hand, instead of collecting ion beam reaction products indirectly, we directly collect a small fraction of the stored ion beam.

At the CSR, the single-particle counting detectors can be used to determine the time structure of the stored ion beam. To this end, the detector data can be represented as a 2D histogram in the so-called ISO-ToF mass spectrum, as depicted in figure 3.18 for two example spectra of a 250 keV anion beam with $m/q \approx 26$ u/e. Each spectrum assumes a chosen reference mass m_0 with a corresponding revolution time T_0. Here, it is the ion CN$^-$ with $m_0 = 26.00362$ u and $T_0 \approx 26$ µs (black dashed line). The horizontal axis represents the storage time t, i.e., the time between the ion injection and the detection of the particle on the detector. On the vertical axis is plotted the particle detection time within given reference particle revolution, obtained as t modulo

T_0. In this way the ion beam structure around the ring (vertical axis) can be monitored as a function of flight time (horizontal axis). As depicted in figure 3.18, particle bunches of individual masses create line-like patterns in such a mass spectrum, corresponding to the increasing separation of the bunches at increasing storage times (flight distances). Using equation 3.4, the slopes of the individual lines scale as

$$\frac{\Delta T}{T_0} = \frac{\Delta(\sqrt{m})}{\sqrt{m_0}}, \tag{3.5}$$

where $\Delta T = T - T_0$ and $\Delta(\sqrt{m}) = \sqrt{m} - \sqrt{m_0}$. The slopes can therefore be used for deriving the mass difference with respect to the chosen reference particle of mass m_0. Note that in figure 3.18 the relative mass difference between the lightest species CN^- and the heaviest species H_2CC^- is $< 5 \times 10^{-4}$ (see table 4.1 in section 4.3.3.2) .

In figure 3.18 a) the NICE detector (see figure 3.1) collects neutral products of pulsed-laser photodetachment at 2.33 eV photon energy. Compared to Grieser et al. 2022, where a continuous-wave laser is used for signal enhancement, the pulsed laser allows to discriminate against the events resulting from the continuous neutralization due to collision with the residual gas. With regard to the photodetachment thresholds of the individual species (EA in table 4.1) we would only expect a photodetachment signal from H_2CC^- (EA $\approx$ 0.5 eV). However, we also see a signal along the line of CN^-(EA $\approx$ 3.9 eV). Also, the signal along the CN^- line decays as the storage time t progresses, which hints at an excited metastable state of CN^-. This method thus allows to identify all species contributing to a photodetachment signal for a given photon energy.

In figure 3.18 b) a part of the stored ions is directly collected by the COMPACT detector (see figure 3.1). It is positioned close to the stored beam and such that only ions at extreme orbits, i.e., the ion beam halo, are collected, while the overall lifetime of the main beam remains nearly unaffected. An advantage of the direct ion detection by COMPACT is the proportionality of the acquired signal to the fractions of the individual ion species. In chapter 4 we use this method to infer the relative fractions of the ion beam components. Due to the higher allowed rate of impinging particles than at NICE, the acquisition time can be as low as 0.3 h (instead of > 10 h for NICE).

With these methods in hand, the output of ion sources may be analyzed with high resolution prior to and during experimental campaigns, and systematically optimized. In fact, this method has already become a standard analysis step during CSR experiments.

3.2.5 Summary of achievements

We presented the results of experimental developments for improving the supply of the CSR with beams of positively and negatively charged atoms and molecules, with the focus on negative ions of clusters. The output of pulsed and low-intensity ion sources can now be analyzed using a dedicated test bench (ISTB) equipped with counting detectors, independent of and prior to their operation on the CSR high voltage platforms (section 3.2.1). The 300 kV ion source platform of the CSR, previously limited to one ion source at a time, may now house up to four more ion sources of different types at its electrostatic branch, and efficiently provide their ion beams for experiments (section 3.2.2). For experiments on cold anionic clusters, an LVAP ion source module was developed, which can be coupled to the ISTB as well as the 300 kV platform beamline (section 3.2.3). By means of high-resolution mass spectrometry and pulsed-laser photodetachment, the CSR is now able to identify isobaric anion species in excited states, as they may respond to photon energies which do not photodetach the ground state. Furthermore, direct collection of a small fraction of the stored ion beam allows to determine the relative fractions of all ion beam components. This further augments the possibilities for precisely characterizing the output of anion sources (section 3.2.4). In a nutshell, the presented developments considerably improve the possibilities for studying the stability of negative ions with the CSR.

Chapter 4

Vinylidene anion stability in a cryogenic environment

After having established the CSR facility as an experimental toolbox for physical chemistry studies on gas phase anions (chapter 3), we ourselves use it for an experiment: In this chapter we investigate the stability of the vinylidene anion H_2CC^- in a cryogenic environment. To this end, we store an ensemble of H_2CC^- ions in the CSR and employ photodetachment for monitoring the H_2CC^- abundance in the storage ring.

4.1 Vinylidene study at the CSR

As detailed in section 2.2 and 2.3, a room-temperature storage ring experiment measured a lifetime of $\tau_0 = 110^{+180}_{-40}$ s for the electronic and vibrational ground state vinylidene anion H_2CC^- (Jensen, Pedersen, and Andersen 2000). The lifetime was obtained indirectly by extrapolation from collision-limited (~ 10 s) ion beam lifetimes of H_2CC^- in dependence on the residual gas pressure, and comparison to the collision-free lifetime of an intrinsically stable reference ion. The state-of-the-art cryogenic electrostatic storage ring CSR (chapter 3) offers the possibility to measure lifetimes of this order of magnitude directly and more precisely, being much less affected by ion beam decay due to residual gas collisions. Here, we outline the idea of a lifetime measurement of ground state H_2CC^- stored in the cryogenic environment of the CSR.

The extremely low residual gas density of the CSR allows to observe stored ion beams on timescales of several 10^3 s. Under these conditions a stored beam of intrinsically stable ions typically decays at a rate of $k_s \approx 10^{-3}\ \mathrm{s}^{-1}$ or lower (Hahn et al. 2016). A beam of vinylidene anions, which is subject to the same loss rate k_s in addition to its intrinsic decay rate k_0, would then decay at a rate of $k_0' = k_0 + k_s$. Using the value $k_0 = 1/\tau_0 = (0.009 \pm 0.006)\ \mathrm{s}^{-1}$ from Jensen, Pedersen, and Andersen 2000, we get $k_0' \approx 0.010\ \mathrm{s}^{-1}$ for the potentially observed decay rate of the stored H_2CC^- beam in the CSR. Such directly measured value would still overestimate the intrinsic decay rate k_0, but its potential difference to k_0 that could be obtained with the CSR beam decay rate k_s would already be smaller than the uncertainties stated by Jensen, Pedersen, and Andersen 2000.

The remaining small systematic uncertainty partly results from ion loss due to Collisional Electron Detachment (CED). As, compared to the room-temperature measurement, this effect is now orders of magnitude smaller, loss mechanisms neglected in the room temperature experiment would already be relevant as well. We listed possible candidates for such effects while discussing the room-temperature H_2CC^- study in section 2.2, where the remaining small uncertainty enters via the reference ion. Thus, due to the different mass of the reference ion there may be potentially mass-dependent loss mechanisms related to the design of the storage ring itself, e.g., higher-order components in the confining electrical fields of the ring orbit (point **A** in section 2.3). Separate storage of H_2CC^- and the reference ion involves changing the settings of the separating magnet of the ion source. This may alter the initial storage conditions and potentially result in different observed lifetimes for the same ion species (**B**). The photodetachment rate due to photons from the ambient blackbody radiation field may play a role as well (**C**).

With the CSR, we are able to address these points: The potentially mass-dependent effects from point **A** may be quantified by choosing an isobaric (mass difference $\Delta m/m \leq 10^{-4}$, Wang et al. 2021) and intrinsically stable reference ion. Point **B** may be dealt with by storing both H_2CC^- and the isobaric reference ion at the same time and probing the respective ion abundance by ion-specific photodetachment. To directly check the isobaric components of the stored ion beam, as well as their contributions to the photodetachment signal, we can employ the CSR as high-resolution ToF mass spectrometer, as described in section 3.2.4. We expect point **C** to be negligible, as the CSR provides a radiatively cold environment with strongly suppressed blackbody radiation compared to a room-temperature environment.

The next section 4.2 discusses the specific experimental implementation of this idea at the CSR using simultaneous storage of H_2CC^- and CN^-, and pulsed-laser photodetachment, as well as the modeling of the ion beam decay, which takes into account possible quantifiable ion loss mechanisms.

4.2 Experiment preparation

The following section describes the experimental setup along with all preparations and considerations necessary for conducting the experiment on the stability of the ground state H_2CC^- ion. Section 4.2.1 introduces the experimental setup. Section 4.2.2 describes the relevant technical instances of the CSR facility and the timing scheme of the experiment. Based on the experimental setup, we model the decay of the stored ion beam components in section 4.2.3. In section 4.2.4 we explain how to connect the model to the measured quantities and to obtain the variables related to the ground state H_2CC^- stability.

4.2.1 Experimental setup

In this section the experimental setup and the given experimental parameters for conduction the H_2CC^- lifetime experiment are introduced. The experimental idea is to store the ground state H_2CC^- ion *and a stable isobaric reference ion* in the CSR, and to monitor their decay in the ring by means of photodetachment with lasers and collecting the resulting neutrals at a single-particle counting detector. The observed decay rate of the H_2CC^- ion contains information about its intrinsic lifetime and about external effects. The purpose of the isobaric reference ion is to quantify most external effects and, by comparing the decay of both ion species, to enable determination of the intrinsic lifetime of the ground state H_2CC^- ion.

In order to suppress systematic effects in time, such as the drifting ring temperature and the resulting changes in the residual gas density inside the experimental vacuum chambers, both ions are stored and observed simultaneously. To account for effects which may be related to the mass-to-charge ratio, the reference ion has to have a mass-to-charge ratio as similar as possible to H_2CC^-($m/q = 26.01620$ u/e^1). The CN^- ion ($m/q = 26.00362$ u/e^1) is chosen for this purpose. Conveniently, it can be provided by the same ion source.

A mixed beam of H_2CC^- and CN^- is produced on the 300 kV ion source platform with a Metal Ion Sputter Source (MISS). It is accelerated to a final kinetic energy of 250 keV per elementary charge, transported to and injected into the CSR. The setup of the lifetime measurement is sketched in figure 4.1. Two pulsed lasers are used to probe the decay of the two ion species by photodetachment. The resulting neutral counts on the detector scale with the intensity of the corresponding ion beam type. For a more quantitative discussion, refer to section 4.2.4. A pulsed nanosecond Neodymium-Doped Yttrium Aluminum Garnet (Nd:YAG) laser[2] with a photon energy of 2.33 eV (532 nm) photodetaches the H_2CC^- ion (EA$\approx$ 0.49 eV) at a rate of 10 Hz. This laser is referred to as VISible laser (VIS). The second laser is a pulsed Optical Parametric

---

[1] Mass-to-charge ratio according to Wang et al. 2021

[2] NEW WAVE RESEARCH Polaris III-10 Hz

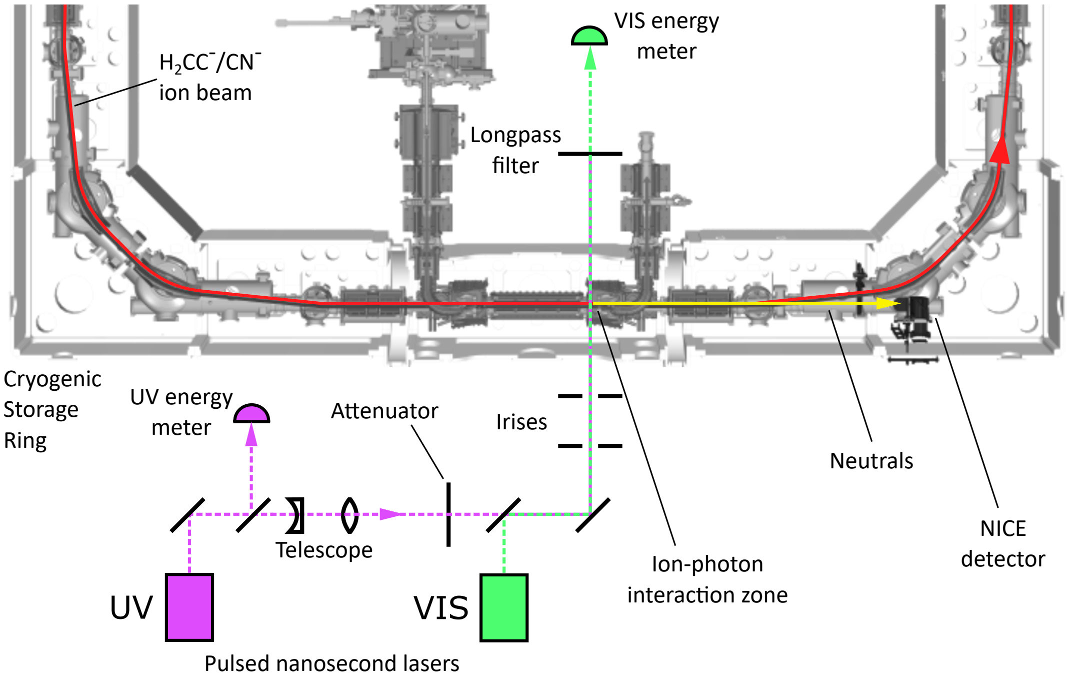

Figure 4.1: The experimental setup for the H_2CC^- lifetime measurement is presented.

Oscillator (OPO)[3] and referred to as UltraViolet laser (UV). It generates photons with an energy of 4.00 eV (310 nm) and photodetaches both the H_2CC^- and the CN^- ion (EA≈ 3.86 eV) at a rate of 20 Hz (EAs from table 4.1 in section 4.3.3.2).

The laser beams (green and purple dashed lines) are combined with a dichroic mirror, guided towards and coupled into the CSR, where they overlap with the stored ion beam at a 90° angle. Ions and photons can interact and the laser beams are then decoupled from the CSR. A longpass filter blocks the UV beam and a pyroelectric energy meter[4] measures the transmitted pulse energy of the VIS laser. The stability of the UV beam is monitored before the CSR, where about 10% of the initial laser pulse energy is branched off with a beam splitter and measured with a second pyroelectric energy meter[5].

The neutrals created from photodetachment in the interaction region are no longer affected by the ion optical elements and fly ballistically (yellow arrow) towards a MicroChannel Plate (MCP) detector (NICE), where they are counted. The distance between the interaction region and the NICE detector is about 3.3 m. For the given beam energy and an ion mass-to-charge ratio of 26 u/e, this corresponds to a Time-of-Flight (ToF) of about 2.4 µs.

To ensure that both laser beams address the same fraction of the ion beam, they are carefully matched in terms of their divergence, size and path through the CSR. To

---

[3] EKSPLA NT342B
[4] Gentec QE25LP-S-MB
[5] Gentec QE12LP-S-MB

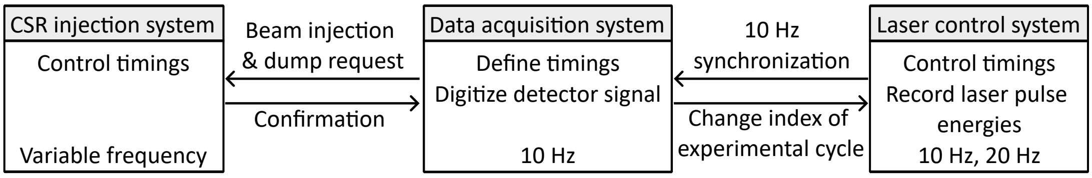

Figure 4.2: The control instances of the CSR facility and their interplay are outlined.

this end, the UV beam is shaped with a telescope. In addition, a pair of irises with a distance of 185 mm and a 5 mm aperture radius is placed directly before the 90° laser port.

In each experimental cycle, about 2×10^7 ions are stored. The CN^- ion is by far the most abundant beam component (98.9%), while there is only a small fraction ($< 0.03\%$) of H_2CC^- (for details, see section 4.3.3 and table 4.1). The UV-induced photodetachment signal at the detector is thus dominated by CN^- and gives an independent estimate of the CN^- component in first order.

In order to obtain a reasonable signal at the NICE detector, the VIS laser pulse energy in the interaction region is chosen to be about 3 mJ. For the UV laser, the pulse energy in the interaction region has to be decreased to 30 µJ in order not to produce too many neutrals in the interaction region and hence saturate the detector. As a result, the transmitted UV pulse energy after the CSR is too low to be monitored with reasonable precision. For this reason, it is monitored shortly after the UV laser output and attenuated subsequently. The VIS and UV laser pulse energies in the interaction region are estimated from calibration measurements and the transmission specifications of the CSR sapphire viewports.

4.2.2 Timing scheme

In order to observe the decay of the stored ion beam components with pulsed lasers and the single particle counting detector, the individual CSR control and data-acquisition system modules have to be synchronized with respect to each other. In the following, the relevant modules and the timing scheme of the H_2CC^- lifetime experiment are outlined.

As shown in figure 4.2, there are three independent modules which communicate among each other mostly via trigger signals: The CSR injection system[6] handles the injection, storage and dumping of ion beams provided by the ion source platforms. The Data AcQuisition (DAQ) system requests a beam from the injection system, records the pulse-heights and timings of the events at the counting detector, and determines after which storage time the stored beam is dumped in order to start a new experimental

---

[6] In-house solution based on 20 MHz ATmega microcontrollers

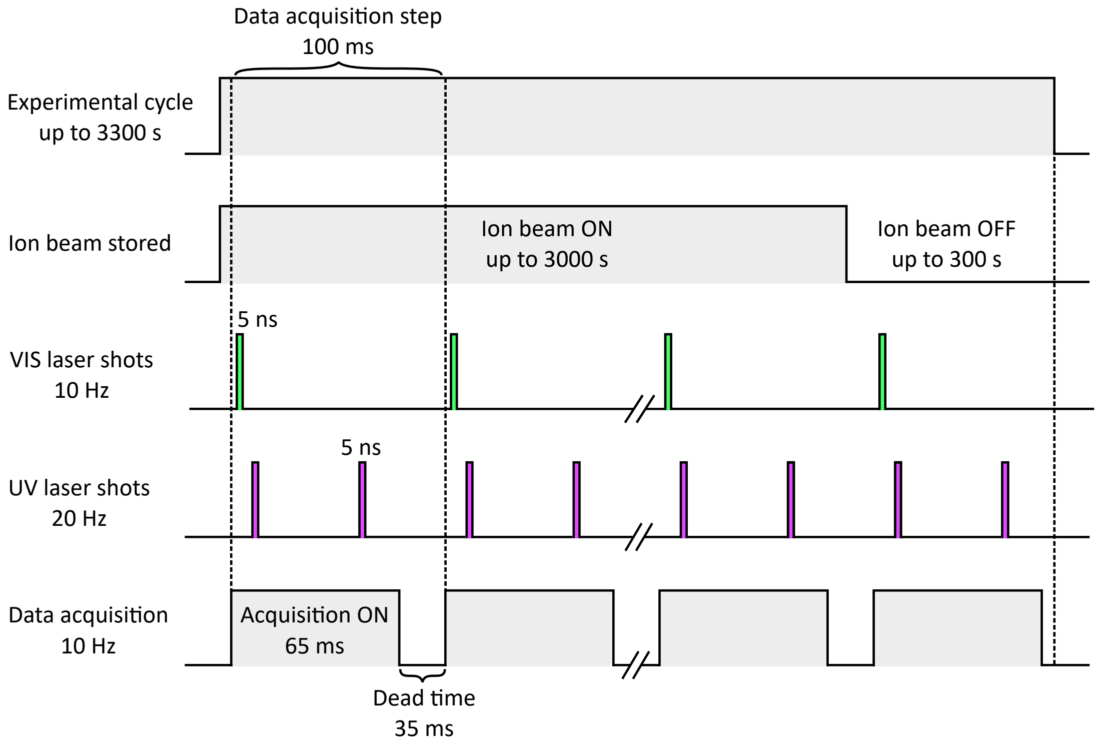

Figure 4.3: The timing scheme used for measuring the ground state H_2CC^- lifetime is shown.

cycle. It is based on LabView and uses an FPGA card[7] for the timings and a dedicated card[8] for digitizing the counting detector signal. The laser control system is also based on LabView software and several counter/timer cards[9]. It provides synchronized trigger signals for firing the pulsed lasers and for reading out the energy meters monitoring the laser pulse energies. Every time a new experimental cycle is started, the laser control system receives feedback from the DAQ system. This ensures that the recorded laser pulse energies are assigned to the correct experimental cycle index. For each laser shot, the laser control system also records the time which has passed since the previous laser shot.

A sketch of the timing scheme is given in figure 4.3. One experimental cycle, which lasts up to 3300 s, is structured as follows: An ion beam is injected into the CSR and stored ("Beam ON" in figure 4.3). After up to 3000 s, the ion beam is dumped ("Beam OFF" in figure 4.3), and the experimental cycle ends after another 300 s. The experimental cycle is subdivided into short DAQ steps, which each have a duration of $t_{\mathrm{DAQ}} = 100$ ms and again a defined time structure: The VIS laser fires at the very beginning of the DAQ step and is followed by two shots of the UV laser. The duration of a laser shot is about 5 ns. The 10 Hz synchronization between the DAQ system and

---

[7] NI PCI-7813R

[8] KeySight U1084A

[9] NI PCIe-6612

the laser control system (see figure 4.2) ensures that the two lasers always fire at the same time with respect to the start of a DAQ step. Within each DAQ step, the DAQ system digitizes the electronic pulses of the detector events. It provides the timing Δt of each digitized detector event with respect to the DAQ step start with ns precision, and its pulse-height U_{pulse}. Additionally the DAQ system provides the time T of the DAQ step start with respect to the time of the ion injection, and hence the precise storage time $t = T + \Delta t$ of each detector event. The DAQ is active in the first 65 ms of each DAQ step ("Acquisition ON" in figure 4.3). The remaining dead time of 35 ms is used for reading out the memory banks of the DAQ system. No detector events are digitized during the dead time.

The detector events originate from residual gas events (continuous), dark counts (continuous), and laser-induced events. Because the lasers are pulsed, these events arrive at the detector in about 2.4 µs with only a small spread of about 20 ns with respect to the time of the laser shot. Within this short time window, the continuous residual gas and dark count events are suppressed by a factor of $\sim 10^6$. Compared to continuous-wave lasers, the pulsed lasers thus offer a great enhancement of the signal-to-noise ratio. The detector dark counts contribute a constant offset to the detector counts and are measured when the ion beam is off.

4.2.3 Modeling the ion beam decay

The H_2CC^- experiment aims at determining the intrinsic lifetime of the ground state H_2CC^- ion by storing an ensemble of H_2CC^- and CN^- ions in the CSR and comparing the decay of both ion species over the course of the storage time. In order to describe their decay and provide a basis for the experiment, we construct a time-dependent a-priori model which accounts for various effects contributing to the decay. It is important to note that this a-priori model can only make assumptions about the circumstances given by the experiment. Later on, the experimental sections 4.3 and 4.4 reveal the actual experimental situation and examine whether the model can still be applied.

So far, we expected to only encounter the desired ion species H_2CC^- and CN^-. In the actual experiment we may also have to account for at least one other contaminant ion species with approximately the same mass-to-charge ratio of 26 u/e. This is motivated by the ion production and separation: In order to produce H_2CC^- and CN^-, the MISS is fed with a mixture C_2H_4 and atmospheric gas. The choice of educts may also lead to the production of other anions, e.g., $^{12}C_2H^-$ and its isotope $^{13}C^{12}CH^-$ with a mass-to-charge ratio of about 26 u/e. As the separating magnets are not capable of resolving and filtering out isobaric ions, all ion species with a mass-to-charge ratio of ≈ 26 u/e are stored in the CSR. Possible contaminants thus have to be included in the model. For simplicity, we assume to have only one contaminant ion species. Experimental results on the actual composition of the stored ion beam are discussed in section 4.3.3.

During the experiment all ion species are stored in the CSR at the same time. While only the vinylidene anion H_2CC^- is expected to have an intrinsic lifetime leading to a decay rate k of the stored H_2CC^- ensemble, all ion beam components are subject to external effects, i.e, decay due to collisions with residual gas, photodetachment by the laser probing and storage-ring induced effects. Here we discuss the properties of these individual effects with respect to the stored ion species.

Generally, after an ensemble of N ions has been stored in the CSR, one can observe that the number of ions decreases at a rate k_{loss} as the time since the ion injection, i.e., the storage time t, progresses. The change $\dot{N} = \mathrm{d}N/\,\mathrm{d}t$ is directly proportional to the loss rate and N:

$$\frac{\mathrm{d}N}{\mathrm{d}t} = -k_{\text{loss}}\, N. \tag{4.1}$$

For the given case of ions trapped in a storage ring, there are usually several effects which add up to the observed loss rate k_{loss} (Jensen, Pedersen, and Andersen 2000, Hahn et al. 2016). For instance, ions can collide with the residual gas left in the experimental vacuum chamber and get neutralized by collisional electron detachment. The corresponding rate k_i^{RG} of the ion species i depends linearly on the collisional electron detachment cross section σ_i^{RG} for the ion impinging on the residual gas particle, the ion velocity v_i and the residual gas density n^{RG}:

$$k_i^{\text{RG}} = \sigma_i^{\text{RG}} v_i n^{\text{RG}}. \tag{4.2}$$

The decay of the ion beam is monitored by means of photodetachment with a VISible laser (VIS) and a UltraViolet laser (UV). The monitoring process itself then reduces the ion ensemble at the rates $k^{\text{VIS/UV}}$. These rates are linearly proportional to the photodetachment cross sections $\sigma^{\text{VIS/UV}}$ of the respective ion. They are also linearly dependent on the rates $r^{\text{VIS}} = 10$ Hz and $r^{\text{UV}} = 20$ Hz at which the pulsed lasers fire, and on the luminosity $L^{\text{VIS/UV}}$ of the lasers. The luminosity factor (see equation 4.20) contains geometrical factors and the number of photons in the ion-photon interaction region. The individual photodetachment loss rates then read:

$$k_i^{\text{VIS}} = \sigma_i^{\text{VIS}} r^{\text{VIS}} L^{\text{VIS}} \tag{4.3}$$

$$k_i^{\text{UV}} = \sigma_i^{\text{UV}} r^{\text{UV}} L^{\text{UV}}. \tag{4.4}$$

The photodetachment cross sections at the respective laser photon energies are given in table 4.1. Note that, as this table also contains information about the measured ion beam composition, it is shown later in the context of the isobaric mass analysis in section 4.3.3.2. The photodetachment cross section is > 0 if the photon energy of the VIS laser (2.33 eV) or the UV laser (4.00 eV) lies above the detachment threshold (EA) of the stored ion. Based on the EAs (also given in table 4.1) we assume that the VIS laser detaches only H_2CC^- and that the UV photons have a high enough photon energy to detach all ion species.

Lastly, we ascribe a loss rate k_0 to the entirety of all effects induced by the storage ring itself. These effects can not be measured directly and the dependencies on properties of the storage ring are not known in detail. One example for such an effect is the voltage rippling of the ion optical elements. Even though the voltages are stable on the order of $\sim 10^{-5}$, the effect may cause ions to deviate from a stable orbit and eventually get lost by collision with a vacuum chamber wall. A second example would be the finite precision at which the ion optical elements were machined and mechanically aligned to each other. This may lead to imperfections in the ion optical lattice and again to a loss of ions over many revolutions. Furthermore, it is not known, whether these effects depend on properties of the stored ions, such as their mass-to-charge ratio or their kinetic energy per elementary charge. Given the small difference ($< 5 \times 10^{-4}$) of the mass-to-charge ratio of all the 26 u/e species we assume that this type of losses is identical for all ion beam components and manifests in the loss rate k_0.

With the mentioned rates and variables from equations 4.2–4.4, we model the temporal change $\dot{N}_i = \mathrm{d}N_i/\,\mathrm{d}t$ in the ion number of the individual species i in the ion beam as a set of uncoupled linear differential equations of first order. The indices represent H_2CC^-(1), CN^-(2) and one contaminant ion species (3):

$$-\frac{\dot{N}_1}{N_1} = k_0 + k_1^{\mathrm{RG}} + k_1^{\mathrm{UV}} + k_1^{\mathrm{VIS}} + k \tag{4.5}$$

$$-\frac{\dot{N}_2}{N_2} = k_0 + k_2^{\mathrm{RG}} + k_2^{\mathrm{UV}} \tag{4.6}$$

$$-\frac{\dot{N}_3}{N_3} = k_0 + k_3^{\mathrm{RG}} + k_3^{\mathrm{UV}} \tag{4.7}$$

Integration of equation 4.5–4.7 over the storage time t yields:

$$N_1(t) = N_1^0 e^{-(k_0+k_1^{\mathrm{RG}}+k_1^{\mathrm{UV}}+k_1^{\mathrm{VIS}}+k)t} \tag{4.8}$$

$$N_2(t) = N_2^0 e^{-(k_0+k_2^{\mathrm{RG}}+k_2^{\mathrm{UV}})t} \tag{4.9}$$

$$N_3(t) = N_3^0 e^{-(k_0+k_3^{\mathrm{RG}}+k_3^{\mathrm{UV}})t} \tag{4.10}$$

Here, the prefactors N_i^0 represent the initial number of ions. In summary, the result of the model is that the ion beam components decay exponentially as a function of the storage time t. All beam components are affected by loss rates due to storage-ring induced effects, collisions with residual gas particles and depletion by the UV laser. Additionally, the H_2CC^- ion ensemble is diminished by VIS laser depletion and the loss rate k ascribed to the intrinsic lifetime of the ground state H_2CC^-. By comparing the decays and quantifying the residual gas and laser-induced loss rates, one can cancel k_0 and in principle obtain the loss rate k.

4.2.4 Expected photodetachment signal

After having developed the model for the decay of the individual ion species in section 4.2.3, we now discuss how the model can be connected to the photodetachment

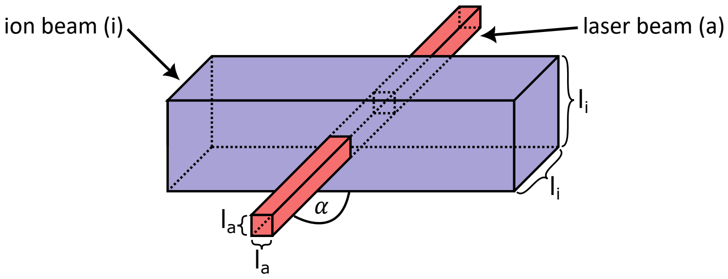

Figure 4.4: Simplified model: A laser beam (a) with quadratic profile overlaps with an ion beam (i) with quadratic profile at an angle of $\alpha = 90°$.

experiment and which measured quantities are relevant for observing the modeled exponential decay. The decay of the stored ion ensemble can be monitored by overlapping the ion beam with a laser beam and photodetaching a small fraction of the ions. The overlap of the two beams is illustrated with a simple geometric model (see figure 4.4) with quadratic beam profiles. The region in which ions and photons interact is then a cuboidal volume V. Within the interaction volume V, the number of neutralized ions N_{neut} is determined by the photodetachment cross section σ, the ion density n_{ion}, the duration t_{pulse} of the laser pulse and the photon flux density ϕ:

$$N_{\text{neut}} = \sigma\ \phi\ n_{\text{ion}}\ t_{\text{pulse}}\ V \tag{4.11}$$

The ion density is derived from the number of ions N_i, the ion beam profile area $A_i = l_i^2$, and the closed-orbit circumference C_{CSR} of the storage ring. For the case of a pulsed laser, the photon flux density ϕ is determined by the number of photons N_γ per laser pulse, the laser pulse duration t_{pulse} and the laser beam profile area $A_a = l_a^2$. The number of neutralized particles is then expressed as follows:

$$\begin{aligned} N_{\text{neut}} &= \sigma \frac{N_\gamma N_i}{A_a A_i t_{\text{pulse}} C_{\text{CSR}}} t_{\text{pulse}} V && (4.12) \\ &= \sigma \frac{N_\gamma N_i}{A_a A_i C_{\text{CSR}}} V && (4.13) \end{aligned}$$

Here we assume that the laser pulse duration is short compared to the time it takes an ion to pass the ion-photon interaction region, i.e., the ions do not move while the laser pulse passes by. We also assume that the ions addressed by the laser pulse are not bleached: The laser pulse can in principle remove all ions in the overlap volume. Increasing the photon density then does not further increase the number of neutralized particles.

From the interaction region, the neutralized particles fly ballistically towards the counting detector (see figure 4.1). The fraction η of these neutrals with the correct direction of momentum for impinging on the surface of the counting detector is detected with an efficiency $\epsilon = 0.593 \pm 0.015$ (given by the MCP single-particle counting efficiency in Paul et al. 2022):

$$\tilde{N} = \eta\epsilon N_{\text{neut}} \tag{4.14}$$

$$= \eta\epsilon\sigma\frac{N_\gamma N_i}{A_a A_i C_{\text{CSR}}}V \tag{4.15}$$

In the direction of the laser beam, the volume V of the interaction region is horizontally restricted by the ion beam width l_i. The laser beam width l_a restricts V in the direction of the ion beam. Depending on whether the laser beam or the ion beam is smaller, V is vertically restricted either by l_a or l_i:

$$V = l_a l_i \min(l_a, l_i) \tag{4.16}$$

Together with $A_i = l_i^2$ and $A_a = l_a^2$, we obtain for the measured number of particles (equation 4.15):

$$\tilde{N} = \eta\epsilon\sigma\frac{N_\gamma N_i}{l_a^2 l_i^2 C_{\text{CSR}}} l_a l_i \min(l_a, l_i) \tag{4.17}$$

$$= \eta\epsilon\sigma\frac{N_\gamma N_i}{\max(l_a, l_i) C_{\text{CSR}}} \tag{4.18}$$

$$= \eta\epsilon\sigma\frac{N_\gamma N_i}{l_{\max} C_{\text{CSR}}} \tag{4.19}$$

Here, we abbreviated the beam height of either the laser beam or the ion beam with the maximum beam height $l_{\max} = \max(l_a, l_i)$. Note that the luminosity

$$L = \frac{N_\gamma}{l_{\max} C_{\text{CSR}}} \tag{4.20}$$

$$= \frac{E_{\text{pulse}}}{l_{\max} C_{\text{CSR}} E_\gamma} \tag{4.21}$$

of the laser is determined by the geometric factors and the number of photons N_γ. In order to estimate $N_\gamma = E_{\text{pulse}}/E_\gamma$, the laser pulse energy E_{pulse} has to be measured and the photon energy E_γ has to be known. The measured number of particles $\tilde{N}$ then transforms to:

$$\tilde{N} = \eta\epsilon\sigma\frac{N_i}{l_{\max} C_{\text{CSR}}}\frac{E_{\text{pulse}}}{E_\gamma}. \tag{4.22}$$

In the context of the H_2CC^-lifetime measurement, we do not change the photon energy E_γ. We assume that the chosen photon energies of 2.33 eV and 4.00 eV are so far away from the detachment threshold (EA) that the photodetachment cross section σ is independent of the internal state of the anionic molecules, and hence constant for constant E_γ. For H_2CC^- (EA$\approx$ 0.49 eV) this is likely the case (see section 1.2). In analogy with the experiment by Meyer et al. 2017 we assume that this is also the case for CN^-, for which the photon energy lies only ≈ 0.14 eV higher than the detachment

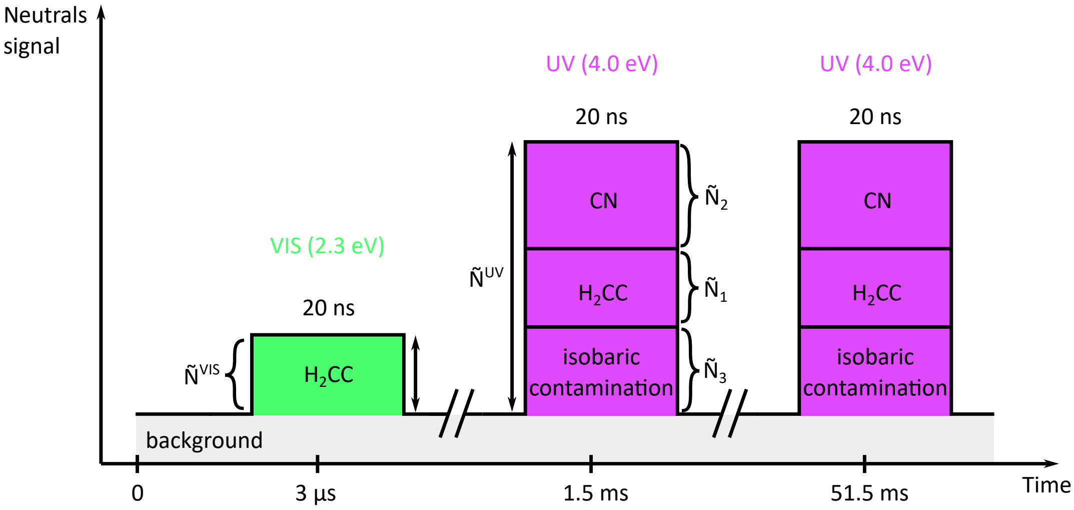

Figure 4.5: Scheme for one DAQ step: The neutrals signal at the NICE detector is sketched as function of the time during the DAQ step.

threshold EA≈ 3.86 eV. We presume η, ϵ and the geometric factors to be constant, while N_i (ion beam decay) and E_{pulse} (laser intensity fluctuation) are time dependent. By monitoring the laser yield Y, i.e., the number of measured particles $\tilde{N}$ normalized by the laser pulse energy E_{pulse}, one can monitor the temporal change of N_i:

$$Y(t) = \frac{\tilde{N}(t)}{E_{\text{pulse}}(t)} \tag{4.23}$$

$$= \frac{\eta\epsilon\sigma}{l_{\max}C_{\text{CSR}}}\frac{1}{E_\gamma}N_i(t) \tag{4.24}$$

Now that the relation between the directly measured quantities and the actual number of ions in the ring is established, we can construct the expected photodetachment signal. In accordance with the timing scheme outlined in section 4.2.2 and figure 4.3, the expected neutrals signal at the counting detector is sketched in figure 4.5. During each measurement step the VIS laser fires once with a laser pulse energy E^{VIS} and as a result the number of neutrals $\tilde{N}^{\text{VIS}}$ is detected within a short time window of about 20 ns. For reasons discussed in section 4.2.3, we assume that only $H_2CC^-$is detached. With equations 4.8, 4.23 and 4.24 the VIS laser yield $Y^{\text{VIS}}(t)$ is then:

$$Y^{\text{VIS}}(t) = \frac{\tilde{N}^{\text{VIS}}(t)}{E^{\text{VIS}}(t)} \tag{4.25}$$

$$= \underbrace{\frac{\eta\epsilon\sigma_1^{\text{VIS}}}{l_{\max}C_{\text{CSR}}E_\gamma^{\text{VIS}}}}_{C_1^{\text{VIS}}} N_1(t) \tag{4.26}$$

$$= C_1^{\text{VIS}}N_1^0 e^{-(k_0+k_1^{\text{RG}}+k_1^{\text{UV}}+k_1^{\text{VIS}}+k)t} \tag{4.27}$$

The effective decay rate

$$k_1^{\mathrm{eff}} = k_0 + k_1^{\mathrm{RG}} + k_1^{\mathrm{UV}} + k_1^{\mathrm{VIS}} + k \tag{4.28}$$

measured with the VIS laser is thus a sum of the decay rates due to external effects and the decay rate k related to the intrinsic lifetime of the H_2CC^- ion. Since all rates are positive, the measured rate k_1^{eff} marks an upper limit for k.

Twice per measurement step, the UV laser detaches anions with a laser pulse energy E^{UV}, and neutrals $\tilde{N}^{\mathrm{UV}}$ are detected. As discussed in section 4.2.3, we assume that the UV photon energy is high enough to photodetach all components in the ion beam, in particular also the isobaric contamination. With equations 4.8–4.10 describing the decay of the beam components and the definition of the laser yield in equations 4.23 and 4.24, the UV laser yield $Y^{\mathrm{UV}}(t)$ can be constructed:

$$\begin{aligned}
Y_{\mathrm{UV}}(t) &= \frac{\tilde{N}^{\mathrm{UV}}(t)}{E^{\mathrm{UV}}(t)} && (4.29)\\
&= \frac{\sum_i \tilde{N}_i}{E^{\mathrm{UV}}(t)} && (4.30)\\
&= \sum_i \underbrace{\frac{\eta\epsilon\sigma_i^{\mathrm{UV}}}{l_{\max} C_{\mathrm{CSR}} E_\gamma^{\mathrm{UV}}}}_{C_i^{\mathrm{UV}}} N_i(t) && (4.31)\\
&= C_1^{\mathrm{UV}} N_1^0 e^{-(k_0 + k_1^{\mathrm{RG}} + k_1^{\mathrm{UV}} + k_1^{\mathrm{VIS}} + k)t} && (4.32)\\
&\quad + C_2^{\mathrm{UV}} N_2^0 e^{-(k_0 + k_2^{\mathrm{RG}} + k_2^{\mathrm{UV}})t} && (4.33)\\
&\quad + C_3^{\mathrm{UV}} N_3^0 e^{-(k_0 + k_3^{\mathrm{RG}} + k_3^{\mathrm{UV}})t} && (4.34)
\end{aligned}$$

Three different components thus contribute to the UV laser yield. Based on the photodetachment cross sections of the anions with mass $m \approx 26$ u in table 4.1 (section 4.3.3.2) we assume that σ_i^{UV} and hence the prefactors C_i^{UV} of the beam components (see equation 4.31) do not differ significantly. Furthermore we presume the reference ion CN^- to be by far the most abundant component in the ion beam. In this case we obtain $C_2^{\mathrm{UV}} N_2^0 \gg C_i^{\mathrm{UV}} N_i^0$ for $i \in \{1, 3\}$ for the prefactors in equations 4.32–4.34, and the UV laser yield simplifies to:

$$Y_{\mathrm{UV}}(t) \approx C_2^{\mathrm{UV}} N_2^0 e^{-(k_0 + k_2^{\mathrm{RG}} + k_2^{\mathrm{UV}})t} \tag{4.35}$$

Whether this ideal situation can still be assumed in the actual H_2CC^- lifetime experiment is discussed in detail based on the experimental results in section 4.3.3.

In order to cancel the rate due to the storage-ring induced effects k_0, the VIS laser yield (equation 4.27) is divided by the UV laser yield (equation 4.35). The yield ratio

$Y_{\text{UV}}^{\text{VIS}}$ then takes approximately the form

$$\begin{aligned}
Y_{\text{UV}}^{\text{VIS}}(t) &= \frac{Y^{\text{VIS}}(t)}{Y_{\text{UV}}(t)} && (4.36)\\
&= \frac{\tilde{N}_{\text{VIS}}(t)E^{\text{UV}}(t)}{\tilde{N}_{\text{UV}}(t)E^{\text{VIS}}(t)} && (4.37)\\
&\approx \underbrace{\frac{C_1^{\text{VIS}}N_1^0}{C_2^{\text{UV}}N_2^0}}_{\tilde{C}} \frac{e^{-(k_0+k_1^{\text{RG}}+k_1^{\text{UV}}+k_1^{\text{VIS}}+k)t}}{e^{-(k_0+k_2^{\text{RG}}+k_2^{\text{UV}})t}} && (4.38)\\
&= \tilde{C}e^{-(k_1^{\text{RG}}-k_2^{\text{RG}}+k_1^{\text{UV}}-k_2^{\text{UV}}+k_1^{\text{VIS}}+k)t} && (4.39)\\
&= \tilde{C}e^{-k^{\text{eff}}t}, && (4.40)
\end{aligned}$$

which is but a single exponential function. With the initial number of ions N_i^0 being constant and given that the photodetachment cross sections are constant for constant photon energy (see context of equation 4.22), the prefactor $\tilde{C}$ is constant over the course of the storage time t. The effective rate

$$k^{\text{eff}} = (k_1^{\text{RG}} - k_2^{\text{RG}}) + (k_1^{\text{UV}} - k_2^{\text{UV}}) + k_1^{\text{VIS}} + k \tag{4.41}$$

can then be extracted. Here, it may not only contain positive terms in case of the decay rates due to the collisional electron detachment and the photodetachment by the UV laser. However, only differences of these rates between the two ion species enter.

By measuring the number of VIS and UV photodetachment products $\tilde{N}_{\text{VIS}}(t)$ and $\tilde{N}_{\text{UV}}(t)$, and the energies of the photodetachment lasers $E^{\text{VIS}}(t)$ and $E^{\text{UV}}(t)$ simultaneously and as a function of the storage time t, we obtain the effective decay rate k^{eff}. This rate, in turn, contains the decay rate k attributed to the intrinsic lifetime of the ground state H_2CC^- ion. Further discussion on how to distinguish k from the other rates in equation 4.41 will be made in section 4.4.

4.3 Experiment procedure and data analysis

The previous section 4.2 introduced the idea of the H_2CC^- lifetime experiment in detail. We described the experimental setup (sections 4.2.1–4.2.2) and constructed a model allowing us to connected the decay of H_2CC^- and the stable reference ion CN^- to parameters measured during the photodetachment experiment (sections 4.2.3–4.2.4).

Here, we now turn to the measured data and determine if our model is still applicable. We analyze the overall time structure of the counting detector signal, identify the relevant signals and separate them from the background (section 4.3.1). Section 4.3.2

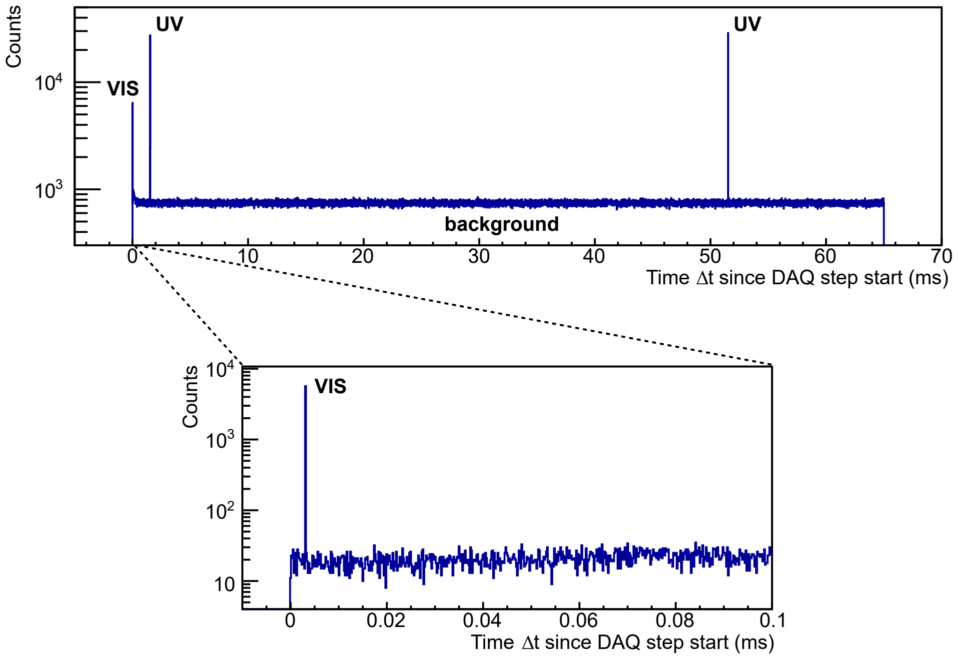

Figure 4.6: The accumulated detection events of a DAQ step are presented: The NICE detector counts are plotted against the delay Δt after the start of the DAQ step. The lower panel is a zoom around the VIS-induced peak. The displayed events are the sum of about 7×10^5 individual DAQ steps.

describes how to suppress detector noise, which is also part of the background signal, by means of pulse-height cuts. Since our decay model also makes assumptions about contaminations of the stored ion ensembles with ions other than H_2CC^- and CN^-, we analyze their composition in detail (section 4.3.3). Note that appendix B.2 outlines how the data of the H_2CC^- lifetime experiment is processed and how the decay curves of the laser signals are constructed.

4.3.1 Laser and collisional background events

The NICE detection events originate from various sources, such as laser-induced photodetachment, residual-gas collision-induced detachment, and electronic noise. Here we will discuss the time-structure of the acquired signal, how it helps to improve the signal-to-background ratio, and how it is used to monitor signals from the various sources as a function of ion storage time.

The Data AcQuisition (DAQ) system acquires waveforms of the detector anode signal. In each DAQ step (see section 4.2.2) the acquired waveform is analyzed and each pulse is identified as a detection event, with assigned pulse-height U_{pulse} and a delay Δt with respect to the beginning of the acquisition step. Detected events from various acquisition steps can be accumulated as a function of Δt, as shown in figure 4.6.

The events in figure 4.6 are accumulated from about 7×10^5 individual DAQ steps from a data set with typical experimental settings, independently of the time of a DAQ since the ion injection, i.e., the storage time T. For reasons explained in section 4.2.2, only the first 65 ms of a 100 ms DAQ step are recorded.

The accumulated detection events feature a uniformly distributed signal (background) and three distinct peaks. The first peak (VIS) appears at the very beginning of the accumulated detection events, while the second and third peak (UV) appear at about 2 ms and 52 ms. In agreement with the timing scheme (figure 4.3) and the repetition rates at which the lasers fire, the peaks can be associated with the 10 Hz VIS and the 20 Hz UV laser.

The background originates from random detector noise (dark counts) and a continuous influx of neutralized particles from the ion beam. The detector dark counts occur as random detection events over time and contribute as a constant offset to the background. The origin of the neutralized particles lies in the linear section before the NICE detector. A small fraction of the stored anions collides with residual gas particles, gets neutralized and flies ballistically towards the NICE detector. As the stored ions continuously circulate in the CSR, the contribution to the background is also continuous. Within the short time scale of the DAQ step it appears to be flat, event though in reality it decays in time as the number of ions in the ring decays.

Figure 4.7 a) and 4.7 b) examine the VIS peak and the first UV peak more closely. Each of the two panels shows a ~ 4 µs time interval sampled with a bin width of about 6 ns. In the case of the VIS peak, a single peak appears at about 3 µs with respect to the start of a DAQ step, i.e., 2.4 µs after the VIS laser fired. It is a plateau with a width of ~ 100 ns. In figure 4.7 b), the UV peak splits up into two separate peaks. The second peak is an order of magnitude higher than the first peak and appears about 2.4 µs after the first peak.

The peaks in figure 4.7 b) are explained by UV photons and the neutrals from photodetachment: A small fraction of the UV photons in the ion-photon interaction region is reflected at the chamber walls and impinges on the NICE detector. The 4 eV photons have a high enough energy to be registered as counts at the detector and form the first peak. It was checked that the number of detected UV photons was low and the MCP-based detector was not depleted, i.e., particles impinging soon after the laser pulse were detected with unchanged efficiency. The second peak originates from the neutrals from photodetachment with UV photons in the interaction region. From the interaction region, the neutrals cover a 3.3 m distance before they are counted at the NICE detector. For a kinetic energy of 250 keV of the neutrals, the distance corresponds to a time-of-flight of about 2.4 µs, which agrees with the time lag between the peaks. We forgo discussing the second UV peak in figure 4.6, since it bears similar observations.

The single VIS peak in figure 4.7 a) is explained by the fact that the 2.33 eV photons

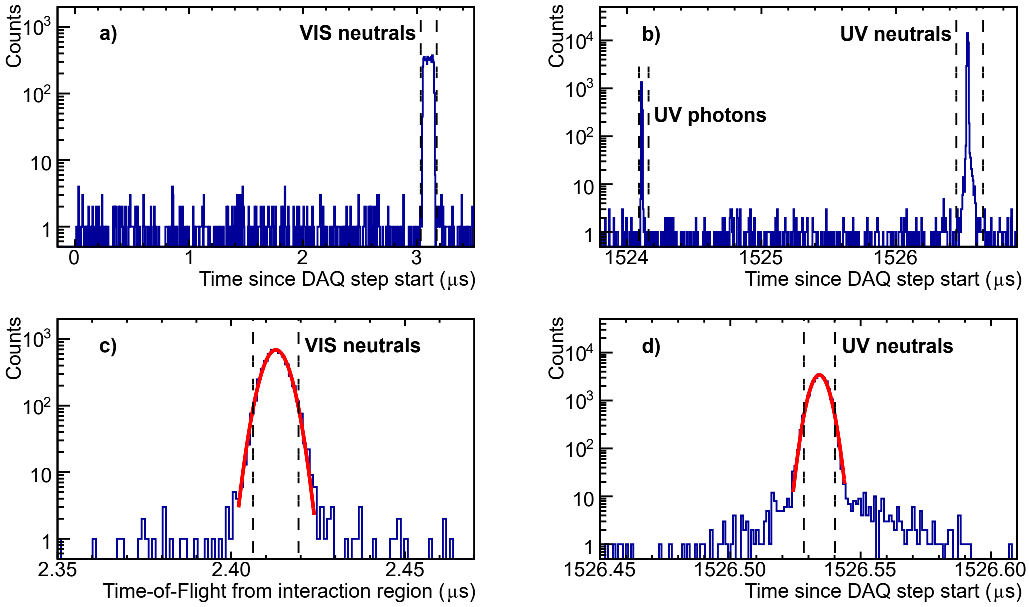

Figure 4.7: The VIS peak and the first UV peak of the accumulated detection events from figure 4.6 are inspected more closely: Panel a) and b) zoom in on the features of the VIS and UV peak. Panel c) and d) zoom in further and inspect the peak shape of the UV and VIS neutrals peak. Drawn in red are Gaussian fits to the peaks. The vertical dashed lines define time windows relevant for the later analysis. Note that for panel c) the events are plotted as a function of the time-of-flight from the interaction region to the detector. For a more detailed explanation, see the text.

of the VIS laser do not have sufficient energy for launching an electron avalanche at the NICE detector and being detected. The peak is thus attributed to neutrals resulting from VIS photodetachment in the interaction region.

Now that the neutral events resulting from photodetachment by the VIS and UV laser are identified in the accumulated detection events, we can in principle monitor different ion beam components by watching the number of events occurring within certain time windows. Because the laser-induced counts originate only from narrow ranges of $t_{\text{laser}} \leq 200$ ns, one can apply time filters. Within the narrow time windows (shown as dashed lines in figure 4.7) the laser-induced signal dominates over the background, even though in the non-filtered signal the background is dominant. Given the duration of a DAQ step of $t_{\text{DAQ}} = 100$ ms and the fact that the UV laser shoots twice per DAQ step, the background contribution within the narrow time windows is suppressed by a scaling factor $w_1 = t_{\text{DAQ}}/t_{\text{laser}} \geq 2.5 \times 10^4$, and can be neglected in first order. By only looking at the counts outside of all time windows, in turn, the background can be monitored.

What remains to be investigated are the shapes of the VIS and UV neutrals peak, which differ significantly. The UV peaks are much sharper than the VIS peak. Related to the peak shape is the question if one can set the window borders around the neutral laser events narrower, in order to suppress the background within the windows even further. With figures 4.7 c) and d), we address these questions.

Figure 4.7 d) zooms in further to a time interval of 150 ns containing the UV neutrals peak. The peak appears to have a Gaussian distribution in first order. A Gaussian fit (red line) yields a width of $4\sigma_{\text{UV}} \approx 12.0$ ns, which is indicated by the vertical dashed lines. This value is comparable to the duration of the UV photon pulse (5 ns). Given the fact that the laser pulses have the shape of a Gaussian distribution in time, the Gaussian distribution of the laser-induced detector events is plausible.

During the course of the experiment the timing of the VIS laser pulses was observed to jitter significantly by about ±50 ns with respect to the laser trigger. The broad peak shape of the VIS neutrals peak in figure 4.7 a) may be explained by this observation. In order correct for the laser jittering, we acquire the actual time of the laser shot by means of a photodiode and correlate it to the arrival time of the VIS neutrals at the NICE detector. The time difference between the photodiode signal and the corresponding NICE detector signal is then the ToF from the interaction region to the NICE detector.

In figure 4.7 c) the NICE detector counts of the VIS are plotted against the ToF from the interaction region (time between the detected event and the laser shot time from the photodiode signal). An interval of 120 ns containing the VIS neutrals peak is displayed. The peak is fitted with a Gaussian (red line). The mean value of the fitted Gaussian is about 2.41 µs and matches the expected ToF. The fitted Gaussian has a width of $4\sigma_{\text{VIS}} \approx 13.0$ ns. As observed for the UV laser events, this value is also on the order of the VIS laser pulse duration (5 ns).

For the further analysis of the decay of the beam components, we define the borders of the VIS and UV neutral event windows: All events occurring within a $\pm 2\sigma$ interval around the maximum of the fitted Gaussians are identified as neutrals resulting from photodetachment. With this choice, about 95 % of the events in each peak are covered. The background within the windows is now suppressed by a factor of $w_2 = t_{\text{DAQ}}/(8\sigma_{\text{UV}}) > 4 \times 10^6$ (two UV laser windows per DAQ step). This is more than two orders of magnitude more than for the broader event windows from figures 4.7 a) and b).

In summary, the relevant data were analyzed as function of the time Δt since the DAQ step start. We identified the neutral events due to the VIS and UV laser. The Gaussian-like distribution of these events helps us to systematically define narrow time windows around them and thereby suppress the background originating from detector noise and neutrals due to collisional electron detachment.

As the DAQ system does not only provide Δt, but also the time T of each DAQ step with respect to the time of the ion injection (see section 4.2.2), the precise storage time $t = T + \Delta t$ can be reconstructed for each event. This allows us to analyze the decay of the different beam components as a function of t independently of the background.

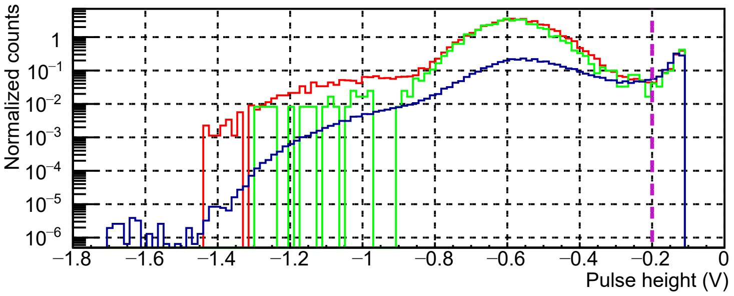

Figure 4.8: Pulse-height distributions of the NICE detector events: The plot distinguishes between the VIS neutrals (green), the UV neutrals (red), and the neutral events due to collisional electron detachment (blue). The vertical dashed line (purple) indicates the chosen border for the pulse-height cuts. The distributions are normalized to the respective integral of all counts to the right of this border.

4.3.2 Pulse-height distributions of the NICE detector events

The NICE detector is based on an MCP detector (Becker 2016) and essentially converts impinging fast particles into nanosecond electronic pulses with a height U_{pulse}. The detector signal also contains noise in the form of electronic pulses with similar duration, but lower height. External conditions can cause the noise to fluctuate over time, which may complicate the identification of signals due to impinging particles. For the analysis, it is thus desirable to discriminate the detector noise against actual particle signals as well as possible. In order to do so, the pulse-height distribution of the detector signal has to be analyzed. In the following the pulse-height distribution of a typical experimental run of the H_2CC^-stability experiment will be discussed.

The pulse-height distributions of the detector signal are displayed in figure 4.8. The normalized counts are plotted against the heights of the corresponding negative electronic pulses. The plot features the pulse-height distributions of the VIS neutrals (green), the UV neutrals (red), and neutral events resulting from collisional electron detachment (blue).

All three distributions have a similar structure. A broad distribution of counts is centered around $U_{\mathrm{pulse}} = -0.6$ V. Towards higher pulse-heights ($U_{\mathrm{pulse}} < -0.9$ V) the distributions open out into a shoulder, which are 1.5–2.5 orders of magnitude lower than the distribution maximum. Additionally, the blue histogram has a small tail at $U_{\mathrm{pulse}} \approx -1.7$ V. Towards lower pulse-heights ($U_{\mathrm{pulse}} > -0.2$ V), the number of counts increases again.

The tail with low pulse-heights results from detector noise. Most counts with higher pulse-heights can be attributed to fast particles impinging on the detector. In order to discriminate against the noise, we discard all counts with $U_{\mathrm{pulse}} \geq -0.2$ V (vertical purple dashed line).

By setting a limit at low pulse-heights, we are thus able to select the electronic

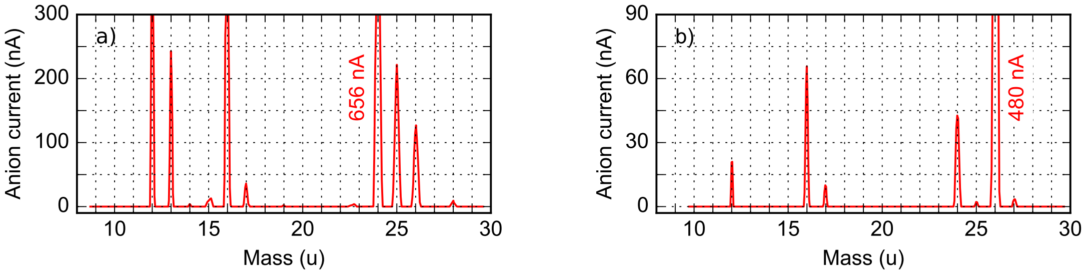

Figure 4.9: Magnetic mass spectra of 20 keV ion beams produced with a MISS under different conditions. The anion current after the selecting magnet is plotted against the mass (assuming singly charged ions). In a) the ion source is fed with a mixture of C_2H_4 and atmospheric gas. The sputtering target is Ta. The peaks at 12 u, 16 u and 24 u are saturated. For the latter, the measured peak value is given. In b) the output of a freshly cleaned MISS without gas input and a CuCN/Ag target is analyzed. The measured value for the peak at 26 u is stated.

detector pulses resulting from fast particles. The pulse-height cuts work equally well for the laser-induced neutrals and the neutrals due to collisional electron detachment and can be incorporated into the further analysis.

4.3.3 Ion beam composition and photodetachment signals

The idea of the H_2CC^- lifetime experiment (see section 4.2.3 and 4.2.4) is to store a mixed beam of H_2CC^- and CN^- ions in the CSR and to monitor their decay simultaneously and independently with photodetachment. While we expect H_2CC^- to have an intrinsic lifetime (Jensen, Pedersen, and Andersen 2000), CN^- serves as a stable reference ion. Ideally, comparing the decay of both ion species suppresses external effects which affect the decay of both species in a similar manner and brings out information about the intrinsic H_2CC^- lifetime.

For the experiment we aim at producing both H_2CC^- and CN^- with the same ion source. As we want to address both ion species independently with our two photodetachment lasers (equations 4.27 and 4.35 in section 4.2.4), it would be preferable to have only a small fraction of H_2CC^-. Apart from the desired ions, the ion source may also produce other contaminant ion species possibly contributing to the photodetachment signals. For these reasons we carefully analyze the ion beam composition and discuss the relevance of the contaminants for the photodetachment signals. Furthermore, we experimentally check if the laser intended for monitoring H_2CC^- actually photodetaches only this ion or also other components of the stored ion beam. Prior to the isobaric mass analysis (section 4.3.3.2) we discuss the ion production (section 4.3.3.1).

4.3.3.1 Ion source

For producing the mixed H_2CC^-/CN^- ion beam, we employ a Middleton-type Metal Ion Sputter Source (MISS) (Middleton 1983). It is a surface plasma ion source, which produces anions from a solid cathode by sputtering it with cesium (Cs) cations, followed by negative ionization at the cathode surface. In addition, the cathode surface is covered with a thin layer of Cs, which reduces the surface work function and greatly enhances the anion yield (Bacal, Sasao, and Wada 2021). The MISS is also capable of producing anions from gaseous educts let into the source volume if it is equipped with a chemically active cathode, such as, among other materials, tantalum (Ta) or titanium (Middleton, Klein, and Fink 1989). In our case, we equip the MISS with a Ta cathode and feed it with a 2–5 mbar mixture of C_2H_4 and a small fraction of atmospheric gas[10].

As the gases are supposed to be the educts for H_2CC^- and CN^-, we refer to this MISS configuration as H_2CC^-/CN^- source configuration. The choice of educts may also result in other contaminant ions with a mass of 26 u. In order to analyze the ion output of the MISS, we record magnetic mass spectra using the magnet on the 300 kV ion source platform and the subsequent Faraday cup (see figure 3.6 a). The resulting magnetic mass spectrum is shown in figure 4.9 a). The peak at 26 u is accompanied by two large peaks which may mostly result from C_2^- (24 u) and C_2H^- (25 u). Based on the peak heights and the isotopic abundances of D ($\approx 1.6 \times 10^{-4}$) and ^{13}C (≈ 1.1 %) taken from Meija et al. 2016, the 127 nA peak at 26 u likely contains small relative fractions of $^{12}C_2D^-$ ($\approx 3 \times 10^{-4}$), $^{13}C_2^-$ ($\approx 6 \times 10^{-4}$), and a larger fraction of $^{13}C^{12}CH^-$ (≈ 1.9 %).

For comparison, we switch to a source configuration unable to produce H_2CC^-. To this end, we clean the source and operate it without gas, but with a CuCN/Ag sputtering cathode. Figure 4.9 b) shows the corresponding magnetic mass spectrum. As the large peak at 26 u indicates efficient production of CN^-, we refer to this MISS configuration as CN^- source configuration. The peaks at 24 u and 25 u may mostly result from isotopes of C_2^-. The low peak at 25 u suggests that the corresponding peak in figure 4.9 a) is related to the inlet of C_2H_4 gas, and thus likely results from $^{12}C_2H^-$. This supports the hypothesis on the contamination of the 26 u peak with $^{13}C^{12}CH^-$.

At this point, it is worthwhile to mention our unsuccessful and quite extensive attempts to produce H_2CC^-. We tried to produce H_2CC^- with a similar MISS configuration as Jensen, Pedersen, and Andersen 2000 used for their room-temperature H_2CC^- lifetime experiment. They used a Fe_3O_4 cathode for the production of O^- and let C_2H_4 gas into the source in order to create H_2CC^- in the presumed chemical reaction

$$C_2H_4 + O^- \longrightarrow H_2CC^- + H_2O. \tag{4.42}$$

In our case we used Fe_2O_3 instead of Fe_3O_4. Even though in the magnetic mass spectra we saw a strong peak at the mass of O^- (≈ 6 µA) and indications that C_2H_4

---

[10] Approximate composition (Cox 2002): 78 % N_2, 21 % O_2, 1 % other including water vapor

was successfully being fed into the source, the ion output at mass 26 turned out to be rather low (< 10 nA). Additionally, from analysis of the charged fragments of the mass 26 ion beam[11], we found that the beam likely only contained CN^- and no H_2CC^-. On the one hand, this observation may indicate that the reaction dynamics are different compared to a Fe_3O_4 sputtering target. On the other hand, Seiersen 2003 (pp. 34–36) also reported this observation from charged-fragment analysis for the same ion source type and configuration as used by Jensen, Pedersen, and Andersen 2000, including the Fe_3O_4 sputtering target. Apparently, the source is capable of producing H_2CC^-, but for the same ion source configuration one may also end up in a situation with only CN^-. In their experiment, Jensen, Pedersen, and Andersen 2000 carefully checked their ion source output beforehand. Apart from the MISS, we also attempted to produce H_2CC^- using a hollow cathode ion source, where we let in O_2 and C_2H_4. Here, the mass 26 output was also rather low (<15 nA) and additionally so unstable that we considered it ineligible for our experiment. Details on this ion source can be found in Altevogt 2003.

4.3.3.2 Isobaric mass analysis

While the magnetic mass spectra already give an idea about the possible contaminations, they do not answer the question on the relative fractions of H_2CC^- and CN^-. Also, they do not give information if there are more contaminants with a mass of 26 u than the suspected ones. To address these questions, we analyze the composition of the mass 26 u peak from figure 4.9 with a direct and much more precise method. For this, we store the ions in the CSR and apply the novel isochronous mass spectrometry technique outlined in section 3.2.4 and detailed in Grieser et al. 2022. With a mass resolution of $\Delta m/m < 10^{-5}$ it is capable of resolving all isobars with mass 26 u.

The isochronous Time-of-Flight (ToF) spectra are displayed in figure 4.10. The left column is dedicated to the H_2CC^-/CN^- ion source configuration, while the right column is associated with the CN^-source configuration. In the spectrum in figure 4.10 a) the counts in the halo of the stored ion beam registered at the COMPACT detector are binned into a two-dimensional histogram. As explained in section 3.2.4, the lines in the acquired signal pattern of the ToF mass spectrum correspond to the individual stored ion components, where the slopes encode the respective masses (equation 3.5). The most abundant component at about 10 µs on the vertical axis results from CN^- itself (black dashed line). At $t = 30$ ms, all other components already appear delayed on the vertical axis. The colored solid lines indicate where to expect the traces of the components $^{13}C_2^-$ (pink), $^{13}C^{12}CH^-$ (brown), $^{12}C_2D^-$ (gold) and the vinylidene anion H_2CC^- (orange). The H_2CC^- ion is the heaviest component, while CN^- has the lowest mass.

---

[11] Using the gas target, the second 45° magnet and the subsequent Faraday cup in the CSR transfer beamline (figure 3.2)

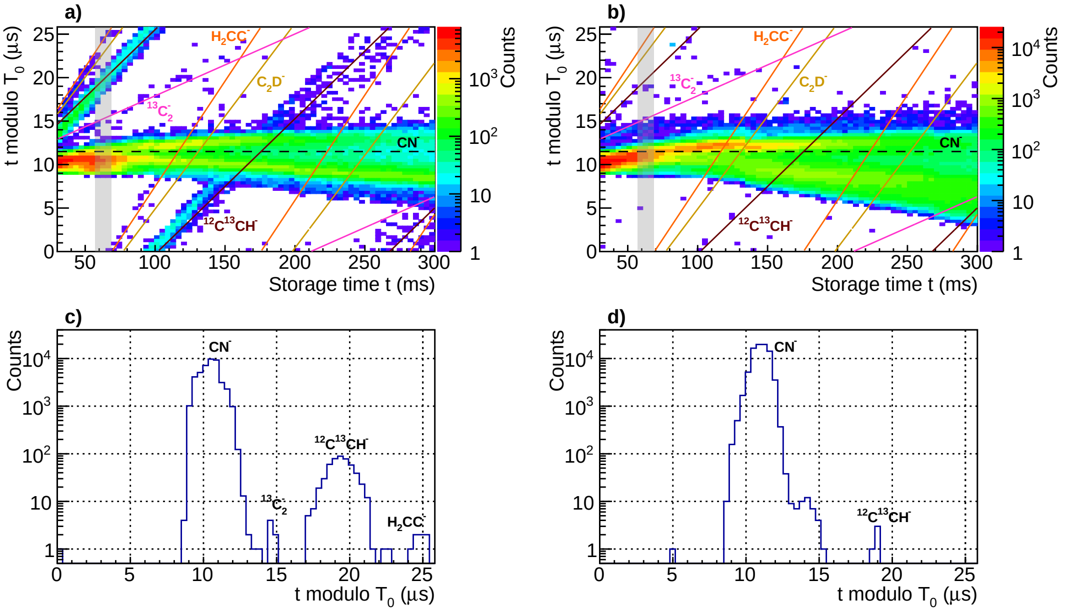

Figure 4.10: Isochronous time-of-flight mass spectra of the MISS revealing the isobaric ion beam components at 26 u and 250 keV kinetic energy: Panel a) and b) show ToF spectra recorded with the COMPACT detector. For more information on the method refer to section 3.2.4. Here, T_0 is the revolution time of the reference ion CN$^-$in the CSR. Dashed and solid lines indicate the expected traces of the components. The data was acquired over a) 0.3 h and b) 2.7 h. Panel c) and d) project the counts within the gray vertical boxes at $t \approx 60$ ms in a) and b) onto the vertical axis. The ion source has two different configurations: In a) and c), the MISS has a Ta cathode and is provided with a mixture of C_2H_4 and atmospheric gas. In b) and d), the MISS has a CuCN/Ag cathode and no gas is let in.

As with the COMPACT scraping technique we directly collect ions from the ion beam halo (section 3.2.4) we can immediately infer the respective fractions of the components in the stored ion beam. This is done in figure 4.10 c). By selecting a slice in figure 4.10 a) (gray box) and projecting its counts onto the vertical axis, we obtain an intensity profile vertically along the slice. This resulting spectrum corresponds to a time-structure of the ion beam along the CSR circumference at a fixed storage time, where the separated ion bunches correspond to the individual isobaric components. The CN$^-$ ion is the most abundant component, followed by ^{13}C^{12}CH$^-$, H$_2$CC$^-$and ^{13}C$_2^-$. For the ^{12}C$_2$D$^-$ ion there are only few counts along the expected trace. Also, within the slice, its trace is so close to the trace of H$_2$CC$^-$ that it does not manifest clearly in the intensity profile. We thus attribute the single count at 0 µs and all counts in the interval 22–26 µs of the profile to H$_2$CC$^-$.

Table 4.1 summarizes the found relative abundances of the components and lists their precise masses. Due to the abovementioned identification issues with ^{12}C$_2$D$^-$ we assume an upper limit of 3×10^{-4} for this ion species. For H$_2$CC$^-$ we obtain a

Table 4.1: Ion beam composition for the H_2CC^-/CN^- ion source configuration derived from figure 4.10 c). EAs, masses and estimates for the photodetachment cross sections σ^{VIS} at 2.33 eV and σ^{UV} at 4.00 eV for ground state molecules are given as well, if available (see footnotes).

Index c	Ion species	Relative abundance	EA (eV)	Mass[a] (u)	σ^{VIS} (10^{-18} cm^2)	σ^{UV}
1	$^{12}C^{12}CH_2^-$	$< 3 \times 10^{-4}$	0.4866 ± 0.0008^b	26.01620	$> 0^c$	$> 0^c$
2	$^{12}C^{14}N^-$	> 0.988	3.864 ± 0.002^d	26.00362	0	5.3 ± 1.1^e
3	$^{12}C^{13}CH^-$	< 0.012	2.969 ± 0.006^f	26.01173	0	5.0 ± 1.3^g
4	$^{13}C_2^-$	$< 2 \times 10^{-4}$	3.269 ± 0.006^h	26.00726	0	$> 0^c$
5	$^{12}C^{12}CD^-$	$< 3 \times 10^{-4}$	2.973 ± 0.006^h	26.01465	0	5.0 ± 1.3^g

[a] All masses as in Grieser et al. 2022 obtained from Wang et al. 2021.
[b] Experimental value from DeVine et al. 2017.
[c] No experimental or theoretical literature values available.
[d] Experimental value from Simpson et al. 2020.
[e] Estimated from experiment by Kumar et al. 2013.
[f] Experimental value from Ervin and Lineberger 1991 for $^{12}C^{12}CH^-$, here assumed for $^{12}C^{13}CH^-$.
[g] Estimated from value measured for $^{12}C^{12}CH^-$ by Best et al. 2011 at 4.03 eV photon energy.
[h] Experimental values from Ervin and Lineberger 1991.

relative faction of $< 3 \times 10^{-4}$. Since during the H_2CC^- lifetime experiment about (1.2–2.2) × 10^7 ions were stored per experimental cycle, each initially stored H_2CC^- ensemble presumably only consisted of about 3600–6600 ions.

For the CN^- ion source configuration, figure 4.10 b) features a much cleaner situation. Here, the CN^- ion is the dominant component and only along the line of $^{13}C^{12}CH^-$ (brown) a significant number of counts accumulates. The intensity profile in figure 4.10 d) implies that the relative fraction of $^{13}C^{12}CH^-$ is $< 5 \times 10^{-5}$. As the MISS was physically disconnected from the gas line, this component may be explained with traces of ethanol[12] left from the cleaning procedure of the ion source. Since there are no counts visible for H_2CC^-, we infer that for the CN^- source configuration its relative fraction is at least an order of magnitude lower than for the H_2CC^-/CN^- source configuration. The small shoulder visible at the right flank of the CN^- peak most likely still results from CN^-, since it does not continue as a trace in figure 4.10 b).

Figure 4.10 a) and c) represent the mixed ion beam intended for the H_2CC^- lifetime experiment. With the EAs of the relevant components in mind (see table 4.1), we can now draw first conclusions about their contributions to the VIS and UV photodetachment signals. For this purpose, table 4.1 also lists, as far as available, their photodetachment cross sections for the photon energies of the VIS (2.33 eV) and UV

---

[12] Sum formula: C_2H_5OH

laser (4 eV). The minor components $c \in [1, 3, 4, 5]$ in table 4.1 contribute to the UV signal via the prefactors $C_c^{\mathrm{UV}} N_c^0$ (see equations 4.29–4.34). The respective photodetachent cross sections σ_c^{UV} are contained in the factors C_c^{UV} and we assume the factors N_c^0 to be proportional to the relative abundances. The known photodetachment cross sections are all of the same order of magnitude. Given the large abundance difference between CN^- and the other components, UV cross sections overestimated by even an order of magnitude would not lead to a significant UV signal fraction from the minor components. For instance, if $\mathrm{H_2CC}^-$ was very long-lived and its photodetachment cross section at the UV photon energy was even an order of magnitude larger than the one of $^{13}\mathrm{C}^{12}\mathrm{CH}^-$ (table 4.1), $\mathrm{H_2CC}^-$ would still contribute only about 0.5% to the UV photodetachment signal. A similar conclusion can be drawn for the stable $^{13}\mathrm{C}_2^-$, which is even less abundant. For the minor components c in the ion beam we can thus assume

$$C_c^{\mathrm{UV}} N_c^0 \ll C_2^{\mathrm{UV}} N_2^0. \tag{4.43}$$

Hence, the approximation made in equations 4.29–4.34 for the UV photodetachment yield,

$$Y_{\mathrm{UV}}(t) \approx C_2^{\mathrm{UV}} N_2^0 e^{-(k_0 + k_2^{\mathrm{RG}} + k_2^{\mathrm{UV}})t}, \tag{4.44}$$

is still valid. From the viewpoint of the relative abundances and the photodetachment cross sections, the $\mathrm{H_2CC}^-$ and CN^- can thus be addressed almost independently by the VIS and UV lasers.

So far we assumed that the 2.33 eV photons of the VIS laser only photodetach the $\mathrm{H_2CC}^-$ ion. This holds true if all beam components are in the ground state. However, the MISS is known to produce rather hot anion ensembles with anions in excited vibrational (Menk et al. 2014), rotational (Meyer et al. 2017) or electronic states (Müll et al. 2021). The additional excitation energy allows photodetachment even below the EA. For the components found in the ion beam, especially the most abundant components $^{13}\mathrm{C}^{12}\mathrm{CH}^-$ and CN^-, we can not exclude a priori that there are excited states contributing to the VIS photodetachment signal.

To check this possibility experimentally, we combine the isochronous ToF mass spectrometry method with laser photodetachment, as described in section 3.2.4. To this end, the stored ion beam is overlapped at a grazing angle with a laser beam provided by the 20 Hz OPO set to the VIS photon energy of 2.33 eV. We then record ToF spectra not via the ion beam halo, but by exclusively counting neutral fragments using the NICE detector. As we only select the events within the short (ns) ToF laser windows, background events are suppressed by the coincidence timing (section 4.3.1). In addition to resolving the ion beam components, the ToF mass spectrum then selectively shows which of those respond to the 2.33 eV photons.

These VIS-photodetachment mass spectra are presented in figure 4.11. The axes of the two-dimensional histograms are the same as in the mass spectra in figure 4.10, and

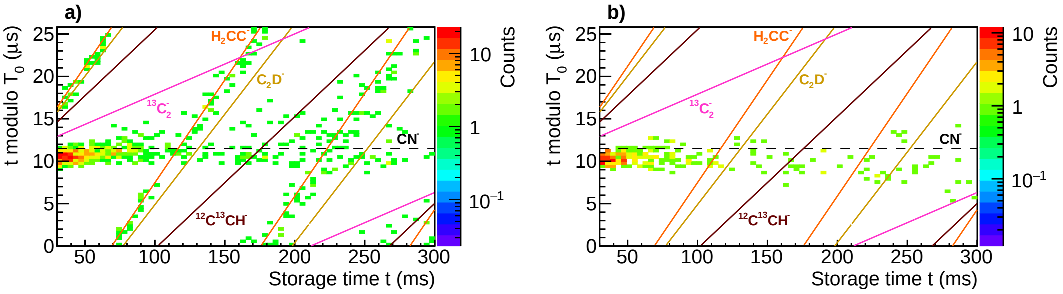

Figure 4.11: Isochronous time-of-flight mass spectra combined with laser photodetachment showing which of the isobars at 26 u respond to 2.33 eV photons: Only the neutral counts resulting from photodetachment are plotted into 2D histograms for ion source configurations of a) H_2CC^-/CN^- and b) CN^- only. The vertical axes represent the storage time t, while the horizontal axes represent t modulo the revolution time T_0 of the reference ion CN^-. The lines show where to expect the different isobaric traces. The laser repetition rate is 20 Hz and the average energy per laser pulse in the ion-photon interaction region is a) 3.6 mJ and b) 3.2 mJ. The data was acquired over a) 17 h and b) 13 h.

the lines indicating the same isobaric traces are drawn. As expected, figure 4.11 a) features a photodetachment signal along the line of H_2CC^- throughout the 300 ms observation time. Furthermore, there is a significant amount of events following the dashed line of the reference ion CN^-. No counts accumulate along the lines of the other components. Unexpectedly, a CN^- trace (much weaker than in figure 4.10) also appears in figure 4.11. Compared to the H_2CC^- trace, it seems to fade out over 300 ms, which may hint at the presence of some ions in a short-lived CN^- state.

To further investigate the CN^- component in the photodetachment signal, we perform dedicated long-time photodetachment measurements with the CN^- source configuration. Here, the CSR is operated in its standard mode, where it is capable of storing the beam for thousands of seconds instead of several seconds in the isochronous mode. Using the same photodetachment laser configuration as above (grazing overlap) we observe that the short-lived component has a lifetime of about 30 ms and that for storage times > 1 s, this component reduces down to the order of the background. We then switch to the VIS laser configuration of the final H_2CC^- lifetime measurement[13] using also comparable VIS laser pulse energy (3.2 mJ). Also here, the number of VIS photodetachment events appears to be on the order of the background for $t > 1$ s. We conclude that this CN^- signal is not relevant and does not have to be included in the model. With regard to its origin, it may result from photodetachment of a highly excited electronic state. For instance, from a spectroscopy experiment on CN^- in a KCl matrix, Mendenhall et al. 1988 reported an excited electronic state with a lifetime of 80 ms at room temperature. It lies 5.6 eV above the ground state. A detailed analysis of the origin of the short-lived component is beyond the scope of this thesis.

---

[13] Nd:YAG laser (10 Hz) at 90° overlap with the ion beam (see figure 4.1 in section 4.2.1).

In summary, the results from the isochronous ToF mass spectrometry and its combination with photodetachment support the feasibility of the original experimental idea. The intended choice of the laser frequencies still ensures that, for storage times $t > 1$ s, H_2CC^- and CN^- can be monitored almost independently. The ratio

$$\frac{Y_{\mathrm{VIS}}(t)}{Y_{\mathrm{UV}}(t)} \approx \tilde{C} e^{-(k_1^{\mathrm{RG}} - k_2^{\mathrm{RG}} + k_1^{\mathrm{VIS}} + k_1^{\mathrm{UV}} - k_2^{\mathrm{UV}} + k)t} \tag{4.45}$$

of the VIS and UV photodetachment yields then contains the decay rate k related to the intrinsic lifetime of the ground state H_2CC^- ion.

4.4 Experimental results

Based on the preliminary measurements, we discuss here the experimental results of the H_2CC^- lifetime experiment. The goal of the experiment is to determine the intrinsic lifetime of the ground state vinylidene anion H_2CC^-. To this end, ensembles of H_2CC^- and the stable reference ion CN^- are stored in the cryogenic environment of the CSR and the decay of both ion species is monitored simultaneously by means of photodetachment and a single-particle counting detector (details in section 4.2.1). According to the model in sections 4.2.3–4.2.4, we expect the H_2CC^- ensemble to be subject to a single exponential decay with an effective decay rate (equation 4.28 in section 4.2.4):

$$k_1^{\mathrm{eff}} = k_0 + k_1^{\mathrm{RG}} + k_1^{\mathrm{UV}} + k_1^{\mathrm{VIS}} + k. \tag{4.46}$$

This effective rate already contains the rate k ascribed to the intrinsic H_2CC^- lifetime. All other rates result from external effects acting on the stored H_2CC^- ensemble and add to the measured effective rate k_1^{eff}. The latter rate thus marks an upper limit for k and a lower limit $1/k_1^{\mathrm{eff}}$ for the intrinsic H_2CC^- lifetime.

By comparing the decay of H_2CC^- and CN^-, we expect to suppress the external effects and observe a single exponential decay with an effective decay rate (equation 4.41)

$$k^{\mathrm{eff}} = \overbrace{k_1^{\mathrm{RG}} - k_2^{\mathrm{RG}}}^{\Delta k^{\mathrm{RG}}} + \overbrace{k_1^{\mathrm{UV}} - k_2^{\mathrm{UV}}}^{\Delta k^{\mathrm{UV}}} + k_1^{\mathrm{VIS}} + k. \tag{4.47}$$

Here, the rate k_0 resulting from storage-ring induced effects is canceled, and the CN^- ion contributes the additional rates k_2^{RG} and k_2^{UV}. They partly cancel the effective contribution Δk^{RG} of CED from collisions with the residual gas and UV laser depletion (Δk^{UV}), and may even change their mathematical sign. In contrast to k_1^{eff}, the effective rate k^{eff} may thus no longer mark the absolute upper limit for k. In order to account for this possibility, the individual contributions to k^{eff} have to be estimated quantitatively.

Below, we present and discuss the obtained effective decay rates (section 4.4.1). Furthermore, we check important experimental parameters (sections 4.4.2 and 4.4.3). The contributions by Δk^{RG} and Δk^{UV} are addressed in the context of section 4.4.1.2.

4.4.1 Effective decay rate of H_2CC^-

A mixed ion ensemble of H_2CC^- and CN^- is stored in the CSR for 3000 s and the laser yield ratio $Y_{\mathrm{UV}}^{\mathrm{VIS}}(t)$ (equation 4.36 in section 4.2.4) is determined as a function of the storage time t. The data are processed as described in appendix B.2. For completeness, the VIS laser yield $Y^{\mathrm{VIS}}(t)$ is determined as well, with the data being processed in a similar manner as for $Y_{\mathrm{UV}}^{\mathrm{VIS}}(t)$. In section 4.4.1.1 we give the experimental results. A detailed discussion of possible systematic effects can be found in section 4.4.1.2.

4.4.1.1 Results

The results are presented in figure 4.12, where the yield $Y^{\mathrm{VIS}}(t)$ and the yield ratio $Y_{\mathrm{UV}}^{\mathrm{VIS}}(t)$ are plotted against t. Each data point represents an average over 250 s of storage time. The data sets are recorded for different VIS laser pulse energies E^{VIS} in the ion-photon interaction region. The respective E^{VIS} values are given at the top of each column. As we are interested in decay rates, the chosen vertical-scale presentation emphasizes the time-dependence of the acquired data while ensuring that the individual datasets remain visually comparable among each other (details see figure caption). The absolute scale is not relevant in this context and thus addressed at the end of this section.

The displayed error bars purely result from the statistical uncertainties of the laser-induced signal and the background signal. From detailed uncertainty estimates given in appendix B we find that the statistical uncertainties, foremost the counting uncertainties of the VIS-induced events, clearly dominate the uncertainty budget (see table B.1 in appendix B.3). Hence, we do not include the systematic uncertainties at this point.

As a general trend in figure 4.12 we observe that both the yield and the yield ratio decay as the storage time progresses. After about 1100 s the fastest-decaying yield signal (figure 4.12 a) has decreased from initially 11 J^{-1} to about 4 J^{-1}. In contrast, the fastest-decaying component of the VIS/UV yield ratio (figure 4.12 e) decreases by only a factor of 2 over 3000 s.

In order to obtain the effective rate k_1^{eff} (equation 4.46), we fit a single exponential function to each of the $Y^{\mathrm{VIS}}(t)$ yield curves in figure 4.12. The fits are indicated by solid lines. Generally, for ion beams stored in the CSR we observe a faster decay at short storage times, leading to a non-exponential signal decay curve. This effect is stronger if more ions are stored and thus likely related to space charge effects. In the decay model, these effects are incorporated in the rate $k_0(t)$. In order to suppress the contribution

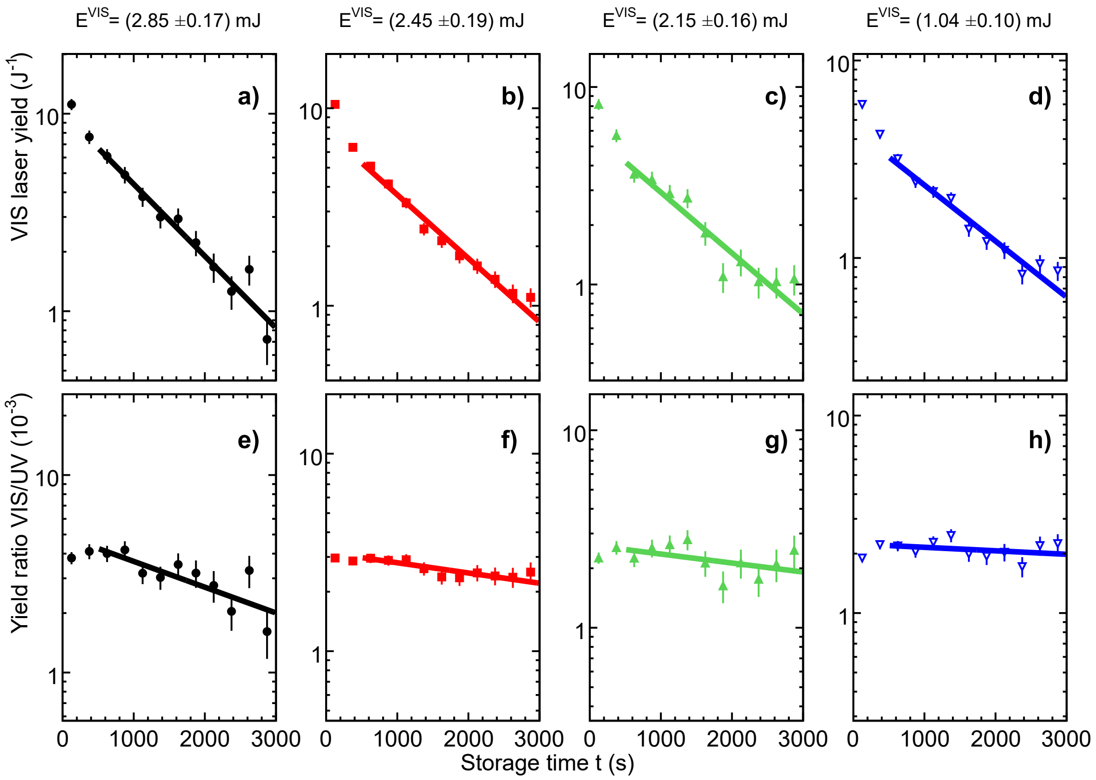

Figure 4.12: a)–d) VIS laser yield $Y^{\rm VIS}(t)$ and e)–h) VIS/UV yield ratio $Y_{\rm UV}^{\rm VIS}(t)$ plotted against the storage time t for different average VIS laser pulse energies $E^{\rm VIS}$ in the ion-photon interaction region, as given at the top of each column. The solid curves in a)–h) are single exponential fits to the data points with reduced chi-squared values in the range a)–d) $\chi^2_{\rm red} = 0.75$–1.65 and e)–h) $\chi^2_{\rm red} = 0.44$–1.25. To emphasize the time-dependence of the recorded data (independent of the absolute scale) we chose the vertical-scale presentation such that per row, the first data point in each panel always appears at the same vertical position. To ensure that the time dependence among all panels remains comparable, there is always a constant factor of 45 between the upper and lower limit of the vertical scale in a)–h).

of the initial non-exponential decay component, we apply the fits in figure 4.12 a)–d) starting from 500 s.

The fits yield effective decay rates in the range $k_1^{\rm eff} = (6.5$–$8.4) \times 10^{-4}$ s^{-1} and corresponding statistical uncertainties $\Delta k_1^{\rm eff}/k_1^{\rm eff} = 5$–$9\%$ given by the fit. The fitted effective decay rate of the data set with the lowest VIS pulse energy ($E^{\rm VIS} = 1.04$ mJ) corresponds to a lifetime of $1/k_1^{\rm eff} = 1530^{+100}_{-90}$ s, which is the longest lifetime that we observe for the VIS laser yield. According to equation 4.46 this value represents a *lower limit* for the intrinsic H_2CC^- lifetime.

We now determine the effective rate $k^{\rm eff}$ (equation 4.47) by fitting a single exponential function to each of the yield ratios $Y_{\rm UV}^{\rm VIS}(t)$ in figure 4.12 e)–h). Here, we observe that the yield ratio either stays constant or increases in the first 500 s. As all beam species are well mixed in the standard operation mode of the CSR, the loss effects from space charge equally affect all components of the ion ensemble. Furthermore, we expect the rate $k_0(t)$ incorporating the space charge to be canceled in the effective rate of the yield ratio (equation 4.47). The initial behavior is thus likely related to the UV laser yield $Y_{\text{UV}}(t)$. Due to an excited-state component with a lifetime on the order of ~ 100 s, it may decay faster than the VIS laser yield and lead to an increase of the yield ratio in the first 500 s. The UV laser yield is dominated by the most abundant beam component CN^- (equation 4.35). As vibrationally excited states typically have a lifetime on the order of milliseconds, the component may result from CN^- in excited rotational states. Since the signal appears to decay uniformly from 500 s onward, we also here limit the fit range to 500–3000 s.

The fit to the fastest-decaying yield ratio (highest VIS pulse energy) gives an effective rate $k^{\text{eff}} = (3.0 \pm 0.7) \times 10^{-4}\ \text{s}^{-1}$, while the effective rate of the fit to the slowest-decaying data set (lowest VIS pulse energy) reaches down to $k^{\text{eff}} = (4.0 \pm 3.9) \times 10^{-5}\ \text{s}^{-1}$. The large relative uncertainty of this smallest decay rate makes the rate almost compatible with zero. The given rates correspond to effective lifetimes $\tau^{\text{eff}} = 1/k^{\text{eff}} \approx 3300$ s and $\tau^{\text{eff}} \approx 24000$ s, respectively.

In order to estimate the systematic uncertainties of the fitted rates, we repeat the fits after having incorporated the uncertainties of the laser pulse energies. These uncertainties are dominated by the systematic drift of the VIS laser intensity (see appendix table B.1). Also, we repeat the fits using alternative thresholds for the pulse-height cuts, i.e., $U_{\text{pulse}} \in \{-0.25\ \text{V}, -0.3\ \text{V}\}$ instead of -0.2 V. The final rates and lifetimes with systematic uncertainties are then

$$k^{\text{eff}} = 3.006(\pm 0.668)_{\text{stat}}(^{+0.006}_{-0.026})_{\text{sys}} \times 10^{-4}\ \text{s}^{-1} \tag{4.48}$$

for the fastest-decaying data set and

$$k^{\text{eff}} = 4.08(\pm 3.91)_{\text{stat}}(^{+0.01}_{-0.16})_{\text{sys}} \times 10^{-5}\ \text{s}^{-1} \tag{4.49}$$

for the slowest-decaying data set. Compared to the statistical uncertainties, the effect of the included systematic uncertainties is negligible.

As we observed from figure 4.12, the fitted effective decay rates strongly differ for different values of the VIS laser pulse energy E^{VIS} in the ion-photon interaction region. The effective rates decrease for lower E^{VIS}, and hence also for lower values of the associated rates k_1^{VIS} (see equation 4.3 in section 4.2.3, and equation 4.21 in section 4.2.4). In order to eliminate the contributions of k_1^{VIS} in the effective rates (equations 4.46 and 4.47), we use the fitted effective rates and the corresponding VIS pulse energies of figure 4.12 for an extrapolation. In figure 4.13, we plot the effective rates k_1^{eff} (black dots) and k^{eff} (red squares) against the corresponding E^{VIS} values given in figure 4.12. The vertical error bars are the uncertainties delivered by the exponential fits from figure 4.12 and reflect the statistical uncertainties, as the fits were only fed with statistical

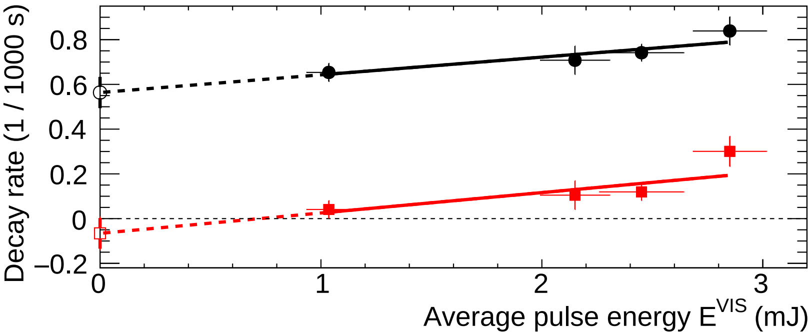

Figure 4.13: The measured effective decay rates k_1^{eff} (decay rate of $Y^{\mathrm{VIS}}(t)$, black dots) and k^{eff} (decay rate of $Y_{\mathrm{UV}}^{\mathrm{VIS}}(t)$, red squares) are plotted against the average VIS laser pulse energy E^{VIS} in the ion-photon interaction region. The rate and E^{VIS} values are obtained from figure 4.12. The fitted lines extrapolate to $E^{\mathrm{VIS}} = 0$, i.e., effective decay rates free from depletion due to the VIS laser (hollow circle and square with error bars). The horizontal dashed line marks a decay rate of zero. The reduced chi-squared values are $\chi^2_{\mathrm{red}} = 0.51$ (upper fit) and $\chi^2_{\mathrm{red}} = 1.90$ (lower fit).

uncertainties. The horizontal error bars are the uncertainties of E^{VIS}, both displayed in the legend in figure 4.12. They are determined from the pulse energy distribution of all VIS laser shots fired for obtaining the corresponding data sets for the exponential fits. While the mean of the distribution is E^{VIS}, its standard deviation estimates ΔE^{VIS}. As each data set was acquired over several hours, the statistical fluctuation of the laser intensity is negligible compared to its systematic drift (see appendix table B.1). The horizontal error bars thus almost purely reflect systematic uncertainties.

Both k_1^{eff} and k^{eff} appear to increase approximately linearly with E^{VIS}. We thus fit a linear function (straight lines) to each of the two data sets and extrapolate to $E^{\mathrm{VIS}} = 0$ (dashed lines). The values at the intercept with the vertical axis are then the effective rates free from depletion by the VIS laser ($k_1^{\mathrm{VIS}} = 0$ in equations 4.46 and 4.47). It is important to note that for the displayed fit we only consider statistical uncertainties (vertical error bars).

The two fitted lines appear to have similar slopes. While for k_1^{eff} the VIS depletion-free rate $k_1^{\mathrm{eff},0} = k_1^{\mathrm{eff}}(E^{\mathrm{VIS}} = 0)$ is positive and lower than all other points of the data set (black dots), the depletion-free value $k^{\mathrm{eff},0} = k^{\mathrm{eff}}(E^{\mathrm{VIS}} = 0)$ of the lower data set (red squares) is negative, but still agrees with zero within the error bar.

We now include the systematic uncertainties. We incorporate the horizontal error bars (systematic laser intensity fluctuation) into the linear fits. Furthermore, we include systematic uncertainties into the rate uncertainties (vertical error bars). As the rate of each data point is given by an exponential fit (figure 4.12), we repeat each exponential fit with the two abovementioned systematic contributions incorporated, i.e., the systematic laser intensity fluctuations and the alternative choice of pulse-height cuts. We then obtain

$$k_1^{\mathrm{eff},0} = 5.64(\pm 0.70)_{\mathrm{stat}}(^{+0.00}_{-0.04})_{\mathrm{sys}} \times 10^{-4}\ \mathrm{s}^{-1} \tag{4.50}$$

for the VIS laser yield and

$$k^{\mathrm{eff},0} = -6.6(\pm 6.9)_{\mathrm{stat}}(^{+0.0}_{-1.1})_{\mathrm{sys}} \times 10^{-5}\ \mathrm{s}^{-1} \tag{4.51}$$

for the VIS depletion-free effective rate of the VIS/UV yield ratio. For the VIS yield, the systematic uncertainties are again negligible compared to the statistical uncertainties. The systematic uncertainties of k^{eff} are about 16% of the statistical uncertainties. With the systematic uncertainties included, the VIS depletion-free rate still agrees with zero within 1σ. Additionally, a detailed discussion of possible systematic effects, which we give for completeness in the following section 4.4.1.2, comes to the conclusion that indeed the negative value of $k^{\mathrm{eff},0}$ is of purely statistical nature.

The extrapolation confirms that the depletion k_1^{VIS} due to the VIS laser significantly adds to the measured effective rates. The dependence of the effective rates on the average pulse energy E^{VIS} has a linear trend. For the k_1^{eff} data set (black line and dots) the data points match the linear fit well within the statistical uncertainties represented by the vertical error bars. The first three data points of the k^{eff} data set (red line and squares) agree well with the fit, while the last data point (highest E^{VIS}) agrees with the fit within 2σ. Also here, we discuss possible systematic effects in section 4.4.1.2 and conclude that this last data point is a statistical outlier.

Even though the absolute scaling of the yield $Y^{\mathrm{VIS}}(t)$ and the yield ratio $Y^{\mathrm{VIS}}_{\mathrm{UV}}(t)$ in figure 4.12 is not relevant for the extracted rates, we here address this point shortly. We observe that the signal amplitudes decrease as E^{VIS} decreases. Since $Y^{\mathrm{VIS}}(t)$ and $Y^{\mathrm{VIS}}_{\mathrm{UV}}(t)$ were each normalized by the laser pulse energies in the interaction region, the decrease is not laser-related. Based on the assumption that the ion of interest is the dominant ion beam component, we usually also normalize to the number of initially stored ions of each experimental cycle in order to account for fluctuations between the cycles. As in our case the reference ion CN^- was the dominant component and the ion of interest H_2CC^- only amounted to a minor fraction, we had no means to normalize to the H_2CC^- ion number. The decrease is thus likely related to the ion source, which, by coincidence and not intentionally, delivered a decreasing H_2CC^- fraction along with decreasing photodetachment laser pulse energies E^{VIS} over the course of the experiment.

In summary, by simultaneously comparing the exponential decay of H_2CC^- and CN^- ion ensembles stored in the cryogenic environment of the CSR we observed an effective lifetime of

$$\tau^{\mathrm{eff}} = \frac{1}{k^{\mathrm{eff}}} = 24490(^{+549200}_{-11980})_{\mathrm{stat}}(^{+1040}_{-50})_{\mathrm{sys}}\ \mathrm{s} \tag{4.52}$$

in the case of the lowest VIS pulse energy $E^{\mathrm{VIS}} = 1.04$ mJ (k^{eff} see equation 4.49). Complementary to this lifetime, we observed that the stored H_2CC^- ensemble alone lives for about 1500 s. In the latter case, external effects such as laser depletion and CED due to collisions with the residual gas, or storage-ring induced effects are not yet suppressed. Extrapolation of k^{eff} to a rate $k^{\mathrm{eff},0}$ (see equation 4.51) free from depletion by the VIS laser even yields a value which is compatible with zero within the statistical uncertainties.

The next section discusses in detail possible systematic effects and, as mentioned above, comes to the conclusion that the experimental results can be explained purely by statistical uncertainties. The subsequent sections corroborate the results by estimating important experimental parameters, i.e., the residual gas density (section 4.4.2) and the $\mathrm{H_2CC^-}$ photodetachment cross section at the VIS laser pulse energy (section 4.4.3).

4.4.1.2 Detailed discussion of possible systematic effects

Even though the deviation of the yield ratio value for highest E^{VIS} (rightmost red data square in figure 4.13) from the fit and the observed negative value of $k^{\mathrm{eff},0}$ (equation 4.51) are acceptable within the statistical limits, these features only appear once the UV photodetachment signal (dominated by $\mathrm{CN^-}$) is involved. Also, including this signal does not seem to increase the absolute statistical uncertainties (vertical error bars) compared to the VIS-only signal (black data dots). This may hint at possible systematic effects, which we discuss in the following. We first address the contributions to the effective rate k^{eff} (equation 4.47) and then turn to possible systematic effects which are not yet incorporated. Finally, we reconsider some assumptions made during the modeling of the photodetachment signals (section 4.2.4).

The term $\Delta k^{\mathrm{RG}} = k_1^{\mathrm{RG}} - k_2^{\mathrm{RG}}$ is the first contribution to equation 4.47. It is the difference between the Collisional Electron Detachment (CED) decay rates of the $\mathrm{H_2CC^-}$ and $\mathrm{CN^-}$ ensembles due to collisions with residual gas particles. If $\Delta k^{\mathrm{RG}} < 0$, the negative value of $k^{\mathrm{eff},0}$ may result from the absolute difference of the decay rates. In order to estimate Δk^{RG}, the CED cross sections σ_1^{RG} and σ_2^{RG} for both ion species impinging on $\mathrm{H_2}$ with a kinetic energy of 250 keV have to be known (see equation 4.2). As the CSR is operated at about 10 K, $\mathrm{H_2}$ is by far the most abundant component of the residual gas in the experimental vacuum chamber (Hahn et al. 2016). Apart from the cross sections, the value of the residual gas density n^{RG} is also required. In the literature σ_1^{RG} is only available for $\mathrm{H_2CC^-}$ impinging either on $\mathrm{N_2}$ or $\mathrm{O_2}$ at < 10 keV kinetic energy (Hernández and Hinojosa 2018). According to the experiment of Jalbert et al. 2014, the CED cross section of $\mathrm{CN^-}$ colliding with $\mathrm{N_2}$ at 250 keV kinetic energy is about $\sigma_2^{\mathrm{RG}} \approx 13 \times 10^{-16}$ cm^2. While the upper limit for n^{RG} can be estimated with this value (see section 4.4.2), the literature does not provide values for the cross sections σ_1^{RG} and σ_2^{RG} at 250 keV with $\mathrm{H_2}$ as target. We thus resort to comparing measured CED cross sections for a case very similar to ours, i.e., of $\mathrm{CN^-}$ and $\mathrm{C_2H^-}$ colliding with $\mathrm{N_2}$: At a kinetic energy of about 90 keV, the cross section is still $\sigma_2^{\mathrm{RG}} \approx 13 \times 10^{-16}$ cm^2 (Jalbert et al. 2014), while for $\mathrm{C_2H^-}$ the cross section is about $\sigma^{\mathrm{RG}} \approx 26 \times 10^{-16}$ cm^2

(Nascimento et al. 2013). As H_2CC^- only differs from C_2H^- by one H atom, we assume its CED cross section σ_1^{RG} to be similar or larger. With $\sigma_1^{\mathrm{RG}} > \sigma_2^{\mathrm{RG}}$, we get $\Delta k^{\mathrm{RG}} > 0$ according to equation 4.2. The contribution Δk^{RG} can thus not explain the negative value of $k^{\mathrm{eff},0}$.

What remains to be discussed is whether Δk^{RG} can explain the outlier data point. According to equation 4.2 the loss rates k_i^{RG} are proportional to the residual gas density n^{RG}. If n^{RG} changes over time, e.g., due to a drifting temperature of the CSR experimental chambers, Δk^{RG} and its contribution to the effective rate k^{eff} are affected as well. Provided that Δk^{RG} is the dominant contribution in k^{eff}, the 50% step between the outlier and the neighboring data point at $E^{\mathrm{VIS}} = 2.45$ mJ may be related to a drift of n^{RG}. The relative change of the residual gas density between the individual experimental cycles can be estimated without knowing the CED loss rates and cross sections: It is sufficient to watch how the total number of CED events N^{CED} normalized to the number of stored ions N_0 changes. Both quantities are known for each experimental cycle of the H_2CC^- lifetime experiment. While N^{CED} is the sum of all noise-corrected background events at the counting detector, N_0 is determined from the capacitive pick-up signal (Hahn et al. 2016) at $t = 1$ ms storage time and lies in the range of about $(1.2–2.2) \times 10^7$. Between the outlier and the neighboring point N^{CED}/N_0 only decreased by about 6%, which translates to the same relative change of n^{RG} and Δk^{RG}. We conclude that the temporal drift in the residual gas density is too small to explain the 50% step of the outlier.

The second contribution to equation 4.47 is the term $\Delta k^{\mathrm{UV}} = k_1^{\mathrm{UV}} - k_2^{\mathrm{UV}}$ resulting from depletion of both H_2CC^- and CN^- by the UV laser. Even though the photodetachment cross section of H_2CC^- is not known, we can make a rough estimate: We assume that the UV photon energy (4.0 eV) is far enough from the EA of H_2CC^- (0.49 eV, see table 4.1 in section 4.3.3.2) for its photodetachment cross section to be approximately zero (section 1.2). The UV depletion term is then approximately the depletion rate of CN^- (equation 4.4). With the luminosity (equations 4.20 and 4.21) it can be expressed in terms of known variables:

$$\begin{aligned}
\Delta k^{\mathrm{UV}} &\approx -k_2^{\mathrm{UV}} && (4.53)\\
&= -\sigma_2^{\mathrm{UV}} r^{\mathrm{UV}} L^{\mathrm{UV}} && (4.54)\\
&= -\sigma_2^{\mathrm{UV}} r^{\mathrm{UV}} \frac{N_\gamma^{\mathrm{UV}}}{l_{\mathrm{max}} C_{\mathrm{CSR}}} && (4.55)\\
&= -\sigma_2^{\mathrm{UV}} r^{\mathrm{UV}} \frac{E^{\mathrm{UV}}}{l_{\mathrm{max}} C_{\mathrm{CSR}} E_\gamma^{\mathrm{UV}}} && (4.56)\\
&\approx -1.2 \times 10^{-6}\ \mathrm{s}^{-1} && (4.57)
\end{aligned}$$

In the last step, we used the CN^- photodetachment cross section at $E_\gamma^{\mathrm{UV}} = 4.0$ eV (table 4.1), the UV laser repetition rate $r^{\mathrm{UV}} = 20$ Hz, the average UV pulse energy in the ion-photon interaction region $E^{\mathrm{UV}} = 30$ µJ, the maximum beam height $l_{\mathrm{max}} = 1$ cm and the closed-orbit circumference $C_{\text{CSR}} = 35.12$ m of the CSR. The contribution Δk^{UV} is negative and only amounts to 1.8% of $k^{\text{eff},0}$. Given the initial assumption about the photodetachment cross section of H_2CC^-, we already estimated the upper limit of Δk^{UV}. The negative value of $k^{\text{eff},0}$ is thus corrected only slightly. The absolute contribution of Δk^{UV} is also too small to explain the outlier data point. Hence, the contribution by the UV laser depletion does not explain the observed irregularities.

The remaining contributions to k^{eff} (equation 4.47) are the depletion rate k_1^{VIS} due to the VIS laser and the rate k attributed to the intrinsic lifetime of H_2CC^-. Both contributions are positive and thus do not explain the negative value of $k^{\text{eff},0}$. Furthermore, the linear trends in both data sets in figure 4.13, which we attributed to the rate k_1^{VIS}, are very similar. As the outlier only appears in the k^{eff} data set, k_1^{VIS} likely does not explain the outlier data point.

The contributions to the effective rate k^{eff} do not seem to account for the observed irregularities. This raises the question if there is an additional systematic effect not yet taken into account. Provided that the systematic effect manifests as a loss rate $k_{\text{sys}} > 0$, there are different scenarios, which we discuss in the following.

In the first scenario, the systematic effect results from the VIS laser yield. It then adds to both k_1^{eff} and k^{eff} (equations 4.46 and 4.47):

$$k_1^{\text{eff}} + k_{\text{sys}} \tag{4.58}$$

$$k^{\text{eff}} + k_{\text{sys}} \tag{4.59}$$

Here, possible candidates for a systematic effect are processes such as multi-photon detachment of H_2CC^- by black-body radiation or fragmentation processes of H_2CC^- induced by one or multiple VIS photons. If such a systematic effect was responsible for the outlier data point in the k^{eff} data set, it should be visible in the k_1^{eff} data set as well. However, this is not the case. In addition, $k_{\text{sys}} > 0$ does not explain the negative value of $k^{\text{eff},0}$. The scenario with a systematic effect resulting from the VIS laser yield thus seems unlikely.

The second scenario is that k_{sys} only contributes to the UV laser yield and thus lowers the effective rate:

$$k^{\text{eff}} - k_{\text{sys}} \tag{4.60}$$

In the ion-photon interaction region, the UV laser pulse energy is about 30–100 times lower than the VIS laser pulse energy. Effects related to high photon densities likely do not play a role here. Apart from CN^- the UV photodetaches all other beam components (see table 4.1). With about 1.2% relative abundance, $^{13}C^{12}CH^-$ is the second-most abundant component in the ion beam. Even though its photodetachment cross section at the UV photon energy (4.0 eV) is in the worst case about 50% higher than the photodetachment cross section of CN^-, its effective contribution to the UV laser yield is still less than 2%. This is too low to explain the outlier data point or the negative value of $k^{\mathrm{eff},0}$.

In the third scenario, k_{sys} adds to both the VIS and UV laser yield and is larger for one of either yields. The effective contribution in k^{eff} is then either positive or negative. An example for such a contribution would be effects related to the mass-to-charge ratio m/q of the stored ions. However, for the stored ions, the relative difference in m/q is $< 5 \times 10^{-4}$, which makes such effects unlikely candidates for explaining the observed irregularities.

As the considered systematic effects do not explain the outlier and the negative value of $k^{\mathrm{eff},0}$, we now reconsider the assumptions made in the model in section 4.2.4 in the context of equations 4.11–4.13: We assumed that the ions do not move in the ion-photon interaction region on the time scale $t_{\mathrm{VIS}} \approx 5$ ns it takes a laser pulse to pass by. Furthermore, we assumed that the VIS laser does not bleach the $\mathrm{H_2CC^-}$ ions in the interaction region.

In order to check the first assumption we presume that the laser beam illuminates the ions over a distance of $l_1 = 1$ cm. Covering this distance takes singly-charged ions with a mass $m = 26$ u and a kinetic energy of $E_{\mathrm{kin}} = 250$ keV about

$$t_1 = \frac{l_1}{v} = l_1 \sqrt{\frac{m}{2E_{\mathrm{kin}}}} \approx 7.3 \text{ ns.} \tag{4.61}$$

This value is on the order of the laser pulse duration t_{VIS}, which renders the assumption incorrect. While the laser pulse passes by, the ions cover a distance of $l_2 = t_{\mathrm{VIS}}/v \approx 0.7$ cm. The laser beam thus addresses an ion beam fraction which is about a factor of

$$C_{\mathrm{VIS}} = \frac{l_1 + l_2}{l_1} \approx 1.7 \tag{4.62}$$

larger than expected. Both the ion velocity and the laser pulse duration remain constant in first order. Since this effect does not propagate to k^{eff}, other than including the factor C_{VIS} in equation 4.12, no further correction is required.

We now turn to determining the significance of the bleaching effect: Bleaching occurs if, with each shot, the VIS laser removes most ions from the ion-photon interaction region so that not enough ions are left for photodetachment. Increasing the energy per laser pulse E^{VIS} then does not increase the yield Y^{VIS}. This effect would thus complicate the interpretation of the data in figure 4.13. Whether bleaching occurs within the relevant storage time range (500–3000 s) can be estimated from the VIS laser yield $\tilde{Y}^{\mathrm{VIS}} \approx 6$ J^{-1} (third black data dot from the left in figure 4.12 a) and the corresponding average laser pulse energy $\tilde{E}^{\mathrm{VIS}} = 2.85$ mJ. During the acquisition of the black data set, the initial number of stored ions was on average $\overline{N}_0 \approx 1.59 \times 10^7$. From observing the CED detector events we estimate that in the storage time interval of the third data point (500–750 s) $\overline{N}_0$ has decreased to a fraction of minimum $\eta_1 \approx 1/7$. Apart from the total number of ions, we also require the relative $\mathrm{H_2CC^-}$ fraction

$\eta_2 \approx 3 \times 10^{-4}$ (table 4.1) in the beam and the fraction η_{int} of H_2CC^- in the ion-photon interaction region. This fraction is obtained from the ratio l_1/C_{CSR} between the length l_1 (equation 4.61) of the interaction region and the closed-orbit circumference $C_{\text{CSR}} = 35.12$ m of the CSR. Furthermore, the detection efficiency $\epsilon = 0.593$ (section 4.2.4) of the MCP-based counting detector and the factor C_{VIS} (equation 4.62) have to be taken into account. On average, the VIS laser then photodetaches an ion fraction of

$$\eta_{\text{det}} = \frac{\tilde{Y}^{\text{VIS}}\tilde{E}^{\text{VIS}}}{\overline{N}_0 C_{\text{VIS}}\epsilon\ \eta_1\ \eta_2\ \eta_{\text{int}}} \tag{4.63}$$

$$= \frac{\tilde{Y}^{\text{VIS}}\tilde{E}^{\text{VIS}}C_{\text{CSR}}}{\overline{N}_0 C_{\text{VIS}}\epsilon\ \eta_1\ \eta_2\ l_1} \approx 9\% \tag{4.64}$$

in the ion-photon interaction region. Considering that subsequent laser shots do not hit the same ions and that the stored beam ensemble continuously mixes while revolving in the CSR, we conclude that the bleaching effect is not critical. This is also supported by the observation that the yield Y^{VIS} in figure 4.13 does not flatten or saturate as E^{VIS} increases.

In short, none of the considered systematic effects sufficiently explains the 50% step of the outlier data point and the negative value of $k^{\text{eff},0}$. Furthermore, the assumptions made in the model are still acceptable. As the data point statistically agrees with the linear fit within 2σ and $k^{\text{eff},0}$ agrees with zero within 1σ, we conclude the observed features are of purely statistical nature.

4.4.2 Residual gas density and vacuum pressure

Here we use the results obtained in figure 4.13 for estimating the upper limit of the average residual gas density n^{RG} in the experimental chambers of the CSR.

The effective rates in figure 4.13 result from the VIS laser yield (black data dots) and the VIS/UV yield ratio (red data squares). According to the definition of the yields (see equations 4.25–4.35) and their ratio (see equations 4.36–4.41), the difference

$$k_1^{\text{eff}} - k^{\text{eff}} = k_0 + k_2^{\text{RG}} + k_2^{\text{UV}} \tag{4.65}$$

$$= k_2^{\text{eff}} \tag{4.66}$$

between the two data sets in figure 4.13 corresponds to the effective rate k_2^{eff} at which the UV laser signal and hence the most abundant ion beam component CN^- decays. With equation 4.2 for the CED loss rate k_2^{RG} of CN^- we get:

$$k_2^{\text{eff}} = k_0 + \sigma_2^{\text{RG}} v_2 n^{\text{RG}} + k_2^{\text{UV}} \tag{4.67}$$

We rearrange for the residual gas density n^{RG} and neglect $k_0 > 0$ in the last step. As a result, we obtain an upper limit

$$n^{\mathrm{RG}} = \frac{k_2^{\mathrm{eff}} - k_0 - k_2^{\mathrm{UV}}}{\sigma_2^{\mathrm{RG}} v_2} \tag{4.68}$$

$$< \frac{k_2^{\mathrm{eff}} - k_2^{\mathrm{UV}}}{\sigma_2^{\mathrm{RG}} v_2}. \tag{4.69}$$

For the difference between rates of the two data sets in figure 4.13 we get a range of $k_2^{\mathrm{eff}} = (5.4–6.2) \times 10^{-4}\ \mathrm{s}^{-1}$. For the following estimate of the upper limit, we take the highest value from this range. As the CED cross sections for CN^- impinging on H_2 at the kinetic energy of 250 keV is not available, we take the value $\sigma_2^{\mathrm{RG}} \approx 13 \times 10^{-16}\ \mathrm{cm}^2$ obtained with N_2 as target (Jalbert et al. 2014). For the mass-to-charge ratio of CN^-(table 4.1 in section 4.3.3.2), this kinetic energy corresponds to a CN^- velocity of $v_2 \approx 1.36 \times 10^6\ \mathrm{ms}^{-1}$. With $k_2^{\mathrm{UV}} \approx 1.2 \times 10^{-6}\ \mathrm{s}^{-1}$(see equations 4.53–4.57) we get

$$n^{\mathrm{RG}} \lesssim 3500\ \mathrm{cm}^{-3} \tag{4.70}$$

for the upper limit of the residual gas density during the $\mathrm{H_2CC}^-$ lifetime experiment. Note that this value represents an average residual gas density inside the CSR, as it is determined from decays and not from instantaneous rates at the counting detector. For $T = 300$ K, this corresponds to a Room-Temperature Equivalent (RTE) pressure (Hahn et al. 2016) of

$$p_{\mathrm{RTE}} = n^{\mathrm{RG}} k_B T < 1.5 \times 10^{-13}\ \mathrm{mbar}. \tag{4.71}$$

This value is lower than, e.g., the RTE pressures during the second Si^- measurement campaign carried out at the CSR in 2018 (Müll 2023): Throughout that campaign the CSR refrigeration system was not operating in a stable manner, which lead to temperature fluctuations of the CSR experimental chambers and consequently the vacuum pressure varied strongly. Additionally, the chambers had not been baked out. As a result, the vacuum pressures varied in the range $p_{\mathrm{RTE}} = (2–50) \times 10^{-13}$ mbar during the Si^- campaign. Considering that at the time of the $\mathrm{H_2CC}^-$ lifetime experiment the chambers were baked out and the temperature was stable, the estimated upper limit of the RTE vacuum pressure is reasonable.

4.4.3 Photodetachment cross section far from threshold

The $\mathrm{H_2CC}^-$ lifetime experiment is based on probing the ion population by photodetachment. The photodetachment cross section of $\mathrm{H_2CC}^-$ is thus one of the central parameters, especially its value σ_1^{VIS} at the photon energy (2.33 eV) of the VIS laser, which is far from the photodetachment threshold (≈ 0.49 eV). In order to further corroborate the experiment, we estimate σ_1^{VIS} from the given experimental data. Because, to the best of our knowledge, no literature values are available for σ_1^{VIS}, we resort to comparing our estimated value to the literature cross sections of other small hydrocarbon anions.

The VIS laser depletion rate depends linearly on the luminosity (equation 4.3) and thus on the VIS pulse energy in the ion-photon interaction region (equation 4.21):

$$k_1^{\mathrm{VIS}} = \sigma_1^{\mathrm{VIS}} r^{\mathrm{VIS}} L^{\mathrm{VIS}} \tag{4.72}$$

$$= \sigma_1^{\mathrm{VIS}} r^{\mathrm{VIS}} \frac{E^{\mathrm{VIS}}}{l_{\mathrm{max}} C_{\mathrm{CSR}} E_\gamma^{\mathrm{VIS}}} \tag{4.73}$$

We rearrange for the photodetachment cross section yields and identify the factor $k_1^{\mathrm{VIS}}/E^{\mathrm{VIS}}$ with the slope $S^{\mathrm{VIS}} \approx 7.9 \times 10^{-2}(Js)^{-1}$ of the linear fit to the VIS laser data set (black dots) in figure 4.13:

$$\sigma_1^{\mathrm{VIS}} = \frac{k_1^{\mathrm{VIS}}}{E^{\mathrm{VIS}}} \frac{E_\gamma^{\mathrm{VIS}} l_{\mathrm{max}} C_{\mathrm{CSR}}}{r^{\mathrm{VIS}}} \tag{4.74}$$

$$= S^{\mathrm{VIS}} \frac{E_\gamma^{\mathrm{VIS}} l_{\mathrm{max}} C_{\mathrm{CSR}}}{r^{\mathrm{VIS}}}. \tag{4.75}$$

For $E_\gamma^{\mathrm{VIS}} = 2.33$ eV, $l_{\mathrm{max}} = 1$ cm, $C_{\mathrm{CSR}} = 35.12$ m and $r^{\mathrm{VIS}} = 10$ Hz, we obtain a $\mathrm{H_2CC^-}$ photodetachment cross section of

$$\sigma_1^{\mathrm{VIS}} = 1.04(\pm 0.44)_{\mathrm{stat}}(^{+1.04}_{-0.52})_{\mathrm{sys}} \times 10^{-17}\ \mathrm{cm}^2. \tag{4.76}$$

Here, the statistical uncertainty purely results from the linear fit, which only uses the statistical uncertainties (vertical error bars) of the data points. The systematic uncertainty results from multiple contributions: As the detailed geometry of the ion-photon interaction region is not known, we assume l_{max} to be only accurate by a factor of 2. Since now the absolute value of E^{VIS} is relevant, we include the systematic uncertainty of the transmission factor T_{VIS} from the ion photon interaction region to the location where E^{VIS} is measured (see appendix table B.1). Furthermore we incorporate the scattering and drift of the VIS laser energies, i.e., the horizontal error bars in figure 4.13 were incorporated, as well as alternative thresholds (analogue to section 4.4.1) of the pulse-height cuts on the detector noise.

Compared to the photodetachment cross sections of the other ion beam components (table 4.1 in section 4.3.3.2), the estimate for the photodetachment cross section of $\mathrm{H_2CC^-}$ appears to be on the same order of magnitude. The photon energy of the VIS laser lies about 1.8 eV higher than the $\mathrm{H_2CC^-}$ photodetachment threshold (EA $\approx$ 0.49 eV). We can compare this value to the total photodetachment cross sections of the hydrocarbon anions $\mathrm{C_2H^-}$ and $\mathrm{C_4H^-}$ calculated by Douguet, Kokoouline, and Orel 2014: About 1.8 eV above their respective photodetachment thresholds, the photodetachment cross section of both molecules is about 10^{-17} cm^2, which agrees well with the estimated photodetachment cross section of $\mathrm{H_2CC^-}$.

4.5 Discussion and theory

Using the radiatively cold ($\sim$ 10 K) environment of the CSR we observed an effective lifetime on the order of $\tau^{\text{eff}} \gtrsim 10^4$ s for the electronic and vibrational ground state of the vinylidene anion H_2CC^-. This value is about a factor $C_{10}^{300} \gtrsim 100$ larger than the lifetime measured by the 300 K storage ring experiment of Jensen, Pedersen, and Andersen 2000. Here, we discuss the possible origin of this discrepancy and suggest further experimental measures.

We first follow the idea of Jensen, Pedersen, and Andersen 2000 about the reaction pathway limiting the intrinsic lifetime of the vinylidene anion. As depicted in figure 2.1 in section 2.1, the vibrational ground state H_2CC^- is stabilized against isomerization by a ≈ 0.5 eV barrier, but lies energetically above the neutral acetylene. This gives rise to the mentioned assumption about a tunneling process to the neutral vinylidene configuration together with electron detachment. Our experimental result clearly shows that the rate of such a process from the vibrational ground state of H_2CC^-, which is practically the only level populated under our cryogenic conditions, cannot explain the result of this earlier study. However, apart from the H_2CC^- vibrational ground state, a few higher excited vibrational states, metastable against isomerization as well, have more shallow barriers for this process. Given the smallest harmonic vibrational frequencies of H_2CC^- (down to $\approx 765\ \text{cm}^{-1}$, see table 2.1 in section 2.1) and the 300 K thermal energy $k_B T/hc = 209\ \text{cm}^{-1}$ we expect small but non-negligible populations for these excited vibrational states. Hence, they are relevant for the tunneling as well. We assume that, for each vibrational level ν, the tunneling probability P_ν is given by the square of the vibrational wave function tail in the barrier. Multiplication with the thermal population B_ν^T given by the Boltzmann distribution yield the absolute loss rates $r_\nu^T = P_\nu B_\nu^T$ due to tunneling at temperature T. The absolute tunneling rate at 300 K is then the sum of all individual rates r_ν^T:

$$R^{300\ \text{K}} = \sum_{\nu=0}^{\infty} P_\nu B_\nu^{300\ \text{K}} \tag{4.77}$$

For the strongly suppressed thermal radiation field of the CSR, we expect close to one hundred percent of the vibrational ground state to be populated:

$$R^{10\ \text{K}} \approx \sum_{\nu=0}^{\infty} P_\nu B_\nu^{10\ \text{K}} \tag{4.78}$$

To explain the factor $C_{10}^{300} \gtrsim 100$ between the two measured lifetimes, the ratio $R^{300\ \text{K}}/R^{10\ \text{K}}$ would have to be at least on the order of this factor. At the same time, the absolute rates would still have to be on the order of the H_2CC^- decay rates measured at room-temperature.

We estimated the wave function parameters (and hence P_ν in equations 4.77–4.78) with the help of our collaborator Evangelos Miliordos from Auburn University (Alabama, USA). By means of quantum chemical calculations, he determined the one-dimensional potential energy surfaces of the neutral and anionic acetylene-vinylidene system for the in-plane motion of a hydrogen atom, as well as for the hydrogen out-of-plane motion (Miliordos 2023). These isomerization coordinates approximately correspond to the normal vibrational CH_2 rocking mode (ν_6, see Guo et al. 2015) and the out-of-plane normal vibrational mode (ν_4) of H_2CC^-. We consider coordinate excursions from equilibrium in a range where the anionic electronic potential lies above the neutral one, such that electron emission and subsequent rapid isomerization would become possible. For both isomerization coordinates, we extract the vibrational wave function parameters and determine the absolute loss rates due to tunneling from equations 4.77–4.78, as well as their ratio $R^{300\text{ K}}/R^{10\text{ K}}$. In each case we either end up in a situation with a ratio on the required order of magnitude ($\gtrsim 100$) but absolute rates too low by orders of magnitude, or a situation where the opposite is the case, i.e., realistic absolute rates but a by far too low ratio. It is to be noted here that compared to the ν_6 isomerization coordinate, along the ν_4 isomerization coordinate the rate ratio seems to rise much more quickly. Taken these estimates, we conclude that, even for the 300 K conditions of Jensen, Pedersen, and Andersen 2000, a tunneling process involving isomerization either via the CH_2 rocking mode or the out-of-plane mode is unlikely to play a role for spontaneous electron loss of H_2CC^-.

In their experiment, Jensen, Pedersen, and Andersen 2000 estimated the rate due to non-resonant photodetachment by blackbody photons to be $r_b < 10^{-3}\text{ s}^{-1}$, which is negligible compared to their measured H_2CC^- decay rate $k_0 = (9 \pm 6) \times 10^{-3}$. However, they did not elaborate how they conducted their estimate. We presume that they determined this rate by assuming a photodetachment cross section σ and using the spectral photon flux Φ given by the Planck radiation law (Planck 1901):

$$r_b = \int_{\tilde{\nu}_0}^{\infty} \sigma(\tilde{\nu})\Phi(\tilde{\nu})\ \mathrm{d}\tilde{\nu} \tag{4.79}$$

$$= \int_{\tilde{\nu}_0}^{\infty} \sigma(\tilde{\nu}) \frac{8\pi c\tilde{\nu}^2}{e^{hc\tilde{\nu}/k_B T} - 1}\, \mathrm{d}\tilde{\nu} \tag{4.80}$$

For a more practical treatment in the following, we formulated equations 4.79–4.80 in the wavenumber scale. Here, $\tilde{\nu}_0$ is the ground state H_2CC^- photodetachment threshold.

Since in section 4.4.3 we measured the H_2CC^- photodetachment cross section far from the detachment threshold ($\tilde{\nu}^{\text{VIS}} = E^{\text{VIS}}/hc = 18797\text{ cm}^{-1}$), we indeed now have, at least for this energy, experimental information at hand about the absolute photodetachment cross section, which we can try to use for re-estimating the rate r_b. To this end, we model the shape of the H_2CC^- photodetachment cross section $\sigma(\tilde{\nu})$ as in Meyer et al. 2017 using

$$\sigma(\tilde{\nu}) = C(\tilde{\nu} - \tilde{\nu}_0)^a\ \tilde{\nu}^{b-a}, \tag{4.81}$$

where $\tilde{\nu}$ is the wavenumber of the impinging photons, $\tilde{\nu}_0 = \text{EA}_v/hc = 3925\text{ cm}^{-1}$(DeVine et al. 2017) is the detachment threshold, and a and b are modeling parameters for the

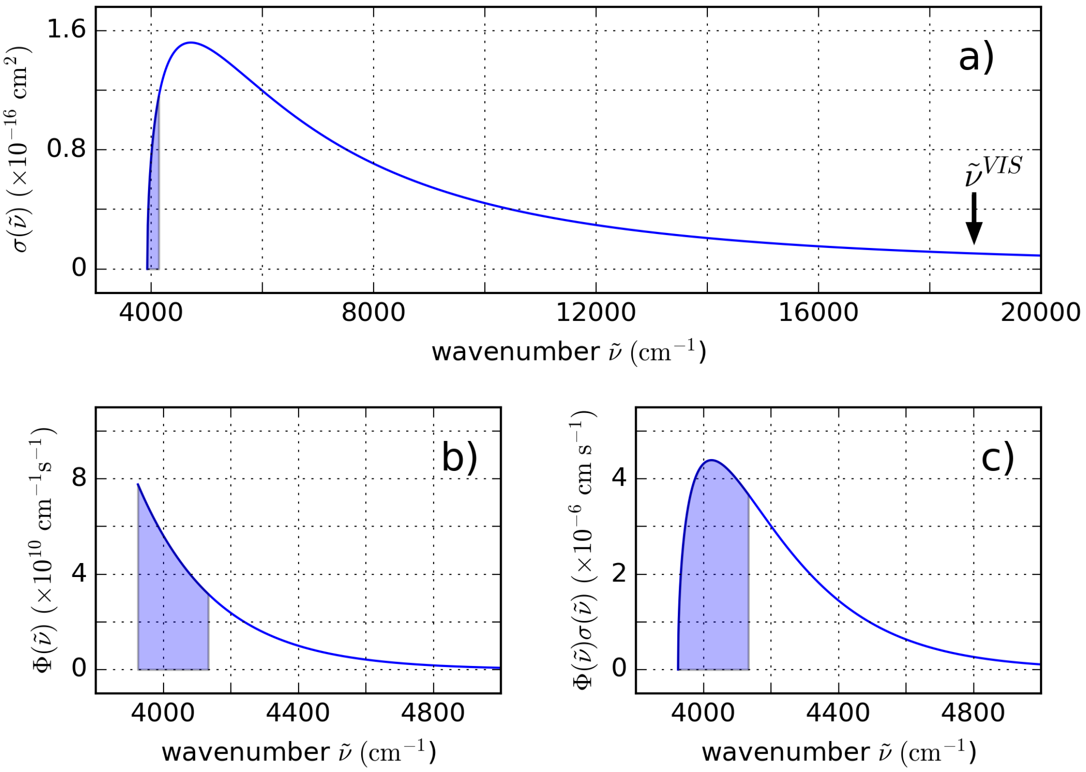

Figure 4.14: a) Non-resonant photodetachment cross section model of H_2CC^-. The black arrow indicates the wavenumber of the VIS laser $\tilde{\nu}^{\text{VIS}} = 18797$ cm^{-1}. b) Room-temperature blackbody photon flux. c) Product of a) and b). The blue shaded area in all plots is a thermal ($T = 300$ K) window of width $k_BT/hc = 209$ cm^{-1}. It commences at the H_2CC^- photodetachment threshold $\text{EA}_v/hc = 3925$ cm^{-1}.

cross section slopes. All constant factors used in Meyer et al. 2017 are contained in the amplitude C. The cross section model is depicted in figure 4.14 a) using parameter values $a = 0.5$ and $b = -2.5$. The amplitude $C = \sigma(\tilde{\nu}^{\text{VIS}}) \times (\tilde{\nu}^{\text{VIS}} - \tilde{\nu}_0)^{-a} \times (\tilde{\nu}^{\text{VIS}})^{a-b}$ results from insertion of the VIS laser wavenumber $\tilde{\nu}^{\text{VIS}}$ and the corresponding measured cross section value (equation 4.76) into equation 4.81. Above the detachment threshold $\tilde{\nu}_0$ the modeled cross section rises sharply. It culminates at a value of about 1.5×10^{-16} cm^2 and decreases monotonically. The black arrow at the far end of the model indicates our measured far-from-threshold cross section, which scales the model amplitude by means of C.

In a next step, we determine the 300 K spectral photon flux $\Phi(\tilde{\nu})$ as given in equation 4.80 and plotted in figure 4.14 b). In the figure, the blue shaded area is a thermal window, which (in all sub-figures) starts at the H_2CC^- photodetachment threshold $\tilde{\nu}_0$ and has a width of $k_BT/hc = 209$ cm^{-1}. The product $\sigma(\tilde{\nu})\Phi(\tilde{\nu})$ of the modeled cross section and the spectral photon flux is depicted in figure 4.14 c). According to equation 4.80 the total area below the curve corresponds to the total blackbody photodetachment rate. The window defined by the interval of size $k_B T/hc$ accounts for about 45% of this rate. For the *total* blackbody photodetachment rate we obtain a value

$$r'_b = 1.8(\pm 0.8)_{\mathrm{stat}}(^{+1.8}_{-0.9})_{\mathrm{sys}} \times 10^{-3}\ \mathrm{s}^{-1}. \tag{4.82}$$

The uncertainties are propagated from the uncertainties of the cross section $\sigma(\tilde{\nu}^{\mathrm{VIS}})$ from equation 4.76. The estimated rate r'_b is almost two times larger than the upper limit of r_b (10^{-3} s) estimated by the room-temperature study. This leads us to believe that, for their estimate, Jensen, Pedersen, and Andersen 2000 assumed a maximum photodetachment cross section of $< 10^{-16}$ cm^2. Even though a cross section on this order of magnitude is already rather large, this value might still be underestimated for the case of H_2CC^-. Within the given uncertainties, r'_b agrees with the measured room-temperature H_2CC^- decay rate $k_0 = (9 \pm 6) \times 10^{-3}$ s^{-1}. From the viewpoint of this estimate, it is thus not excluded that the measured room-temperature H_2CC^- lifetime results from non-resonant detachment by 300 K blackbody photons.

Another reaction pathway from H_2CC^- to the linear HCCH may be autodetachment after vibrational excitation by means of infrared photons, as observed by DeVine et al. 2018; Gerardi et al. 2010 and simulated by Issler, Mitrić, and Petersen 2023. In view of these studies, we estimated if the measured room-temperature H_2CC^- decay rate k_0 may alternatively be explained with *resonant* photodetachment after vibrational excitation by blackbody photons. Here, we considered the level density of all six vibrational modes of H_2CC^- above the photodetachment threshold (Hansen 2013) and the Planck radiation law at room temperature. If we take into account the uncertainty of k_0, each resonance would have to have a cross section of $> 10^{-15}$ cm^2. This value is too large to be realistic for vibrational excitation. Hence, resonant photodetachment above threshold seems to be an unlikely explanation for the decay rate of H_2CC^- measured at room temperature.

To give a short intermediate résumé: Among our explanation approaches, which comprise tunneling in combination with isomerization and electron loss, as well as resonant and non-resonant photodetachment, we estimated non-resonant photodetachment by blackbody photons to be the most likely explanation for the factor $C^{300}_{10} \gtrsim 100$ discrepancy between the ground state H_2CC^- lifetimes measured with the room-temperature storage ring of Jensen, Pedersen, and Andersen 2000 and the cryogenic storage ring CSR. As our explanation approaches either have rather large uncertainties or a mostly speculative character, we propose further steps to shed light on this discrepancy:

- In our experiment the uncertainty was dominated by the low statistics of the H_2CC^- photodetachment signal. To reduce this uncertainty, we suggest to find an ion source with significantly higher H_2CC^- output.
- If the absolute H_2CC^- photodetachment signal then allows for it, the power of the probing laser (VIS) may be lowered, thereby reducing depletion effects due

to the laser probing. Using a VIS laser with better long-time stability would be advisable as well. Apart from reduced systematic uncertainties of the lifetime measurement these measures will also allow to determine the photodetachment cross section more precisely. Furthermore, while we find it intriguing that we were able to model the absolute H_2CC^- cross section by means of a cross section value measured during our very experiment, we would welcome complementary absolute H_2CC^- photodetachment cross section values determined by experiments dedicated to such measurements.

- In order to better estimate the effect of Collisional Electron Detachment (CED) we propose to either vary the pressure in the CSR or the ion beam kinetic energy. According to equation 4.2 in section 4.2.3 we expect both measures to have a similar effect on the CED-induced loss rate. Complementary to this approach it would be helpful if other experiments specialized on measuring CED cross sections would provide more detailed information on the absolute CED cross sections of H_2CC^- and CN^-, especially within the kinetic energy range of the CSR and for the target gas H_2, which is the most-abundant residual gas component under cryogenic vacuum conditions.
- While in their study, DeVine et al. 2017 found coupling of neutral vinylidene to neutral acetylene via the CH_2 rocking mode (ν_6), they did not observe this for deuterated vinylidene D_2CC^-. H_2CC may thus more readily isomerize to HCCH than its deuterated version. To shed more light on whether isomerization does, after all, influence the results, it would be interesting to repeat the storage ring lifetime experiment at *room temperature* with both H_2CC^- and deuterated vinylidene D_2CC^-. Observation of the same lifetime for both ion species would yield a further indication that non-resonant photodetachment by blackbody radiation affects the H_2CC^- lifetime.
- From the viewpoint of theory, it may be interesting to use the new approaches outlined by Issler, Mitrić, and Petersen 2023 for deriving a combined probability for anionic vibrational excitation and the following autodetachment, especially considering photoexcitation from lower-lying anionic states in a blackbody radiation field. This may explain the difference of the Aarhus experiment (Jensen, Pedersen, and Andersen 2000) in a 300 K blackbody field and of the CSR experiment at a radiation field of much lower temperature.

In conclusion, using the low radiative environment of the CSR we measured the lifetime for H_2CC^- in its vibrational and electronic ground state to be two orders of magnitude higher than the lifetime determined by a room-temperature storage ring study of Jensen, Pedersen, and Andersen 2000. We speculated about the origin of this discrepancy and found that, other than estimated by Jensen, Pedersen, and Andersen 2000, non-resonant photodetachment by room-temperature blackbody radiation seems to be the most likely explanation. From the viewpoint of our estimates, isomerization in connection with electron detachment does not seem to play a role here. With regard to future H_2CC^- studies, our suggestions comprise enhancements of our own experiment, requests for additional absolute cross section data from dedicated experiments, and usage of newly developed theoretical approaches (Issler, Mitrić, and Petersen 2023) related to the reaction pathway between H_2CC^- and the neutral HCCH.

Chapter 5

Conclusion and outlook

The conditions provided by ion storage rings allow to study anions in their ground or excited states over long times. Using the electrostatic cryogenic storage ring CSR, we addressed the stability of the vinylidene anion H_2CC^- in this thesis. Energetically, H_2CC^- lies above the neutral state of the acetylene anion which has the same elemental composition. The time scale by which vinylidene reaches this lowest neutral state is unknown, although it may be very long. In view of previous results suggesting a finite lifetime of the order of 100 s, we have studied at the CSR the stability of this ion species on a timescale which is by factor of ~ 100 longer.

The low residual gas density and hence the almost collision-free environment of cryogenic storage rings, which leads to ion beam lifetimes on the order of ~ 1 h, allows to observe the decay of such metastable ions. As already shown by Jensen, Pedersen, and Andersen 2000, this experimentally explored time can be extended by quantifying the external loss mechanisms using a reference anion stable against spontaneous electron loss. This trick expands the experimentally explored timescale by about an order of magnitude, which means up to ~ 10 h for cryogenic storage rings. Among ion storage devices, such long timescales are only surpassed by cryogenic Penning trap experiments, which, due to their even lower residual gas densities and more confined trapping potentials, manage to trap a single ion for days (Eliseev and Novikov 2023) or even months (Heiße et al. 2019). However, storage rings are the better choice with respect to stability experiments on ensembles of anions. Compared to ion ensembles confined to $\lesssim 1$ cm trap dimensions, ensembles stored as dilute ~ 1 cm diameter beams on closed orbits of up to ~ 10 m are less affected by space charge effects. Also, compared to ion trapping almost at rest, storage at high velocity effectively decouples ions from the residual gas, which helps to better isolate collision-related loss processes.

In our studies, we also addressed the situation that anions are sometimes difficult to produce, so that experiments have to get along with comparably few ions. Photodetachment experiments using cryogenic storage rings can handle low ion numbers well, as such devices only have low collisional background in the signals of their single-particle detectors collecting the neutral photodetachment products. In addition, the detector background can be suppressed by techniques related to the detector signal analysis and the ion beam probing scheme, e.g., pulsed-laser photodetachment. Using these techniques for the H_2CC^- stability study conducted within this thesis, we were able to work with only few thousand ions of H_2CC^- at a time. This is so far the lowest number of a single ion species studied at the CSR by means of photodetachment. Other (non-photodetachment) anion stability studies conducted with storage rings, e.g., experiments on dianions, even manage to cope with down to a single ion per experimental cycle (Najeeb et al. 2023). To statistically track the ion decay over many experimental cycles in this case, ions are extracted from the closed ring orbit and directly dumped on a counting detector at various times with respect to the starting time of the experimental cycle (Gatchell et al. 2021; Najeeb et al. 2023). Comparable detection schemes are also envisaged for the CSR.

Ion sources are complex chemical reactors used to produce beams of gas-phase ions from solid, liquid or gaseous samples. Even seemingly insignificant changes or the same ion production settings may lead to a completely different outcome with respect to the ion beam composition or the initial state populations. Sensitive and high-resolution diagnostic methods are thus required to track down the origin of such changes. Once the ion beam composition is under control, it should be verified repeatedly during experiments. This is also relevant for anion stability studies, where the desired anion or a specific anionic excited state is sometimes difficult to produce (Müll et al. 2021). High-resolution ToF mass spectrometry (Plaß, Dickel, and Scheidenberger 2013), which has recently also been incorporated into electrostatic storage ring technology (Grieser et al. 2022), significantly facilitates such tasks. As demonstrated in this thesis for the case of the CSR operated as an ISO-ToF mass spectrometer (Grieser et al. 2022), such techniques can also be augmented to determine the precise relative fractions of isobaric ion species in a stored ion beam, and to identify the contribution of excited states of isobaric anions to photodetachment signals. In addition to diagnostics, techniques for actively removing unwanted ion beam components in electrostatic storage rings are currently in development.

In room-temperature storage ring experiments, anions with a weakly bound electron ($\sim$ 10 meV) are photodetached by almost the entire spectral range of the thermal ($k_B T \approx 26$ meV) blackbody field. Under these conditions such anions are short-lived and therefore hard to study. In order to suppress the 300 K thermal field and to stabilize anion with a weakly bound electron against detachment by thermal photons, storage rings are cooled (Pedersen et al. 2001). Even though some anions with a higher detachment threshold ($\gtrsim 0.5$ eV) appear to be mostly stable against room-temperature blackbody photodetachment, they may still have a rather large photodetachment cross section. Of the total blackbody spectrum, only the very small fraction above threshold is then sufficient for introducing a very low photodetachment decay rate. Storage rings are sensitive to such low rates, as shown by Jensen, Pedersen, and Andersen 2000 and also within this thesis.

To conclude, this thesis has once again demonstrated that electrostatic storage rings, especially when operated under cryogenic conditions, are well suited for studying the stability of gas-phase negative ions. Furthermore, the developments made within this thesis further augment the possibilities of such studies.

Appendix A

Supplementary information on the experimental developments

Here we give supplementary information on various topics of chapter 3. In section A.1 we show a detailed view of the laser setup located in the second linear section of the CSR. Section A.2 presents the technical modification and calibration of the ISTB detector system made for characterizing the output of low-intensity ion sources. Section A.3 is about the ion-optical simulation of the electrostatic branch beamline on the 300 kV ion source platform. In section A.4 we give additional technical information about the LVAP ion source and discuss cationic mass spectra measured with the LVAP ion source mounted at the ISTB.

A.1 Detailed technical view of the CSR laser setup

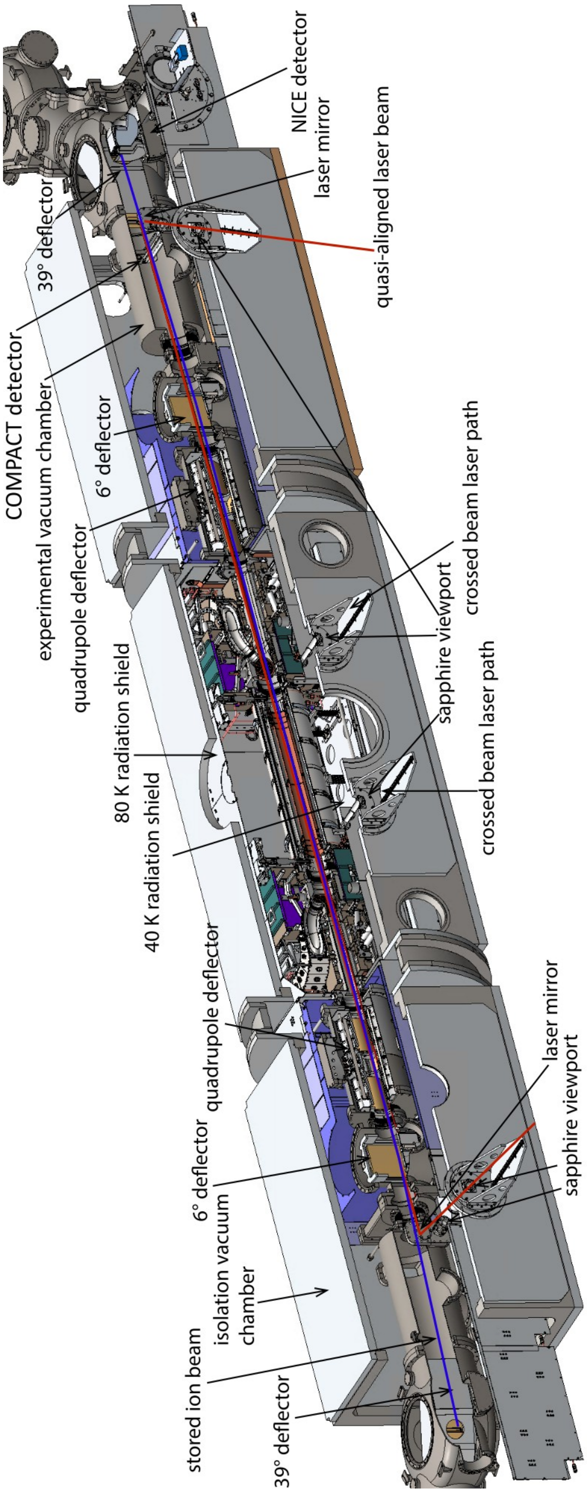

Figure A.1: Technical view of the CSR laser setup. Figure adapted from Müll 2023.

A.2 Sensitivity gap between particle counting and ion current measurement

Here we describe the technical modification made (section A.2.1) and the calibration procedure carried out (section A.2.2) for bridging the sensitivity gap (section 3.2.1.3) of the diagnostics 2 detector unit of the ion source test bench (see figure 3.3).

A.2.1 Technical modification of the channeltron circuit

Figure A.2 a) depicts the electrical circuit of the channeltron. As described in Nüsslein 2018, particles impinge at the Faraday cup and are converted into electrons. The electrons are sucked in by the channeltron and converted into a voltage signal U_{sig} digestible by a voltage probe. A central element here is the high pass filter composed of R_0 and C (Suits 2023). Compared to the counting mode circuit used in Nüsslein 2018, $R_0 = 1\ \mathrm{M\Omega}$ (before $50\ \Omega$) was changed. All other circuit elements are unchanged. The timescale

$$\tau_{\mathrm{C}} = R_0 C \tag{A.1}$$

determining the integration timescale of the incoming signal thus increases drastically to $\tau_C = 1$ ms (before 50 ns).

Instead of counting single particles at a high input voltage U_{in}, entire ion pulses with a duration on the order of µs can now be registered at a lower input voltage U_{in}. Note that the effective gain voltage U_{ch} dropping at the channeltron (R_{ch}) is about 58.5% of U_{in} (Nüsslein 2018).

A.2.2 Calibration

By means of the time traces in figure 3.4, we now explain the idea of the calibration procedure. The time traces visualize the time-dependent ion current $I(t)$ and thus the shape of the ion pulse in time t. The number of ions in a pulse

$$N_q = \frac{1}{q} \int I(t)\,\mathrm{d}t \tag{A.2}$$

is then given by the time integral over the relevant part of the time trace and the charge q of the individual charge carriers within the pulse. Here, we assume singly charged particles carrying the elementary charge $q = e$. With the Faraday cup and an amperemeter $I(t)$ can be determined easily. In the case of the channeltron, we can only measure the time trace of the signal voltage

$$U_{\mathrm{sig}}(t) = C_{\mathrm{ch}} G(U_{\mathrm{in}}) I(t), \tag{A.3}$$

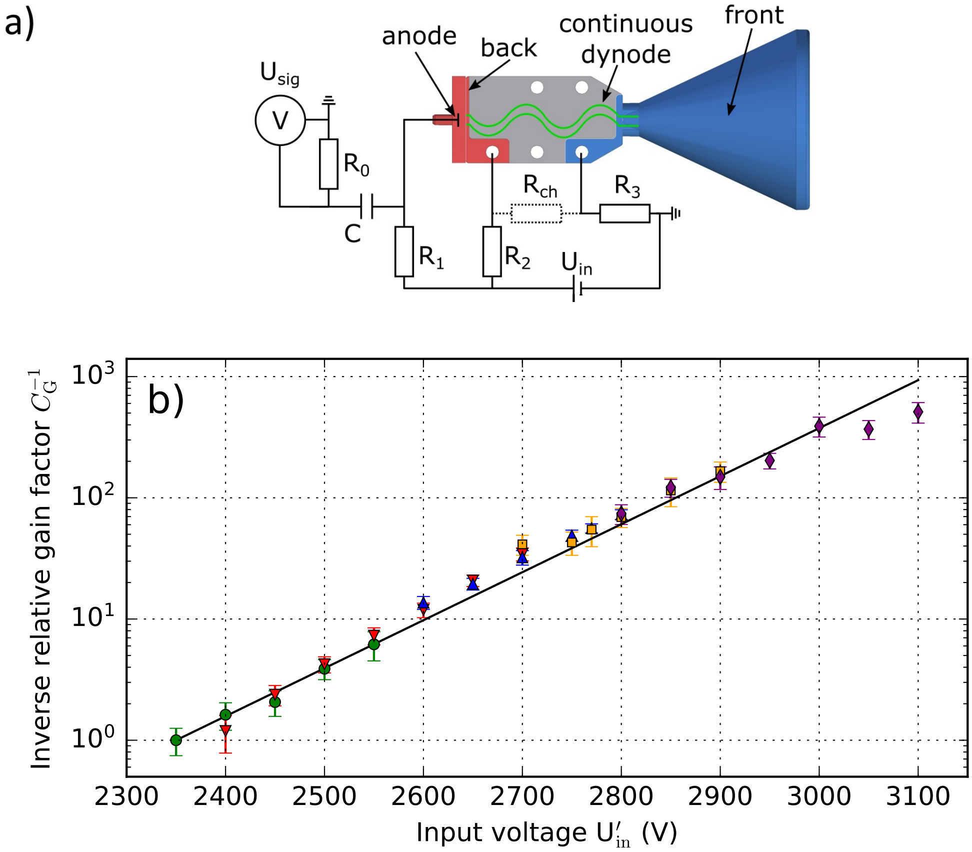

Figure A.2: a) Channeltron electrical circuit (figure taken from Nüsslein 2018) for the channeltron current amplifier mode. The values of the circuit elements are $C = 1$ nF, $R_1 = 1$ MΩ, $R_2 = 2$ MΩ, $R_3 = 50$ MΩ, $R_{\mathrm{ch}} = (73.28 \pm 0.10)$ MΩ. b) Inverse relative gain factor C_{G}^{-1} plotted against the channeltron input voltage U'_{in}. The data points were taken for different input voltages U'_{in} using C_{10}^{-} (green circles), C_{11}^{-} (red downward-facing triangles), C_{9}^{-} (blue upward-facing triangles) and C_{4}^{-} (orange squares and purple diamonds). The solid line is a single-exponential fit to all data points and forced to match with the first data point at 2350 V.

which we assume to be related to the ion current $I(t)$ via an unknown conversion factor C_{ch} from voltage to current and the absolute gain factor $G(U_{\mathrm{in}})$. The latter factor represents the amplification by means of the channeltron and depends on the input voltage U_{in}. The time integral over the relevant part of the voltage time trace is then proportional to the number of ions in the pulse:

$$\int U_{\mathrm{sig}}(t)\,\mathrm{d}t = C_{\mathrm{ch}} G(U_{\mathrm{in}}) \int I(t)\,\mathrm{d}t \tag{A.4}$$

The calibration procedure is based on these two quantities: For a current $I(t)$ high enough to be detectable by the Faraday cup and low enough not to damage the channeltron we measure both N_q and $U_{\mathrm{sig}}(t)$. To detect ion pulses with lower ion currents $I'(t)$ and thus lower ion numbers $N'_q = \frac{1}{q} \int I'(t)\,\mathrm{d}t$, we use a higher absolute gain factor

$G(U'_{\mathrm{in}})$. The resulting integrated signal voltage is then:

$$\int U'_{\mathrm{sig}}(t)\,\mathrm{d}t = C_{\mathrm{ch}} G(U'_{\mathrm{in}}) \int I'(t)\,\mathrm{d}t. \tag{A.5}$$

As we have the absolute ion number N_q from the Faraday cup measurement, we establish a connection to N'_q by taking the ratio

$$N_q \frac{\int U'_{\mathrm{sig}}(t)\,\mathrm{d}t}{\int U_{\mathrm{sig}}(t)\,\mathrm{d}t} = N_q \frac{G(U'_{\mathrm{in}}) \int I'(t)\,\mathrm{d}t}{G(U_{\mathrm{in}}) \int I(t)\,\mathrm{d}t} \tag{A.6}$$

$$= N_q \frac{G(U'_{\mathrm{in}})\, \overbrace{q^{-1} \int I'(t)\,\mathrm{d}t}^{N'_q}}{G(U_{\mathrm{in}})\, \underbrace{q^{-1} \int I(t)\,\mathrm{d}t}_{N_q}} \tag{A.7}$$

$$= N'_q \frac{G(U'_{\mathrm{in}})}{G(U_{\mathrm{in}})} \tag{A.8}$$

In the second equation we expanded the fracture by q^{-1}. Rearranging for N'_q then yields:

$$N'_q = \overbrace{\frac{G(U_{\mathrm{in}})}{G(U'_{\mathrm{in}})}}^{C_{\mathrm{G}}} \overbrace{\frac{N_q}{\int U_{\mathrm{sig}}(t)\,\mathrm{d}t}}^{C_q} \int U'_{\mathrm{sig}}(t)\,\mathrm{d}t \tag{A.9}$$

$$= C_{\mathrm{G}} C_q \int U'_{\mathrm{sig}}(t)\,\mathrm{d}t \tag{A.10}$$

Both the calibration factor C_q and the relative gain factor C_{G} can be determined experimentally. To this end, we use the LVAP ion source (see section 3.2.3) equipped with a graphite target for producing carbon-based ion species in a wide range of masses and intensities, as in the mass spectrum in figure 3.15. We set the horizontal and vertical opening of slits 1 and 2 of the ion source test bench such that the highest peak in the mass spectrum (C_{10}^-) reduces to about 0.5 nA peak current. This ion current lies within the sensitivity range of both Faraday cup and channeltron for $U_{\mathrm{in}} = 2350$ V. We measure 32 samples each for N_q and $\int U_{\mathrm{sig}}(t)\,\mathrm{d}t$ and obtain for the calibration factor:

$$C_q = \frac{N_q}{\int U_{\mathrm{sig}}(t)\,\mathrm{d}t} = (6.1 \pm 0.5) \times 10^{11}\ \mathrm{V}^{-1}\mathrm{s}^{-1}. \tag{A.11}$$

The uncertainty is propagated from the standard error of the mean of N_q and $\int U_{\mathrm{sig}}(t)\,\mathrm{d}t$.

The relative gain factor C_{g} is obtained by measuring $\int U'_{\mathrm{sig}}(t)\,\mathrm{d}t$ and, for constant parameters except for G, comparing it to the signal $\int U_{\mathrm{in}}$ obtained for $U_{\mathrm{in}} = 2350$ V:

$$\frac{\int U'_{\mathrm{sig}}(t)\,\mathrm{d}t}{\int U_{\mathrm{sig}}(t)\,\mathrm{d}t} = \frac{G(U'_{\mathrm{in}}) \int I'(t)\,\mathrm{d}t}{G(U_{\mathrm{in}}) \int I(t)\,\mathrm{d}t} \tag{A.12}$$

$$= \frac{G(U'_{\mathrm{in}})}{G(U_{\mathrm{in}})} = C_{\mathrm{G}}^{-1} \tag{A.13}$$

The inverse relative gain factor C_{G}^{-1} is plotted in figure A.2 b) against the input voltage U'_{in}. Each data point is the mean of 32 samples both of $\int U_{\mathrm{sig}}(t)\,\mathrm{d}t$ and $\int U'_{\mathrm{sig}}(t)\,\mathrm{d}t$. For $\int U_{\mathrm{sig}}(t)\,\mathrm{d}t$ we always use the same data set obtained at $U_{\mathrm{in}} = 2350$ V. The error bars are then propagated from the 1σ uncertainty of $\int U_{\mathrm{sig}}(t)\,\mathrm{d}t$ and $\int U'_{\mathrm{sig}}(t)\,\mathrm{d}t$.

If the amplification becomes too high (peak signal > 40 mV), we switch to peaks in the mass spectrum with lower ion intensity. We record dedicated data sets of $\int U'_{\mathrm{sig}}(t)\,\mathrm{d}t$ with C_{11}^-, C_9^- and C_4^-. The data sets are indicated by different markers in figure A.2 b). An overlap in U'_{in} between the data sets ensures their compatibility. In order to stitch two overlapping data sets together we use the ratio of all overlapping points.

As the inverse relative gain factor exhibits an exponential trend, we fit a single exponential function

$$f_{\mathrm{G}}(U'_{\mathrm{in}}) = \exp[A(U'_{\mathrm{in}} - U_0)] \tag{A.14}$$

to all data points (black line), where we force $U_0 = 2350$ V. The fit yields

$$A = (9.11995 \pm 1.2) \times 10^{-3}\ \mathrm{V}^{-1} \tag{A.15}$$

with a negligible uncertainty. Instead of propagating it to the statistical uncertainty of $f_{\mathrm{G}}(U'_{\mathrm{in}})$, it is more realistic to take the statistical uncertainty of the first data point:

$$\left(\frac{\Delta f_{\mathrm{G}}(U'_{\mathrm{in}})}{f_{\mathrm{G}}(U'_{\mathrm{in}})}\right)_{\mathrm{stat}} = \frac{\Delta C_{\mathrm{G}}^{-1}}{C_{\mathrm{G}}^{-1}} \approx 25\ \% \tag{A.16}$$

For the highest voltages U'_{in} the data points deviate strongly from the exponential trend. On average, the systematic deviation of the data points from the curve is:

$$\left(\frac{\Delta f_{\mathrm{G}}(U'_{\mathrm{in}})}{f_{\mathrm{G}}(U'_{\mathrm{in}})}\right)_{\mathrm{sys}} = \pm 21\ \% \tag{A.17}$$

It is maximum $+70\%$ and minimum -45%.

As the exponential fit (equation A.14) enables us to estimate the number of particles more easily than with the discrete measurement points, we use the following conversion from the signal voltage U'_{sig} to the number of particles N'_q based on equation A.10:

$$N'_q(U'_{\mathrm{in}}) = \frac{C_q}{f_{\mathrm{G}}(U'_{\mathrm{in}})} \int U'_{\mathrm{sig}}(t)\,\mathrm{d}t \tag{A.18}$$

$$= C_q e^{-A(U'_{\mathrm{in}} - U_0)} \int U'_{\mathrm{sig}}(t)\,\mathrm{d}t \tag{A.19}$$

A.3 Ion-optical simulation for the electrostatic branch of the 300 kV ion source platform

Here we summarize the relevant results of the simulations for the electrostatic branch beamline of the CSR 300 kV ion source platform (see section 3.2.2), which were carried out by P. M. Mishra and M. Grieser (Grieser 2019; Mishra et al. 2018; Mishra 2019).

The electrical fields of the 90° electrostatic deflectors and the quadrupole triplets were calculated with TOSCA (Opera3D) (Vector Fields 2004). The resulting electrical field maps were used as input for G4beamline (Roberts 2013), which was employed for simulating the path of the ion beam through the beamline, as depicted in figure A.3. The simulation does not include the ion-optical elements upstream of the first 90° electrostatic deflector CD 1 (see figure 3.6 b)). For the G4beamline simulation, the following initial ion beam parameters were assumed:

- Particle number, species and kinetic energy: 10^4 protons with 5.1 keV
- Gaussian beam profile
- Horizontal (x) and vertical (z) phase space: $\sigma_x = 1.67$ mm, $\sigma_{x'} = 6$ mrad, $\sigma_z = 1.67$ mm, $\sigma_{z'} = 6$ mrad, no additional angle of the phase space ellipses
- Resulting from the phase space, the horizontal and vertical 2σ emittances are $\epsilon_{2\sigma,x} = 4\sigma_x\sigma_{x'} \approx 40$ mm·mrad and $\epsilon_{2\sigma,z} = 4\sigma_z\sigma_{z'} \approx 40$ mm·mrad

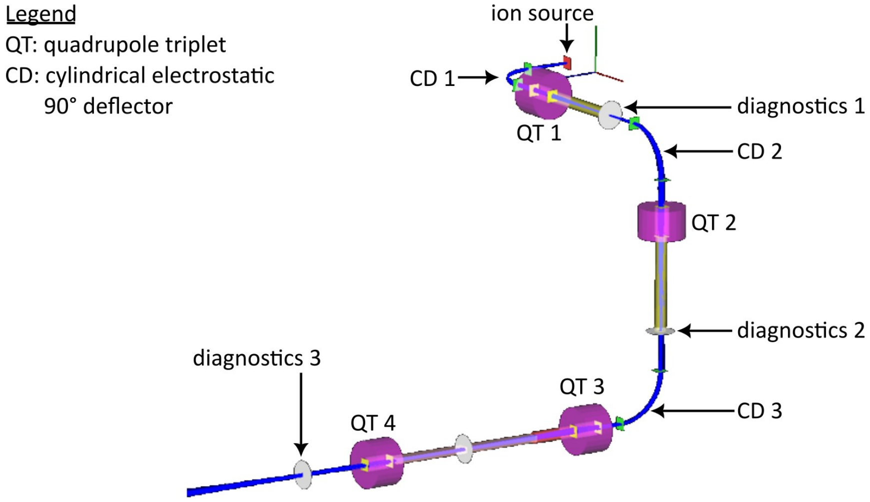

Figure A.3: G4beamline simulation of the electrostatic branch of the 300 kV ion source platform (see figure 3.6) based on the G4beamline input file by P. M. Mishra. The figure shows the graphical output of the simulated beamline with the ion beam in blue. Labels and legend were added subsequently. The shown figure is (with kind permission of M. Grieser) an adapted version of a figure provided by M. Grieser.

Using the quadrupole triplets QT 1–4, the voltages of the modeled electrostatic elements were optimized to focus the ion beam as small as possible at the position of diagnostics 1–3. Figure A.4 shows the ion beam profile at the respective positions, while figure A.5 shows the corresponding horizontal and vertical phase space diagrams. The green ellipses are fitted and contain 90% of all particles in the respective diagram. The transmission through the beamline from the ion source (see figure A.3) up to diagnostics 3 is determined by comparing the number of particles within the ellipse (see figure A.5) to the initial number of particles. It is about $T_{\text{sim}} = 76\%$.

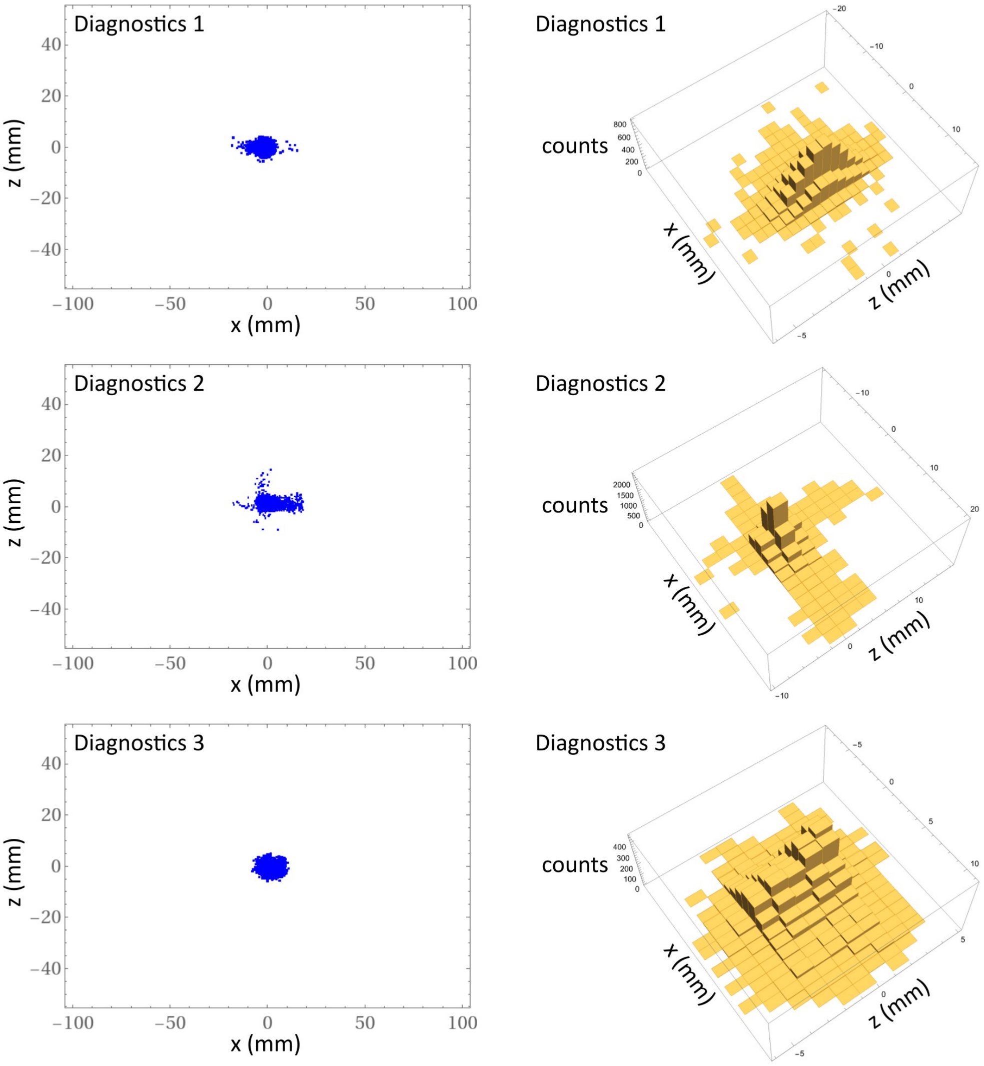

Figure A.4: Two-dimensional (left column) and three-dimensional (right column) depiction of the ion beam profile at the positions of diagnostics 1–3 (see figure A.3 and 3.6). Labels were added subsequently. The shown figures are (with kind permission of M. Grieser) adapted versions of figures created with Mathematica by M. Grieser.

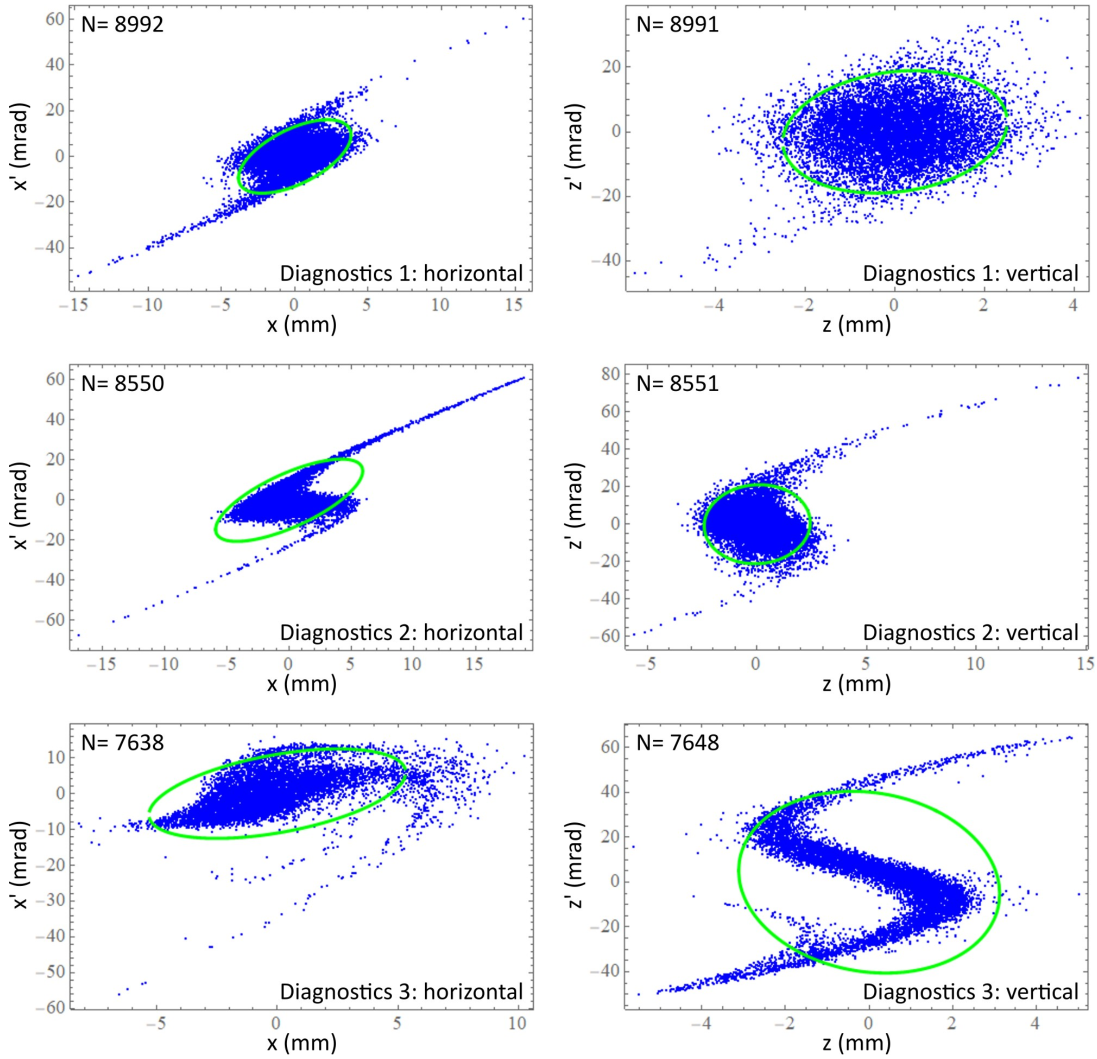

Figure A.5: Horizontal (left column) and vertical (right column) phase space diagrams of the ion beam at the positions of diagnostics 1–3 (see figure A.3 and 3.6). Stated in each diagram is the number N of particles within the green ellipse, which corresponds to 90% of all particles in the diagram. Labels were added subsequently. The shown figures are (with kind permission of M. Grieser) adapted versions of figures created with Mathematica by M. Grieser.

A.4 Additional information on the LVAP ion source

Here we give information on the in-house-built valve used for generating short and dense gas pulses for cluster production with the LVAP ion source (section A.4.1). Furthermore, we discuss cationic LVAP mass spectra obtained at the Ion Source Test Bench (ISTB) for aluminum ablation targets of different purity (section A.4.2).

A.4.1 In-house-built pulsed valve

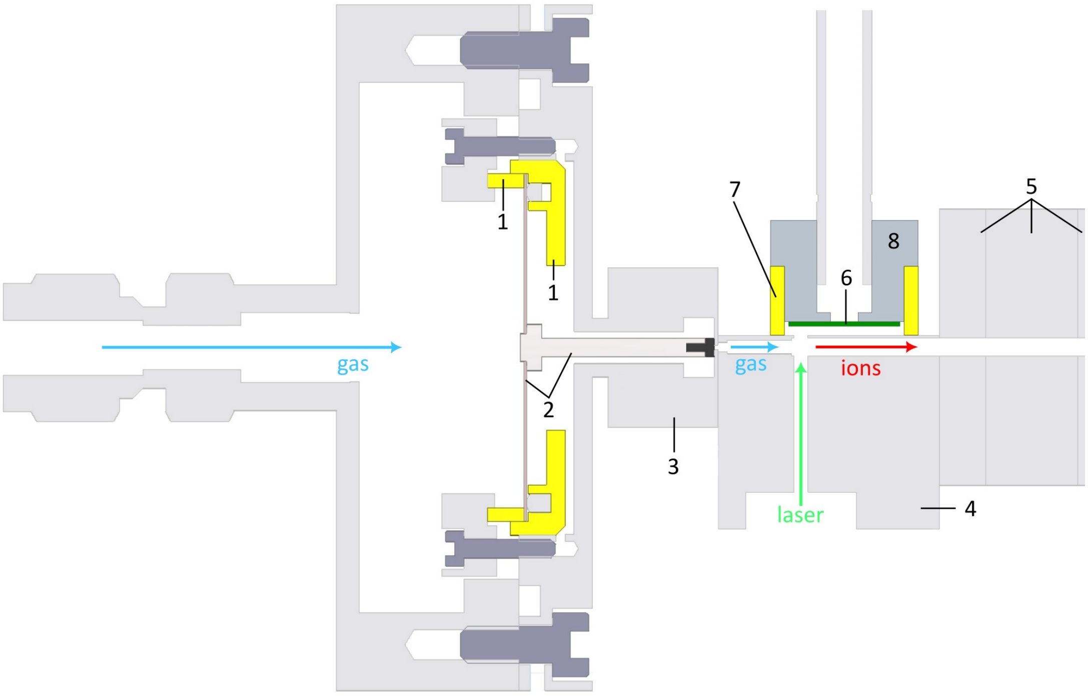

Figure A.6: Sectional view of the in-house-built valve and the components around the vaporization block: (1) electrical insulator (2) perforated piezo disk and plunger with black PTFE tip (3) nozzle (4) vaporization block (5) cluster growth channel (6) ablation target (7) PTFE spacer (8) target holder.

The pulsed valve of the previous LVAP version (figure A.6) is in-house-built (Meyer 2014). From inside the gas-filled valve body, a plunger with a PTFE tip seals a small hole (0.5 mm diameter) in the nozzle. The plunger is glued onto a piezo ceramic disk. The disk deforms temporarily if a voltage pulse is applied to one side. The plunger pulls back by a small distance and shortly unblocks the hole in the nozzle, so that gas from inside the valve body flows into the channel. The resulting gas pulse then cools the plasma plume and promotes the formation of clusters. The new commercial valve is also based on a piezo element, but uses the cantilever design (Irimia et al. 2009). In contrast to the in-house-built valve, its dedicated nozzle is not directly attached to the vaporization block (see figure 3.12). It is encased in a construct which allows to switch to the in-house-built valve. The construct features a PTFE gasket and a second nozzle with a long and thin channel connecting the commercial valve to the vaporization block.

A.4.2 Cationic LVAP ion source spectra

Here we compare cationic spectra of the LVAP ion source (section 3.2.3) recorded for aluminum targets of different purity. The spectra not only yield information about contaminant ion species, but may also be used for qualitatively estimating the temperature of the ablation plasma from which the clusters are formed. For recording the spectra at the ISTB (section 3.2.1), the voltage polarities at all ion-optical elements were switched for accelerating and transporting positive ions.

Except for the target materials and detector settings, we recorded all cationic spectra for unchanged parameters, i.e., 5 keV ion kinetic energy, 13 bar He backing pressure, 50 µs Opening Duration of the pulsed valve, 100 µs Laser Pulse Delay, 3.2 mJ laser pulse energy at the target, 50 mm growth channel length and 4 mm distance between growth channel and skimmer (3 mm orifice diameter). For the stated backing pressure we obtained by far the highest ion yield. The horizontal and vertical slits $[x, y]$ of the mass spectrometer were set to $[2\text{ mm}, 2\text{ mm}]$ (slits 1) and $[2\text{ mm}, 2\text{ mm}]$ (slits 2). We employed the channeltron of diagnostics 2 for ion detection and the same ion number calibration as for negative ions (section A.2.2). Note that for the strongest component in each spectrum we used voltages U'_{in} below the range covered by the ion number calibration curve (figure A.2). For this case we exponentially extrapolated the detector gain factor according to equation A.18.

We used high-purity aluminum[1] for the spectra in figure A.7, where the ion number is plotted against the mass-to-charge ratio. The spectra feature one strong component (orange line) and zoom in further, so that weaker components (green and blue lines) become visible successively. At the highest magnification, we found no components for $m/q > 100$ u/e.

We explain the strong component by Al^+, and the other peaks by contributions of the backing gas (He), residual water in the gas line and small leaks allowing atmospheric air to enter the gas line. Apart from Al_2^+ we see no larger clusters.

For the spectra displayed in figure A.8, we used the aluminum[2] target holder (see figure 3.12) as ablation target. Again, the spectra feature one strong component and no components with $m/q > 100$ u/e. We now encounter more peaks than in the high-purity aluminum spectrum. We partly explain the additional peaks by other metals contained in the target alloy. Apparently, the He dimer is now also present. The peak

---

[1] Aluminum foil, $\geq 99.999\%$ purity, 0.25 mm thickness, Merck KGaA

[2] Al alloy containing mostly Al and (in percent by weight) 2.6–3.3% Mg, 0–0.4% Mn, 0–0.3% Cr, $\leq 0.5\%$ Si, $\leq 0.4\%$ Fe, $\leq 0.2\%$ Zn and $\leq 0.05\%$ Cu (Altenpohl 1965).

assigned to Mn^+ may also partly be explained by the presence of Al_2H^+. Compared to the Al^+ peak, the contribution of Mg to the spectrum is about 2%, which is on the order of the Mg impurity in the alloy.

Using cationic LVAP spectra, we are thus capable of distinguishing target compositions differing by impurities down to few per mill by weight. Apart from composition analysis, the spectra also allow to qualitatively infer the temperature of the laser-ignited ablation plasma, which is injected into (and cooled by) the cold and high-density He gas pulse. According to Duncan 2012, the presence of cations of the He backing gas is a good indicator for a too hot plasma. As a high plasma temperature hampers efficient cluster condensation, this explains why the Al^+ monomer peak dominates and almost no clusters form.

To conclude: As the chosen ion source settings favor the production of monomers in the cationic spectra, they are well-suited for analysis of the target material. For cluster production, other ion source conditions leading to a colder plasma should be chosen, e.g., as in the anionic spectra in figure 3.16.

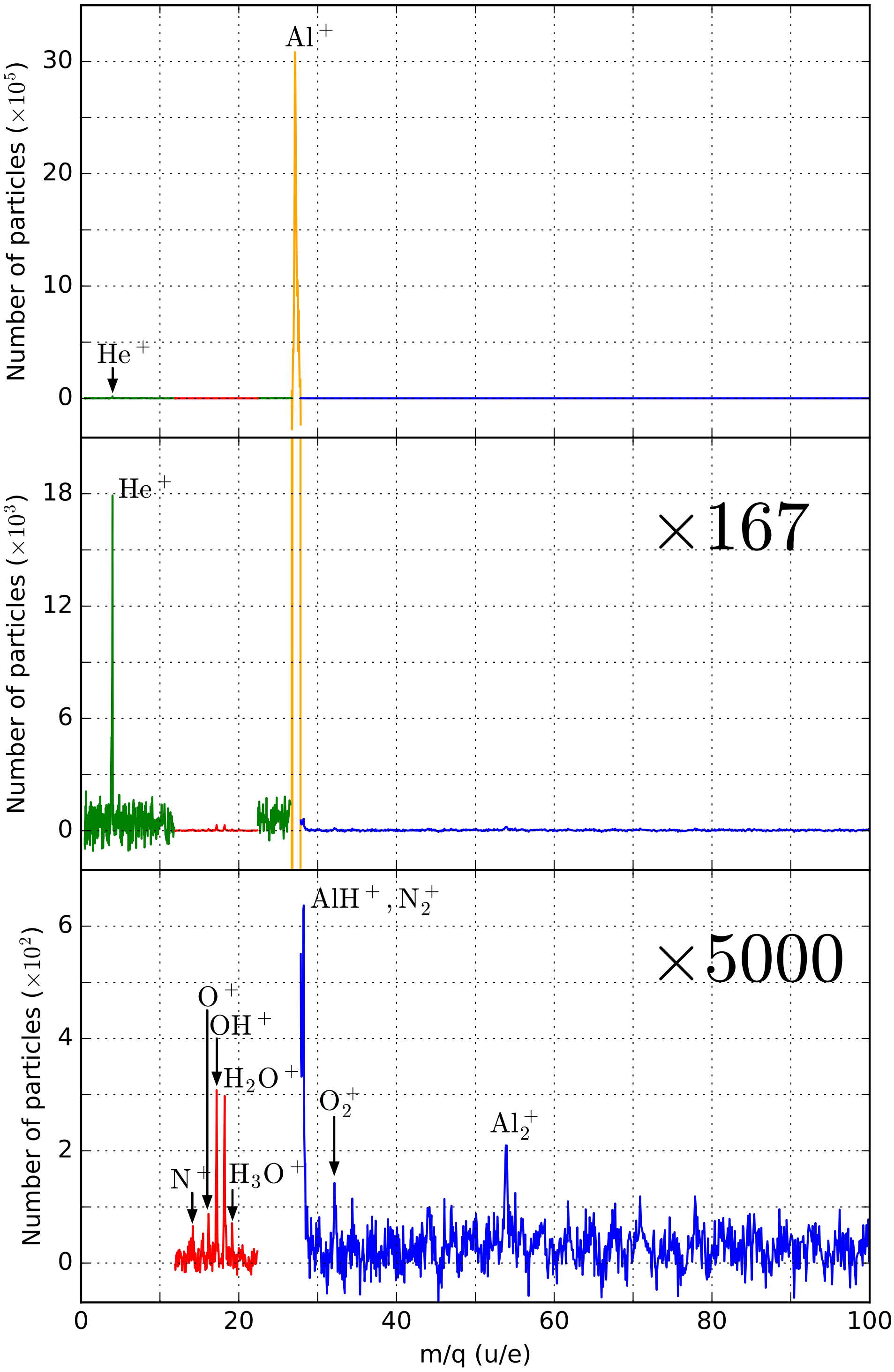

Figure A.7: Spectra of positive ions produced with an LVAP ion source equipped with a high-purity aluminum ablation target. We used 2 kV (orange), 2.7 kV (green), 3 kV (blue) and 3.1 kV (red) as channeltron input voltage U'_{in}.

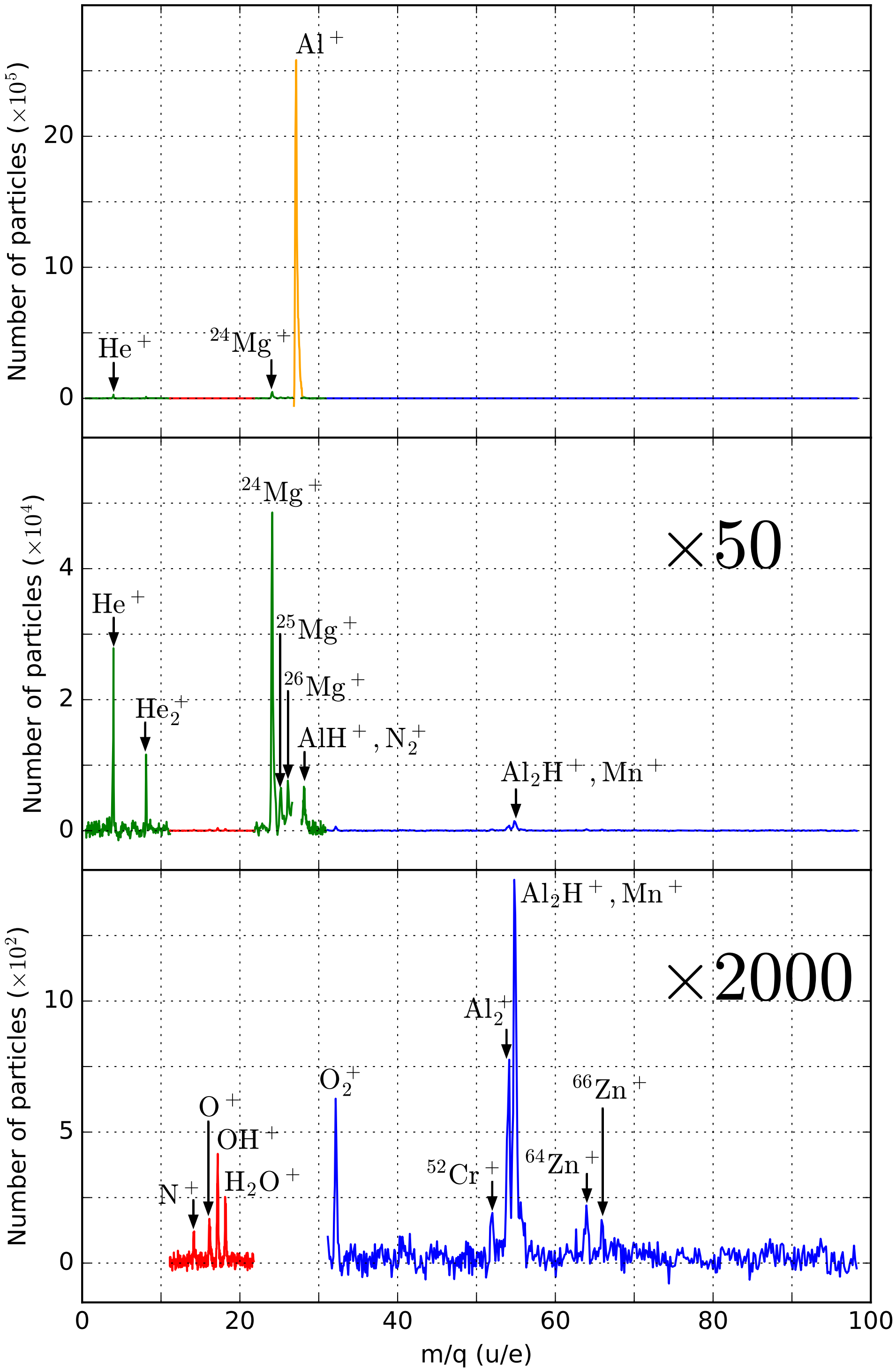

Figure A.8: Spectra of positive ions produced with an LVAP ion source equipped with an aluminum alloy² target. We used 2.2 kV (orange), 2.7 kV (green), 3 kV (blue) and 3.1 kV (red) channeltron input voltages U'_{in}.

Appendix B

Supplementary information on the vinylidene anion stability experiment

This chapter gives information on the data processing and the uncertainty estimates of the vinylidene anion stability experiment presented in chapter 4. Here, we define the relevant measured quantities in the H_2CC^- experiment (section B.1). We then describe how we process the measured data (section B.2) and give a quantitative overview of the statistical and systematic uncertainties (section B.3). Lastly, we explain how we propagate the uncertainties to the final result, i.e., the laser yield ratio (section B.4).

B.1 Measured quantities of the yield ratio

The yield ratio (equation 4.36 in section 4.2.4) is determined by different measured quantities. These quantities have systematic and statistical uncertainties. Here, we give all quantities relevant for the further error propagation.

According to equation 4.36, the yield ratio is determined by measured detector counts $\tilde{N}$ and the laser pulse energies E in the ion-photon interaction region:

$$
\begin{aligned}
Y_{\mathrm{UV}}^{\mathrm{VIS}}(t) &= \frac{Y^{\mathrm{VIS}}(t)}{Y^{\mathrm{UV}}(t)} && \text{(B.1)} \\
&= \frac{\tilde{N}^{\mathrm{VIS}}(t) E^{\mathrm{UV}}(t)}{\tilde{N}^{\mathrm{UV}}(t) E^{\mathrm{VIS}}(t)} && \text{(B.2)}
\end{aligned}
$$

As the ion-photon interaction region is not directly accessible for laser pulse energy measurements, we monitored the laser pulse energies elsewhere in the laser setup (section 4.2.1) and estimated the energies in the interaction region by means of calibration factors T_{VIS} and T_{UV}. These factors are determined by calibration measurements and the transmission factors of the CSR laser windows. The energies in the interaction region are then expressed as

$$E^{\text{VIS}} = E^{\text{VIS}}_{\text{meas}} T_{\text{VIS}} \tag{B.3}$$

$$E^{\text{UV}} = E^{\text{UV}}_{\text{meas}} T_{\text{UV}}, \tag{B.4}$$

where E_{meas} are the measured laser pulse energies.

Also, as described in section B.2 the detector events $\tilde{N}$ are already corrected for the background $\tilde{N}^{\text{RG}}$ resulting from CED events and dark counts. To account for the different durations of their acquisition time windows[1], $\tilde{N}^{\text{RG}}$ is scaled by a factor w_2 before being subtracted from the uncorrected laser-induced counts $\tilde{N}_{\text{uncorr}}$:

$$\tilde{N}^{\text{VIS}}(t) = \tilde{N}^{\text{VIS}}_{\text{uncorr}}(t) - \tilde{N}^{\text{RG}}(t)/w_2 \tag{B.5}$$

$$\tilde{N}^{\text{UV}}(t) = \tilde{N}^{\text{UV}}_{\text{uncorr}}(t) - \tilde{N}^{\text{RG}}(t)/w_2 \tag{B.6}$$

With equations B.3–B.6, the yield ration then reads:

$$Y^{\text{VIS}}_{\text{UV}}(t) = \frac{\left(\tilde{N}^{\text{VIS}}_{\text{uncorr}}(t) - \tilde{N}^{\text{RG}}(t)/w_2\right) E^{\text{UV}}_{\text{meas}}(t)}{\left(\tilde{N}^{\text{UV}}_{\text{uncorr}}(t) - \tilde{N}^{\text{RG}}(t)/w_2\right) E^{\text{VIS}}_{\text{meas}}(t)} \frac{T_{\text{UV}}}{T_{\text{VIS}}} \tag{B.7}$$

Note that as the scaling factor is very large ($w_2 > 4 \times 10^6$, see section 4.3.1), the background $\tilde{N}^{\text{RG}}$ together with its uncertainty appears to be negligible in first order. At long storage times, where the ratio is significantly lower due to the exponential ion decay, this may not necessarily be true. We thus include $\tilde{N}^{\text{RG}}$ in the analysis. Also, the laser calibration factors (T_{VIS}, T_{UV}) are partly determined by transmission factors of optical components of the setup, and partly by averaging over a certain number of laser shots in the course of the calibration measurements. As we do not change the laser setup, we assume these factors to remain constant once determined. As they do not depend on t, they can only scale the temporal evolution of the laser yield ratio, but not change it. Hence, the factors do not affect the measured H_2CC^- decay rate.

B.2 Data processing

Here, we describe how we process the experiment data such that the exponential laser yield and yield ratio models (equations 4.27, 4.35 and 4.36 in section 4.2.4) may be fitted to it.

---

[1] As described in section 4.3.1 photodetachment neutral events are collected in time windows which are a factor of w_2 shorter than the time windows for collecting CED background events.

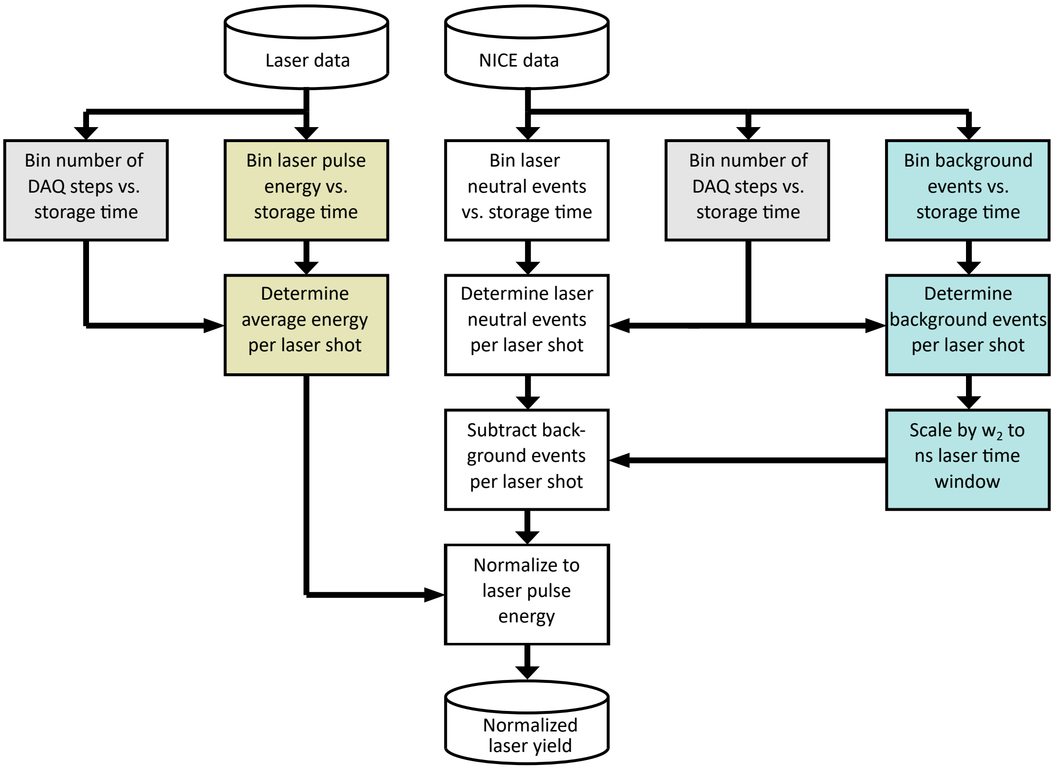

Figure B.1: Flow of the H_2CC^- experimental data for determining the average laser yield $Y_i(t)$ in each experimental cycle i. From the NICE detector data, neutral events due to laser photodetachment and Collisional Electron Detachment (CED) are selected and processed. The number of Data AcQuisition (DAQ) steps is needed for determining the average energy per laser pulse and the number of neutral events per laser shot.

The data flow diagram in figure B.1 visualizes the steps carried out for each experimental cycle (fixed duration up to 3300 s, see figure 4.3 in section 4.2.2) and laser (VIS and UV): We divide each cycle i into time bins of equal duration (typically 10–250 s) and bin the measured values of each quantity according to their acquisition time t relative to the cycle starting time. This time coincides with the ion injection into the ring, i.e., the start of the storage. With the time-binned data, we perform all further steps bin-wise. With respect to the laser data, we determine the average laser pulse energy per laser shot E_i. The number of laser shots is given by the number of Data AcQuisition (DAQ) steps (section 4.2.2). Per DAQ step, the VIS laser fires once and the UV laser fires twice (figure 4.3 in section 4.2.2). With regard to the NICE detector data, we determine the average neutral photodetachment events $\tilde{N}_{\mathrm{uncorr,i}}$ and the average background events $\tilde{N}_i^{\mathrm{RG}}$ per laser shot (figure 4.6 in section 4.3.1). We then scale the background signal by a factor w_2 determined by the ratio between the acquisition windows for background and photodetachment neutral events (see equation B.6), and subtract the scaled background signal from the photodetachment signal. This step removes not only CED, but all non-laser induced signals, which is dominated by the

NICE detector dark counts present as constant offset in both signals. It is necessary since applying pulse-height cuts only (see section 4.3.2) does not suppress the dark counts completely. Dividing the offset-corrected photodetachment events $\tilde{N}_i$ by the average laser pulse energy E_i then results in the desired normalized average laser yields for the VIS and UV laser and each experimental cycle i:

$$Y_i^{\mathrm{VIS}}(t) \propto \frac{\tilde{N}_i^{\mathrm{VIS}}(t)}{E_i^{\mathrm{VIS}}(t)} \tag{B.8}$$

$$Y_i^{\mathrm{UV}}(t) \propto \frac{\tilde{N}_i^{\mathrm{UV}}(t)}{E_i^{\mathrm{UV}}(t)} \tag{B.9}$$

Next, we determine the overall yield ratio by summing up the cycle-specific yield ratio values $(Y_{\mathrm{UV}}^{\mathrm{VIS}}(t))_i = Y_i^{\mathrm{VIS}}(t)/Y_i^{\mathrm{UV}}(t)$ for all cycles i:

$$\sum_i \left(Y_{\mathrm{UV}}^{\mathrm{VIS}}(t)\right)_i = \sum_i \frac{Y_i^{\mathrm{VIS}}(t)}{Y_i^{\mathrm{UV}}(t)} \tag{B.10}$$

For the VIS and UV laser, equations 4.25–4.27 and 4.29–4.34 in section 4.2.4 express the relation between the exponential decay and the yield, respectively. Using these equations and the abbreviations A_i and B_i for their time-independent prefactors, the yield ratio takes the following form, which is simplified further:

$$\begin{aligned}
\sum_i \left(Y_{\mathrm{UV}}^{\mathrm{VIS}}(t)\right)_i &\approx \sum_i \frac{A_i e^{-(k_0+k_1^{\mathrm{RG}}+k_1^{\mathrm{VIS}}+k_1^{\mathrm{UV}}+k)t}}{B_i e^{-(k_0+k_2^{\mathrm{RG}}+k_2^{\mathrm{UV}})t}} && \text{(B.11)}\\
&= \frac{e^{-(k_0+k_1^{\mathrm{RG}}+k_1^{\mathrm{VIS}}+k_1^{\mathrm{UV}}+k)t}}{e^{-(k_0+k_2^{\mathrm{RG}}+k_2^{\mathrm{UV}})t}} \underbrace{\sum_i \frac{A_i}{B_i}}_{C} && \text{(B.12)}\\
&= C e^{-(k_1^{\mathrm{RG}}-k_2^{\mathrm{RG}}+k_1^{\mathrm{VIS}}+k_1^{\mathrm{UV}}-k_2^{\mathrm{UV}}+k)t} && \text{(B.13)}\\
&= C e^{-k^{\mathrm{eff}}t}. && \text{(B.14)}
\end{aligned}$$

Except for a constant prefactor C, the exponential function containing the effective rate k^{eff} (see equations 4.36–4.41 in section 4.2.4) is reproduced correctly. The modeled decay rates may thus be fitted to the experimental data evaluated by this method, and the respective rates may be extracted.

B.3 Quantitative overview of the uncertainties

In order to reveal the uncertainties which dominate the final uncertainty of the laser yield ratio in each experimental cycle, we give here a quantitative overview. The estimated relative uncertainty values are given in table B.1. Subdivided into statistical and systematic uncertainties, all quantities from equation B.7 and their individual contributions are listed. The stated uncertainties of the time-dependent variables ($\tilde{N}$, time-drift of E_{meas}) are typical values for data binned in steps of 250 s, as used later for binning the final data (see section 4.4). Also, the shown numerical values are typical for a single experimental cycle. Due to averaging over multiple individual cycles, the data displayed later in section 4.4 has smaller relative statistical uncertainties. The systematic uncertainties of variables related to the measurement of laser energies (E_{meas}, T_{VIS}, T_{UV}) either result from the specifications of the energy meters, or from the observed laser intensity drift. In the case of the calibration factors (T_{VIS}, T_{UV}) the displayed uncertainties are already propagated from several individual reference measurements.

It is to be noted here that we noticed a clear difference in the temporal behaviour of the two laser systems on the time scale of the data binning used later in section 4.4 (250 s): While the UV laser output drifted very little, the VIS laser output showed a significant systematic drift. The respective systematic uncertainties reflect this observation. As the two reference measurements for determining T_{VIS} were carried out with the same energy meter head, the absolute energy calibration uncertainty does not play a role here.

With regard to the statistical uncertainties, the VIS-induced detector counting statistics dominate by far, followed by the UV-induced counts. The relative influence of the background events and the random laser fluctuation is negligible. The statistical uncertainties of the respective measured laser pulse energies are negligible as well. Overall, within a single experimental cycle, the statistical uncertainties dominate by far, which is given by the low detector count rate for VIS-induced events.

B.4 Propagation of uncertainties

Here we outline how we propagate the uncertainties of the measured variables to the final yield ratio. According to equations B.11–B.14 in section B.2 the final yield ratio is the sum of the yield ratios of the individual experimental cycles i. Also, we showed that the final yield ratio can be related to the single exponential decay containing the effective rate k_{eff}:

$$\begin{aligned} Y_{\text{UV}}^{\text{VIS}}(t) &= \sum_i \left(Y_{\text{UV}}^{\text{VIS}}(t)\right)_i && \text{(B.15)} \\ &= \frac{T_{\text{UV}}}{T_{\text{VIS}}} \sum_i \frac{\tilde{N}_i^{\text{VIS}}(t) E_{\text{meas,i}}^{\text{UV}}(t)}{\tilde{N}_i^{\text{UV}}(t) E_{\text{meas,i}}^{\text{VIS}}(t)} && \text{(B.16)} \\ &\approx C e^{-k^{\text{eff}} t}. && \text{(B.17)} \end{aligned}$$

Table B.1: Quantitative overview of the relative statistical and systematic uncertainties of the measured quantities of the H_2CC^- lifetime experiment. For more details, see the text.

Quantity	Type	Contribution	Rel. unc. (%)
$\tilde{N}^{\mathrm{RG}}(t)$	Statistical	Background events counting	0.6–1.0
$\tilde{N}^{\mathrm{VIS}}(t)$	Statistical	VIS events counting	33–61
$\tilde{N}^{\mathrm{UV}}(t)$	Statistical	UV events counting	7–14
$E^{\mathrm{VIS}}_{\mathrm{meas}}(t)$	Statistical	Random intensity fluctuation	< 0.1
	Systematic	Laser intensity drift	2.0
		Absolute energy calibration uncertainty	4.0
		Readout accuracy	1.1
		Readout resolution	< 0.2
$E^{\mathrm{UV}}_{\mathrm{meas}}(t)$	Statistical	Random intensity fluctuation	< 0.1
	Systematic	Laser intensity drift	< 0.2
		Absolute energy calibration uncertainty	4.0
		Readout accuracy	1.0
		Readout resolution	< 0.1
T_{VIS}	Statistical	Random intensity fluctuation	< 0.2
	Systematic	Laser intensity drift	7.1
		Absolute energy calibration uncertainty	-
		Readout accuracy	1.5
		Readout resolution	< 0.1
T_{UV}	Statistical	Random intensity fluctuation	0.5
	Systematic	Laser intensity drift	0.4
		Absolute energy calibration uncertainty	5.7
		Readout accuracy	4.8
		Readout resolution	< 0.1

If we compare equations B.16 and B.17 it becomes apparent that only the time-dependent measured variables are relevant for determining the effective rate k^{eff}. The time-independent laser calibration factors are reflected by the constant C, and only needed if the absolute value of the yield ratio is relevant. Their uncertainty is irrelevant for the uncertainty of k^{eff}. For each experimental cycle i, the uncertainty of the bin-wise yield ratio is thus determined from the relative uncertainties of the time-dependent quantities. We treat these quantities as uncorrelated. The relative uncertainty of the yield ratio is then:

$$\left(\frac{\Delta Y_{\text{UV}}^{\text{VIS}}(t)}{Y_{\text{UV}}^{\text{VIS}}(t)}\right)_i = \sqrt{\left(\frac{\Delta\tilde{N}_i^{\text{VIS}}(t)}{\tilde{N}_i^{\text{VIS}}(t)}\right)^2 + \left(\frac{\Delta\tilde{N}_i^{\text{UV}}(t)}{\tilde{N}_i^{\text{UV}}(t)}\right)^2 + \left(\frac{\Delta E_{\text{meas,i}}^{\text{UV}}(t)}{E_{\text{meas,i}}^{\text{UV}}(t)}\right)^2 + \left(\frac{\Delta E_{\text{meas,i}}^{\text{VIS}}(t)}{E_{\text{meas,i}}^{\text{VIS}}(t)}\right)^2} \tag{B.18}$$

Note that, as the laser-induced events are already offset-corrected according to equations B.5 and B.6, their absolute uncertainties may be determined by quadratic addition of their individual uncertainties:

$$\Delta\tilde{N}_i^{\text{VIS}}(t) = \sqrt{\left(\Delta\tilde{N}_{\text{uncorr,i}}^{\text{VIS}}(t)\right)^2 + \left(w_2^{-1}\Delta\tilde{N}_i^{\text{RG}}(t)\right)^2} \tag{B.19}$$

As $w_2 > 4 \times 10^6$ (see section B.1) this step may in principle be omitted. The absolute uncertainty of the final yield ratio is then determined from the sum of squares of the cycle-specific absolute uncertainties:

$$\Delta Y_{\text{UV}}^{\text{VIS}} = \sqrt{\sum_i \left(\Delta Y_{\text{UV}}^{\text{VIS}}\right)_i^2} \tag{B.20}$$

My Publications

This thesis partly builds on the following article published during the course of the described work:

Grieser, M., V. C. Schmidt, K. Blaum, F. Grussie, R. von Hahn, Á. Kálosi, H. Kreckel, D. Müll, O. Novotný, F. **Nuesslein**, and A. Wolf (2022). „Isochronous mass spectrometry in an electrostatic storage ring.“ In: *Review of Scientific Instruments* 93.6. DOI: `10.1063/5.0090131`.

Additionally, the following articles were published during the preparation time of this thesis:

Jain, N., Á. Kálosi, F. **Nuesslein**, D. Paul, P. Wilhelm, S. G. Ard, M. Grieser, R. von Hahn, M. C. Heaven, E. Miliordos, D. Maffucci, N. S. Shuman, A. A. Viggiano, A. Wolf, and O. Novotný (2023). „Near-thermo-neutral electron recombination of titanium oxide ions.“ In: *The Journal of Chemical Physics* 158.14. DOI: `10.1063/5.0146365`.

Müll, D., F. Grussie, K. Blaum, S. George, J. Göck, M. Grieser, R. von Hahn, Z. Harman, Á. Kálosi, C. H. Keitel, C. Krantz, C. Lyu, O. Novotný, F. **Nuesslein**, D. Paul, V. C. Schmidt, S. Singh, S. Sunil Kumar, X. Urbain, A. Wolf, and H. Kreckel (2021). „Metastable states of Si^- observed in a cryogenic storage ring.“ In: *Physical Review A* 104.3, p. 032811. DOI: `10.1103/physreva.104.032811`.

Novotný, O., P. Wilhelm, D. Paul, Á. Kálosi, S. Saurabh, A. Becker, K. Blaum, S. George, J. Göck, M. Grieser, F. Grussie, R. von Hahn, C. Krantz, H. Kreckel, C. Meyer, P. M. Mishra, D. Muell, F. **Nuesslein**, D. A. Orlov, M. Rimmler, V. C. Schmidt, A. Shornikov, A. S. Terekhov, S. Vogel, D. Zajfman, and A. Wolf (2019). „Quantum-state–selective electron recombination studies suggest enhanced abundance of primordial HeH^+.“ In: *Science* 365.6454, pp. 676–679. DOI: `10.1126/science.aax5921`.

Bibliography

Altenpohl, D. (1965). *Aluminium und Aluminiumlegierungen.* Springer Berlin Heidelberg. DOI: 10.1007/978-3-662-30245-3.

Altevogt, S. (2003). „Production of rotationally cold H_3^+ ions with a hollow cathode ion source.“ Diploma thesis. Ruprecht-Karls Universität Heidelberg.

Bacal, M., M. Sasao, and M. Wada (2021). „Negative ion sources.“ In: *Journal of Applied Physics* 129.22. DOI: 10.1063/5.0049289.

Becker, A. (2016). „Imaging of Neutral Fragmentation Products from Fast Molecular Ion Beams: Paving the Way for Reaction Studies in Cryogenic Environment.“ PhD thesis. DOI: 10.11588/HEIDOK.00020213.

Belau, L., S. E. Wheeler, B. W. Ticknor, M. Ahmed, S. R. Leone, W. D. Allen, H. F. Schaefer, and M. A. Duncan (2007). „Ionization thresholds of small carbon clusters: tunable VUV experiments and theory.“ In: *Journal of the American Chemical Society* 129.33, pp. 10229–10243. DOI: 10.1021/ja072526q.

Ben-Shabo, Y., A. Kurbanov, C. D. Schröter, R. Moshammer, H. Kreckel, and Y. Toker (2023). „Velocity map imaging with no spherical aberrations.“ In: *Physical Chemistry Chemical Physics* 25.37, pp. 25122–25129. DOI: 10.1039/d3cp03693f.

Best, T., R. Otto, S. Trippel, P. Hlavenka, A. von Zastrow, S. Eisenbach, S. Jézouin, R. Wester, E. Vigren, M. Hamberg, and W. D. Geppert (2011). „Absolute photodetachment cross-section measurements for hydrocarbon chain anions.“ In: *The Astrophysical Journal* 742.2, p. 63. DOI: 10.1088/0004-637x/742/2/63.

Blewett, J. P. and E. J. Jones (1936). „Filament Sources of Positive Ions.“ In: *Physical Review* 50.5, pp. 464–468. DOI: 10.1103/physrev.50.464.

Bondybey, V. E. and J. H. English (1981). „Laser induced fluorescence of metal clusters produced by laser vaporization: Gas phase spectrum of Pb_2.“ In: *The Journal of Chemical Physics* 74.12, pp. 6978–6979. DOI: 10.1063/1.441064.

Brandenstein, C., S. Stelzl, E. Gutsmiedl, W. Schott, A. Weiler, and P. Fierlinger (2023). „Towards an electrostatic storage ring for fundamental physics measurements.“ In: *EPJ Web of Conferences* 282. Ed. by A. Gligorova, C. Amsler, M. Simon, and E. Widmann, p. 01017. DOI: 10.1051/epjconf/202328201017.

Breitenfeldt, C., K. Blaum, S. George, J. Göck, G. Guzmán-Ramírez, J. Karthein, T. Kolling, M. Lange, S. Menk, C. Meyer, J. Mohrbach, G. Niedner-Schatteburg, D. Schwalm, L. Schweikhard, and A. Wolf (2018). „Long-Term Monitoring of the Internal Energy Distribution of Isolated Cluster Systems.“ In: *Physical Review Letters* 120.25, p. 253001. DOI: `10.1103/physrevlett.120.253001`.

Bull, J. N., M. S. Scholz, E. Carrascosa, M. K. Kristiansson, G. Eklund, N. Punnakayathil, N. de Ruette, H. Zettergren, H. T. Schmidt, H. Cederquist, et al. (2019). „Ultraslow radiative cooling of C_n^- (n = 3–5).“ In: *The Journal of Chemical Physics* 151.11. DOI: `10.1063/1.5114678`.

Cavanagh, S. J., S. T. Gibson, M. N. Gale, C. J. Dedman, E. H. Roberts, and B. R. Lewis (2007). „High-resolution velocity-map-imaging photoelectron spectroscopy of the O^- photodetachment fine-structure transitions.“ In: *Physical Review A* 76.5, p. 052708. DOI: `10.1103/physreva.76.052708`.

Chandrasekhar, J., R. A. Kahn, and P. von Ragué Schleyer (1982). „The preferred structure of $C_2H_2^-$.“ In: *Chemical Physics Letters* 85.5-6, pp. 493–495. DOI: `10.1016/0009-2614(82)80343-6`.

Cox, A. N., ed. (2002). *Allen's Astrophysical Quantities*. Springer New York. DOI: `10.1007/978-1-4612-1186-0`.

Demtröder, W. (2017). *Experimentalphysik 2*. Springer Berlin Heidelberg. DOI: `10.1007/978-3-662-55790-7`.

Demtröder, W. (2021). *Experimentalphysik 1: Mechanik und Wärme*. Springer Berlin Heidelberg. DOI: `10.1007/978-3-662-62728-0`.

DeVine, J. A., M. L. Weichman, B. Laws, J. Chang, M. C. Babin, G. Balerdi, C. Xie, C. L. Malbon, W. C. Lineberger, D. R. Yarkony, R. W. Field, S. T. Gibson, J. Ma, H. Guo, and D. M. Neumark (2017). „Encoding of vinylidene isomerization in its anion photoelectron spectrum.“ In: *Science* 358.6361, pp. 336–339. DOI: `10.1126/science.aao1905`.

DeVine, J. A., M. L. Weichman, C. Xie, M. C. Babin, M. A. Johnson, J. Ma, H. Guo, and D. M. Neumark (2018). „Autodetachment from Vibrationally Excited Vinylidene Anions.“ In: *The Journal of Physical Chemistry Letters* 9.5, pp. 1058–1063. DOI: `10.1021/acs.jpclett.8b00144`.

DeVine, J. A., M. L. Weichman, X. Zhou, J. Ma, B. Jiang, H. Guo, and D. M. Neumark (2016). „Non-Adiabatic Effects on Excited States of Vinylidene Observed with Slow Photoelectron Velocity-Map Imaging.“ In: *Journal of the American Chemical Society* 138.50, pp. 16417–16425. DOI: `10.1021/jacs.6b10233`.

Dietz, T. G., M. A. Duncan, D. E. Powers, and R. E. Smalley (1981). „Laser production of supersonic metal cluster beams.“ In: *The Journal of Chemical Physics* 74.11, pp. 6511–6512. DOI: `10.1063/1.440991`.

Douguet, N., V. Kokoouline, and A. E. Orel (2014). „Photodetachment cross sections of the $C_{2n}H^-$ (n = 1–3) hydrocarbon-chain anions.“ In: *Physical Review A* 90.6, p. 063410. DOI: `10.1103/physreva.90.063410`.

Dressler, R. and M. Allan (1987). „A dissociative electron attachment, electron transmission, and electron energy-loss study of the temporary negative ion of acetylene.“ In: *The Journal of Chemical Physics* 87.8, pp. 4510–4518. DOI: 10.1063/1.452864.

Duncan, M. A. (2012). „Invited Review Article: Laser vaporization cluster sources.“ In: *Review of Scientific Instruments* 83.4. DOI: 10.1063/1.3697599.

Eliseev, S. and Y. Novikov (2023). „High-precision Penning-trap mass spectrometry for neutrino physics.“ In: *The European Physical Journal A* 59.2. DOI: 10.1140/epja/s10050-023-00946-4.

Ervin, K. M., J. Ho, and W. C. Lineberger (1989). „A study of the singlet and triplet states of vinylidene by photoelectron spectroscopy of $H_2C = C^-$, $D_2C = C^-$, and $HDC = C^-$. Vinylidene–acetylene isomerization.“ In: *The Journal of chemical physics* 91.10, pp. 5974–5992. DOI: 10.1063/1.457415.

Ervin, K. M. and W. C. Lineberger (1991). „Photoelectron spectra of dicarbon(1-) and ethynyl(1-).“ In: *The Journal of Physical Chemistry* 95.3, pp. 1167–1177. DOI: 10.1021/j100156a026.

Fantz, U., P. Franzen, W. Kraus, M. Berger, S. Christ-Koch, M. Fröschle, R. Gutser, B. Heinemann, C. Martens, P. McNeely, R. Riedl, E. Speth, and D. Wünderlich (2007). „Negative ion RF sources for ITER NBI: status of the development and recent achievements.“ In: *Plasma Physics and Controlled Fusion* 49.12B, B563–B580. DOI: 10.1088/0741-3335/49/12b/s53.

Fifield, L. K. (1999). „Accelerator mass spectrometry and its applications.“ In: *Reports on Progress in Physics* 62.8, pp. 1223–1274. DOI: 10.1088/0034-4885/62/8/202.

Frenking, G. (1983). „The neutral and ionic vinylidene—acetylene rearrangement.“ In: *Chemical Physics Letters* 100.6, pp. 484–487. DOI: 10.1016/0009-2614(83)87413-2.

Gatchell, M., J. Ameixa, M. Ji, M. H. Stockett, A. Simonsson, S. Denifl, H. Cederquist, H. T. Schmidt, and H. Zettergren (2021). „Survival of polycyclic aromatic hydrocarbon knockout fragments in the interstellar medium.“ In: *Nature Communications* 12.1. DOI: 10.1038/s41467-021-26899-0.

Geistlinger, K., M. Fischer, S. Spieler, L. Remmers, F. Duensing, F. Dahlmann, E. Endres, and R. Wester (2021). „A sub-4 Kelvin radio frequency linear multipole wire trap.“ In: *Review of Scientific Instruments* 92.2. DOI: 10.1063/5.0040866.

Gerardi, H. K., K. J. Breen, T. L. Guasco, G. H. Weddle, G. H. Gardenier, J. E. Laaser, and M. A. Johnson (2010). „Survey of Ar-tagged predissociation and vibrationally mediated photodetachment spectroscopies of the vinylidene anion, $C_2H_2^-$.“ In: *The Journal of Physical Chemistry A* 114.3, pp. 1592–1601. DOI: 10.1021/jp9095419.

Glendening, E. D. and M. L. Strange (2002). „Mechanism of Acetylene-Vinylidene Rearrangement with Na, Al, and Y Atoms.“ In: *The Journal of Physical Chemistry A* 106.32, pp. 7338–7347. DOI: 10.1021/jp020060m.

Grieser, M. (2019). *Private communications.*

Grieser, M., V. C. Schmidt, K. Blaum, F. Grussie, R. von Hahn, Á. Kálosi, H. Kreckel, D. Müll, O. Novotný, F. Nuesslein, and A. Wolf (2022). „Isochronous mass spectrometry in an electrostatic storage ring.“ In: *Review of Scientific Instruments* 93.6, p. 063302. DOI: 10.1063/5.0090131.

Grussie, F., A. P. O’Connor, M. Grieser, D. Müll, A. Znotins, X. Urbain, and H. Kreckel (2022). „An ion-atom merged beams setup at the Cryogenic Storage Ring.“ In: *Review of Scientific Instruments* 93.5. DOI: 10.1063/5.0086391.

Grussie, F. (2016). „Experimental sudies of ion-neutral reactions under astrophysical conditions.“ PhD thesis. DOI: 10.11588/HEIDOK.00021435.

Guo, L., H. Han, J. Ma, and H. Guo (2015). „Quantum Dynamics of Vinylidene Photodetachment on an Accurate Global Acetylene-Vinylidene Potential Energy Surface.“ In: *The Journal of Physical Chemistry A* 119.31, pp. 8488–8496. DOI: 10.1021/acs.jpca.5b05061.

Hahn, R. von, A. Becker, F. Berg, K. Blaum, C. Breitenfeldt, H. Fadil, F. Fellenberger, M. Froese, S. George, J. Göck, M. Grieser, F. Grussie, E. A. Guerin, O. Heber, P. Herwig, J. Karthein, C. Krantz, H. Kreckel, M. Lange, F. Laux, S. Lohmann, S. Menk, C. Meyer, P. M. Mishra, O. Novotný, A. P. O’Connor, D. A. Orlov, M. L. Rappaport, R. Repnow, S. Saurabh, S. Schippers, C. D. Schröter, D. Schwalm, L. Schweikhard, T. Sieber, A. Shornikov, K. Spruck, S. S. Kumar, J. Ullrich, X. Urbain, S. Vogel, P. Wilhelm, A. Wolf, and D. Zajfman (2016). „The cryogenic storage ring CSR.“ In: *Review of Scientific Instruments* 87.6, p. 063115. DOI: 10.1063/1.4953888.

Han, H., A. Li, and H. Guo (2014). „Toward spectroscopically accurate global ab initio potential energy surface for the acetylene-vinylidene isomerization.“ In: *The Journal of Chemical Physics* 141.24. DOI: 10.1063/1.4904859.

Hansen, K. (2013). *Statistical Physics of Nanoparticles in the Gas Phase.* Springer Netherlands. DOI: 10.1007/978-94-007-5839-1.

Hassan, S. Z., J. Tauch, M. Kas, M. Nötzold, H. L. Carrera, E. S. Endres, R. Wester, and M. Weidemüller (2022). „Associative detachment in anion-atom reactions involving a dipole-bound electron.“ In: *Nature Communications* 13.1. DOI: 10.1038/s41467-022-28382-w.

Hayes, R. L., E. Fattal, N. Govind, and E. A. Carter (2001). „Long Live Vinylidene! A New View of the $H_2CC \longrightarrow HCCH$ Rearrangement from ab Initio Molecular Dynamics.“ In: *Journal of the American Chemical Society* 123.4, pp. 641–657. DOI: 10.1021/ja000907x.

Heinicke, E. and H. Baumann (1969). „Penning ion source for MP accelerator.“ In: *Nuclear Instruments and Methods* 74.2, pp. 229–232. DOI: 10.1016/0029-554x(69)90341-3.

Heiße, F., S. Rau, F. Köhler-Langes, W. Quint, G. Werth, S. Sturm, and K. Blaum (2019). „High-precision mass spectrometer for light ions.“ In: *Physical Review A* 100.2, p. 022518. DOI: 10.1103/physreva.100.022518.

Hernández, E. and G. Hinojosa (2018). „Collision induced electron detachment cross sections of the H_2CC^- anion below 10 keV on O_2 and N2.“ In: *International Journal of Mass Spectrometry* 424, pp. 35–39. DOI: 10.1016/j.ijms.2017.11.013.

Hettich, R. L. and C. Jin (1994). „Laser Ablation and Laser Desorption Techniques with Fourier-Transform Mass Spectrometry (FTMS).“ In: *Springer Series in Materials Science*. Springer Berlin Heidelberg, pp. 135–155. DOI: `10.1007/978-3-642-78720-1_6`.

Himmelsbach, J. (2022). „Completion and commissioning of an LVAP ion source.“ Bachelor’s thesis. Ruprecht-Karls-Universität Heidelberg.

Hock, C., J. B. Kim, M. L. Weichman, T. I. Yacovitch, and D. M. Neumark (2012). „Slow photoelectron velocity-map imaging spectroscopy of cold negative ions.“ In: *The Journal of Chemical Physics* 137.24. DOI: `10.1063/1.4772406`.

Howe, J. A. (1963). „Observations on the Maser-Induced Graphite Jet.“ In: *The Journal of Chemical Physics* 39.5, pp. 1362–1363. DOI: `10.1063/1.1734451`.

Irimia, D., D. Dobrikov, R. Kortekaas, H. Voet, D. A. van den Ende, W. A. Groen, and M. H. Janssen (2009). „A short pulse (7 μs FWHM) and high repetition rate (dc-5kHz) cantilever piezovalve for pulsed atomic and molecular beams.“ In: *Review of Scientific Instruments* 80.11. DOI: `10.1063/1.3263912`.

Issler, K., R. Mitrić, and J. Petersen (2023). „Quantum–classical dynamics of vibration-induced autoionization in molecules.“ In: *The Journal of Chemical Physics* 158.3. DOI: `10.1063/5.0135392`.

Jain, N., Á. Kálosi, F. Nuesslein, D. Paul, P. Wilhelm, S. G. Ard, M. Grieser, R. von Hahn, M. C. Heaven, E. Miliordos, D. Maffucci, N. S. Shuman, A. A. Viggiano, A. Wolf, and O. Novotný (2023). „Near-thermo-neutral electron recombination of titanium oxide ions.“ In: *The Journal of Chemical Physics* 158.14. DOI: `10.1063/5.0146365`.

Jalbert, G., R. F. Nascimento, C. R. de Carvalho, C. R. Carvalho, B. F. Magnani, A. C. F. Santos, A. B. Rocha, M. M. Sant’Anna, and N. V. de Castro Faria (2014). „Electron-detachment cross section for CN^- and O_2^- incident on N_2 at intermediate velocities.“ In: *Physical Review A* 89.1, p. 012712. DOI: `10.1103/physreva.89.012712`.

Janssen, M. (2021). *User manual 2021.2: Amsterdam Cantilever Piezo Valve ACPV2/ACPV3 Electronic Driver Unit EDU5-200V*. MassSpecpecD BV, the Netherlands.

Jensen, M. J., U. V. Pedersen, and L. H. Andersen (2000). „Stability of the Ground State Vinylidene Anion H_2CC^-.“ In: *Physical Review Letters* 84.6, pp. 1128–1131. DOI: `10.1103/physrevlett.84.1128`.

Jerosimić, S. V., F. A. Gianturco, and R. Wester (2018). „Associative detachment (AD) paths for H and CN^- in the gas-phase: astrophysical implications.“ In: *Physical Chemistry Chemical Physics* 20.8, pp. 5490–5500. DOI: `10.1039/c7cp05573k`.

Jin, C., R. L. Hettich, R. N. Compton, A. Tuinman, A. Derecskei-Kovacs, D. S. Marynick, and B. I. Dunlap (1994). „Attachment of Two Electrons to $C_{60}F_{48}$: Coulomb Barriers in Doubly Charged Anions.“ In: *Physical Review Letters* 73.21, pp. 2821–2824. DOI: `10.1103/physrevlett.73.2821`.

Jochim, B., B. Berry, T. Severt, P. Feizollah, M. Zohrabi, K. R. P., E. Wells, K. D. Carnes, and I. Ben-Itzhak (2019). „Dependence on the Initial Configuration of Strong Field-Driven Isomerization of C2H2 Cations and Anions.“ In: *The Journal of Physical Chemistry Letters* 10.10, pp. 2320–2327. DOI: `10.1021/acs.jpclett.9b00520`.

Kálosi, Á., M. Grieser, R. von Hahn, U. Hechtfischer, C. Krantz, H. Kreckel, D. Müll, D. Paul, D. W. Savin, P. Wilhelm, A. Wolf, and O. Novotný (2022). „Laser Probing of the Rotational Cooling of Molecular Ions by Electron Collisions.“ In: *Physical Review Letters* 128.18, p. 183402. DOI: `10.1103/physrevlett.128.183402`.

Kandula, D. Z., C. Gohle, T. J. Pinkert, W. Ubachs, and K. S. E. Eikema (2010). „Extreme Ultraviolet Frequency Comb Metrology.“ In: *Physical Review Letters* 105.6, p. 063001. DOI: `10.1103/physrevlett.105.063001`.

Karthein, J. (2015). „Preparatory studies for laser experiments on cold metal clusters at the CSR.“ Bachelor’s thesis. Ruprecht-Karls-Universität Heidelberg.

Kebarle, P. and U. H. Verkerk (2009). „Electrospray: From ions in solution to ions in the gas phase, what we know now.“ In: *Mass Spectrometry Reviews* 28.6, pp. 898–917. DOI: `10.1002/mas.20247`.

Kumar, S. S., D. Hauser, R. Jindra, T. Best, Š. Roučka, W. D. Geppert, T. J. Millar, and R. Wester (2013). „Photodetachment as a destruction mechanism for CN^- and C_3N^- anions in circumstellar envelopes.“ In: *The Astrophysical Journal* 776.1, p. 25. DOI: `10.1088/0004-637x/776/1/25`.

Laufer, A. H. (1980). „An excited state of acetylene: Photochemical and spectroscopic evidence.“ In: *The Journal of Chemical Physics* 73.1, pp. 49–52. DOI: `10.1063/1.439846`.

Levin, J., H. Feldman, A. Baer, D. Ben-Hamu, O. Heber, D. Zajfman, and Z. Vager (1998). „Study of Unimolecular Reactions by Coulomb Explosion Imaging: The Nondecaying Vinylidene.“ In: *Physical Review Letters* 81.16, pp. 3347–3350. DOI: `10.1103/physrevlett.81.3347`.

Li, Z., L. Inhester, C. Liekhus-Schmaltz, B. F. E. Curchod, J. W. Snyder, N. Medvedev, J. Cryan, T. Osipov, S. Pabst, O. Vendrell, P. Bucksbaum, and T. J. Martinez (2017). „Ultrafast isomerization in acetylene dication after carbon K-shell ionization.“ In: *Nature Communications* 8.1. DOI: `10.1038/s41467-017-00426-6`.

Linstrom, P. (1997). *NIST Chemistry WebBook, NIST Standard Reference Database 69*. en. Accessed on 06.01.2024. DOI: `10.18434/T4D303`.

Luna, H., S. D. Magalhães, J. C. Acquadro, M. H. P. Martins, W. M. S. Santos, G. Jalbert, L. F. S. Coelho, and N. V. de Castro Faria (2001). „Electron detachment of Si^- by He, Ne, and Ar.“ In: *Physical Review A* 63.2, p. 022705. DOI: `10.1103/physreva.63.022705`.

Luria, K., W. Christen, and U. Even (2011). „Generation and Propagation of Intense Supersonic Beams.“ In: *The Journal of Physical Chemistry A* 115.25, pp. 7362–7367. DOI: `10.1021/jp201342u`.

Lutey, A. H. A. (2013). „An improved model for nanosecond pulsed laser ablation of metals.“ In: *Journal of Applied Physics* 114.8. DOI: 10.1063/1.4818513.

Makarov, A. A., A. L. Malinovsky, and E. A. Ryabov (2012). „Intramolecular vibrational redistribution: from high-resolution spectra to real-time dynamics.“ In: *Physics-Uspekhi* 55.10, pp. 977–1007. DOI: 10.3367/ufne.0182.201210e.1047.

Meija, J., T. B. Coplen, M. Berglund, W. A. Brand, P. D. Bièvre, M. Gröning, N. E. Holden, J. Irrgeher, R. D. Loss, T. Walczyk, and T. Prohaska (2016). „Isotopic compositions of the elements 2013 (IUPAC Technical Report).“ In: *Pure and Applied Chemistry* 88.3, pp. 293–306. DOI: 10.1515/pac-2015-0503.

Mendenhall, M., A. Barnes, P. Bunton, R. Haglund, L. Hudson, R. Rosenberg, D. Russell, J. Sarnthein, P. Savundararaj, N. Tolk, and J. Tellinghuisen (1988). „Ultraviolet spectroscopy of CN^- in alkali halides: Dynamics of the metastable triplet state.“ In: *Chemical Physics Letters* 147.1, pp. 59–64. DOI: 10.1016/0009-2614(88)80224-0.

Menk, S., P. Bertier, Y. Enomoto, T. Masunaga, T. Majima, Y. Nakano, and T. Azuma (2018). „A cryogenic linear ion trap beamline for providing keV ion bunches.“ In: *Review of Scientific Instruments* 89.11. DOI: 10.1063/1.5051044.

Menk, S., S. Das, K. Blaum, M. W. Froese, M. Lange, M. Mukherjee, R. Repnow, D. Schwalm, R. von Hahn, and A. Wolf (2014). „Vibrational autodetachment of sulfur hexafluoride anions at its long-lifetime limit.“ In: *Physical Review A* 89.2, p. 022502. DOI: 10.1103/physreva.89.022502.

Meyer, C., A. Becker, K. Blaum, C. Breitenfeldt, S. George, J. Göck, M. Grieser, F. Grussie, E. Guerin, R. von Hahn, P. Herwig, C. Krantz, H. Kreckel, J. Lion, S. Lohmann, P. Mishra, O. Novotný, A. O'Connor, R. Repnow, S. Saurabh, D. Schwalm, L. Schweikhard, K. Spruck, S. S. Kumar, S. Vogel, and A. Wolf (2017). „Radiative Rotational Lifetimes and State-Resolved Relative Detachment Cross Sections from Photodetachment Thermometry of Molecular Anions in a Cryogenic Storage Ring.“ In: *Physical Review Letters* 119.2, p. 023202. DOI: 10.1103/physrevlett.119.023202.

Meyer, J. (2014). „Spin and orbital contributions to the magnetic moment of isolated transition metal clusters and complexes.“ PhD thesis. Technische Universität Kaiserslautern.

Middleton, R. (1983). „A versatile high intensity negative ion source.“ In: *Nuclear Instruments and Methods in Physics Research* 214.2-3, pp. 139–150. DOI: 10.1016/0167-5087(83)90580-x.

Middleton, R., J. Klein, and D. Fink (1989). „A CO_2 negative ion source for ^{14}C dating.“ In: *Nuclear Instruments and Methods in Physics Research Section B: Beam Interactions with Materials and Atoms* 43.2, pp. 231–239. DOI: 10.1016/0168-583x(89)90043-8.

Middleton, R. (1989). „A negative-ion cookbook.“ In: *University of Pennsylvania, unpublished.*

Miliordos, E. (2023). *Private communications.*

Millar, T. J., C. Walsh, and T. A. Field (2017). „Negative Ions in Space.“ In: *Chemical Reviews* 117.3, pp. 1765–1795. DOI: 10.1021/acs.chemrev.6b00480.

Mishra, P. M., K. Blaum, C. Breitenfeldt, S. George, J. Göck, M. Grieser, R. von Hahn, J. Karthein, T. Kolling, C. Krantz, H. Kreckel, S. Kumar, J. Mohrbach, G. Niedner-Schatteburg, C. Meyer, R. Repnow, L. Schweikard, and A. Wolf (2015). „An ion source platform of the cryogenic storage ring (CSR).“ In: *Journal of Physics: Conference Series* 635.11, p. 112061. DOI: 10.1088/1742-6596/635/11/112061.

Mishra, P., K. Blaum, S. George, M. Grieser, and A. Wolf (2018). „Transfer matrix calculation for ion optical elements using real fields.“ In: *Nuclear Instruments and Methods in Physics Research Section A: Accelerators, Spectrometers, Detectors and Associated Equipment* 885, pp. 124–133. DOI: 10.1016/j.nima.2017.11.057.

Mishra, P. M. (2019). *Private communications.*

Müll, D., F. Grussie, K. Blaum, S. George, J. Göck, M. Grieser, R. von Hahn, Z. Harman, Á. Kálosi, C. H. Keitel, C. Krantz, C. Lyu, O. Novotný, F. Nuesslein, D. Paul, V. C. Schmidt, S. Singh, S. S. Kumar, X. Urbain, A. Wolf, and H. Kreckel (2021). „Metastable states of Si^- observed in a cryogenic storage ring.“ In: *Physical Review A* 104.3, p. 032811. DOI: 10.1103/physreva.104.032811.

Müll, D. (2023). „Photodetachment studies of negative ions at the Cryogenic Storage Ring.“ PhD thesis. DOI: 10.11588/HEIDOK.00032839.

Najeeb, P. K., M. H. Stockett, E. K. Anderson, M. K. Kristiansson, P. Reinhed, A. Simonsson, S. Rosén, R. D. Thomas, K. C. Chartkunchand, H. Gnaser, R. Golser, D. Hanstorp, Å. Larson, H. Cederquist, H. T. Schmidt, and H. Zettergren (2023). „Stability and Cooling of the C_7^{2-} Dianion.“ In: *Physical Review Letters* 131.11, p. 113003. DOI: 10.1103/physrevlett.131.113003.

Nakano, Y., Y. Enomoto, T. Masunaga, S. Menk, P. Bertier, and T. Azuma (2017). „Design and commissioning of the RIKEN cryogenic electrostatic ring (RICE).“ In: *Review of Scientific Instruments* 88.3. DOI: 10.1063/1.4978454.

Nascimento, R. F., S. L. A. Mello, B. F. Magnani, M. M. Sant’Anna, G. Jalbert, and N. V. de Castro Faria (2013). „Total detachment cross sections of C^-, CH^-, C_2^- and C_2H^- at keV energies.“ In: *Physical Review A* 87.6, p. 062704. DOI: 10.1103/physreva.87.062704.

Novotný, O., P. Wilhelm, D. Paul, Á. Kálosi, S. Saurabh, A. Becker, K. Blaum, S. George, J. Göck, M. Grieser, F. Grussie, R. von Hahn, C. Krantz, H. Kreckel, C. Meyer, P. M. Mishra, D. Muell, F. Nuesslein, D. A. Orlov, M. Rimmler, V. C. Schmidt, A. Shornikov, A. S. Terekhov, S. Vogel, D. Zajfman, and A. Wolf (2019). „Quantum-state–selective electron recombination studies suggest enhanced abundance of primordial HeH^+.“ In: *Science* 365.6454, pp. 676–679. DOI: 10.1126/science.aax5921.

Nüsslein, F. (2018). „An experimental setup for testing ion beam sources for the CSR facility.“ Master’s thesis. Ruprecht-Karls-Universität Heidelberg.

O’Connor, A. P., A. Becker, K. Blaum, C. Breitenfeldt, S. George, J. Göck, M. Grieser, F. Grussie, E. A. Guerin, R. von Hahn, U. Hechtfischer, P. Herwig, J. Karthein, C.

Krantz, H. Kreckel, S. Lohmann, C. Meyer, P. M. Mishra, O. Novotný, R. Repnow, S. Saurabh, D. Schwalm, K. Spruck, S. Sunil Kumar, S. Vogel, and A. Wolf (2016). „Photodissociation of an Internally Cold Beam of CH^+ Ions in a Cryogenic Storage Ring.“ In: *Physical Review Letters* 116.11, p. 113002. DOI: `10.1103/physrevlett.116.113002`.

Oetjens, A. (2022). „Planning and Testing the Laser Beam Transfer Line at CSR.“ Master's thesis. Ruprecht-Karls-Universität Heidelberg.

Osterwalder, A., M. J. Nee, J. Zhou, and D. M. Neumark (2004). „High resolution photodetachment spectroscopy of negative ions via slow photoelectron imaging.“ In: *The Journal of Chemical Physics* 121.13, pp. 6317–6322. DOI: `10.1063/1.1787491`.

Paul, D., M. Grieser, F. Grussie, R. von Hahn, L. W. Isberner, Á. Kálosi, C. Krantz, H. Kreckel, D. Müll, D. A. Neufeld, D. W. Savin, S. Schippers, P. Wilhelm, A. Wolf, M. G. Wolfire, and O. Novotný (2022). „Experimental Determination of the Dissociative Recombination Rate Coefficient for Rotationally Cold CH^+ and Its Implications for Diffuse Cloud Chemistry.“ In: *The Astrophysical Journal* 939.2, p. 122. DOI: `10.3847/1538-4357/ac8e02`.

Pedersen, U. V., M. Hyde, S. P. Møller, and T. Andersen (2001). „Lifetime measurement of He^- utilizing an electrostatic ion storage ring.“ In: *Physical Review A* 64.1, p. 012503. DOI: `10.1103/physreva.64.012503`.

Pegg, D. J. (2004). „Structure and dynamics of negative ions.“ In: *Reports on Progress in Physics* 67.6, pp. 857–905. DOI: `10.1088/0034-4885/67/6/r02`.

Planck, M. (1901). „Ueber das Gesetz der Energieverteilung im Normalspectrum.“ In: *Annalen der Physik* 309.3, pp. 553–563. DOI: `10.1002/andp.19013090310`.

Plaß, W. R., T. Dickel, and C. Scheidenberger (2013). „Multiple-reflection time-of-flight mass spectrometry.“ In: *International Journal of Mass Spectrometry* 349-350, pp. 134–144. DOI: `10.1016/j.ijms.2013.06.005`.

Repp, J. M. A. (2012). „The setup of the high-precision Penning-trap mass spectrometer PENTATRAP and first production studies of highly charged ions.“ PhD thesis. DOI: `10.11588/HEIDOK.00013994`.

Ridgway, S. T., D. N. B. Hall, S. G. Kleinmann, D. A. Weinberger, and R. S. Wojslaw (1976). „Circumstellar acetylene in the infrared spectrum of IRC +10° 216.“ In: *Nature* 264.5584, pp. 345–346. DOI: `10.1038/264345a0`.

Rienstra-Kiracofe, J. C., G. S. Tschumper, H. F. Schaefer, S. Nandi, and G. B. Ellison (2002). „Atomic and molecular electron affinities: photoelectron experiments and theoretical computations.“ In: *Chemical reviews* 102.1, pp. 231–282. DOI: `10.1021/cr990044u`.

Roberts, T. (2013). „G4Beamline user's guide.“ In: *Muons, Inc*, pp. 3468–3470.

Schaefer, H. F. (1979). „The 1,2 hydrogen shift: a common vehicle for the disappearance of evanescent molecular species.“ In: *Accounts of Chemical Research* 12.8, pp. 288–296. DOI: `10.1021/ar50140a004`.

Schippers, S., E. Sokell, F. Aumayr, H. Sadeghpour, K. Ueda, I. Bray, K. Bartschat, A. Murray, J. Tennyson, A. Dorn, M. Yamazaki, M. Takahashi, N. Mason, O. Novotný,

A. Wolf, L. Sanche, M. Centurion, Y. Yamazaki, G. Laricchia, C. M. Surko, J. Sullivan, G. Gribakin, D. W. Savin, Y. Ralchenko, R. Hoekstra, and G. O'Sullivan (2019). „Roadmap on photonic, electronic and atomic collision physics: II. Electron and antimatter interactions." In: *Journal of Physics B: Atomic, Molecular and Optical Physics* 52.17, p. 171002. DOI: 10.1088/1361-6455/ab26e0.

Schmidt, H. T., G. Eklund, K. C. Chartkunchand, E. K. Anderson, M. Kamińska, N. de Ruette, R. D. Thomas, M. K. Kristiansson, M. Gatchell, P. Reinhed, S. Rosén, A. Simonsson, A. Källberg, P. Löfgren, S. Mannervik, H. Zettergren, and H. Cederquist (2017). „Rotationally Cold OH^- Ions in the Cryogenic Electrostatic Ion-Beam Storage Ring DESIREE." In: *Physical Review Letters* 119.7, p. 073001. DOI: 10.1103/physrevlett.119.073001.

Schmidt, H. T., R. D. Thomas, M. Gatchell, S. Rosén, P. Reinhed, P. Löfgren, L. Brännholm, M. Blom, M. Björkhage, E. Bäckström, J. D. Alexander, S. Leontein, D. Hanstorp, H. Zettergren, L. Liljeby, A. Källberg, A. Simonsson, F. Hellberg, S. Mannervik, M. Larsson, W. D. Geppert, K. G. Rensfelt, H. Danared, A. Paál, M. Masuda, P. Halldén, G. Andler, M. H. Stockett, T. Chen, G. Källersjö, J. Weimer, K. Hansen, H. Hartman, and H. Cederquist (2013). „First storage of ion beams in the Double Electrostatic Ion-Ring Experiment: DESIREE." In: *Review of Scientific Instruments* 84.5. DOI: 10.1063/1.4807702.

Schmidt, V. C. (2018). „Design of an ion beam extraction optics and analysis of the molecular composition of an ion beam in an electrostatic storage ring." Bachelor's thesis. Ruprecht-Karls-Universität Heidelberg.

Schork, R. and H. Köppel (2001). „Barrier recrossing in the vinylidene–acetylene isomerization reaction: A five-dimensional ab initio quantum dynamical investigation." In: *The Journal of Chemical Physics* 115.17, pp. 7907–7923. DOI: 10.1063/1.1405120.

Schotsch, F.-F. (2021). „TrapREMI - Development of a Reaction Microscope inside a Zajfman Trap and First Photodissociation Experiments on Stored Molecular Ions." PhD thesis. DOI: 10.11588/HEIDOK.00029402.

Schuurman, M. S. and V. Blanchet (2022). „Time-resolved photoelectron spectroscopy: the continuing evolution of a mature technique." In: *Physical Chemistry Chemical Physics* 24.34, pp. 20012–20024. DOI: 10.1039/d1cp05885a.

Seiersen, K. (2003). „Electron Scattering on Positive and Negative Ions Studied in Heavy Ion Storage Rings." PhD thesis. University of Aarhus, Denmark.

Simpson, M., M. Nötzold, A. Schmidt-May, T. Michaelsen, B. Bastian, J. Meyer, R. Wild, F. A. Gianturco, M. Milovanović, V. Kokoouline, and R. Wester (2020). „Threshold photodetachment spectroscopy of the astrochemical anion CN^-." In: *The Journal of Chemical Physics* 153.18, p. 184309. DOI: 10.1063/5.0029841.

Singh, R. P., S. Kumar, S. Dubey, and A. Singh (2021). „A review on working and applications of oxy-acetylene gas welding." In: *Materials Today: Proceedings* 38, pp. 34–39. DOI: 10.1016/j.matpr.2020.05.521.

Skell, P. S., J. E. Villaume, and F. A. Fagone (1972). „Formation of vinylidene intermediates in the reaction of diatomic carbon with propylene.“ In: *Journal of the American Chemical Society* 94.22, pp. 7866–7867. DOI: 10.1021/ja00777a033.

Spruck, K., A. Becker, F. Fellenberger, M. Grieser, R. von Hahn, V. Klinkhamer, O. Novotný, S. Schippers, S. Vogel, A. Wolf, and C. Krantz (2015). „An efficient, movable single-particle detector for use in cryogenic ultra-high vacuum environments.“ In: *Review of Scientific Instruments* 86.2. DOI: 10.1063/1.4907352.

Stockett, M. H., J. N. Bull, J. T. Buntine, E. Carrascosa, E. K. Anderson, M. Gatchell, M. Kaminska, R. F. Nascimento, H. Cederquist, H. T. Schmidt, et al. (2020). „Radiative cooling of carbon cluster anions C_{2n+1}^{-} (n = 3–5).“ In: *The European Physical Journal D* 74, pp. 1–9. DOI: 10.1140/epjd/e2020-10052-5.

Suits, B. H. (2023). *Electronics for Physicists: An Introduction.* Springer International Publishing. DOI: 10.1007/978-3-031-36364-1.

Tremblay, M. E., B. W. Smith, M. B. Leong, and J. D. Winefordner (1987). „Laser Ablation for the Introduction of Solid Metals into an Inductively Coupled Plasma.“ In: *Spectroscopy Letters* 20.4, pp. 311–318. DOI: 10.1080/00387018708081552.

Vector Fields (2004). „Opera-3d reference manual.“ In: *Vector Fields Limited, England* 3010.10.

Wang, M., W. Huang, F. Kondev, G. Audi, and S. Naimi (2021). „The AME 2020 atomic mass evaluation (II). Tables, graphs and references.“ In: *Chinese Physics C* 45.3, p. 030003. DOI: 10.1088/1674-1137/abddaf.

Weber, J. M. (2005). „A pulsed ion source for the preparation of metal containing cluster anions using supersonic entrainment of laser vaporized metal.“ In: *Review of Scientific Instruments* 76.4. DOI: 10.1063/1.1889430.

Weichman, M. L. and D. M. Neumark (2018). „Slow Photoelectron Velocity-Map Imaging of Cryogenically Cooled Anions.“ In: *Annual Review of Physical Chemistry* 69.1, pp. 101–124. DOI: 10.1146/annurev-physchem-050317-020808.

Wilhelm, P. U. (2019). „First Studies of Low-Energy Electron Cooling of keV Energy Ion Beams at the Electrostatic Cryogenic Storage Ring CSR.“ PhD thesis. DOI: 10.11588/HEIDOK.00026821.

Wolf, B. (1995). *Handbook of ion sources.* CRC press.

Yang, L., H. Gao, J. Zhou, and C. Ng (2015). „Vacuum ultraviolet laser photoion and pulsed field ionization–photoion study of Rydberg series of chlorine atoms prepared in the $^2\mathrm{P}_\mathrm{J}$ (J = 3/2 and 1/2) fine-structure states.“ In: *The Astrophysical Journal* 810.2, p. 132. DOI: 10.1088/0004-637x/810/2/132.

Zettergren, H., A. Domaracka, T. Schlathölter, P. Bolognesi, S. Díaz-Tendero, M. Łabuda, S. Tosic, S. Maclot, P. Johnsson, A. Steber, D. Tikhonov, M. C. Castrovilli, L. Avaldi, S. Bari, A. R. Milosavljević, A. Palacios, S. Faraji, D. G. Piekarski, P. Rousseau, D. Ascenzi, C. Romanzin, E. Erdmann, M. Alcamí, J. Kopyra, P. Limão-Vieira, J. Kočišek, J. Fedor, S. Albertini, M. Gatchell, H. Cederquist, H. T. Schmidt, E. Gruber, L. H. Andersen, O. Heber, Y. Toker, K. Hansen, J. A. Noble, C. Jouvet, C. Kjær, S. B. Nielsen, E. Carrascosa, J. Bull, A. Candian, and

A. Petrignani (2021). „Roadmap on dynamics of molecules and clusters in the gas phase.“ In: *The European Physical Journal D* 75.5. DOI: `10.1140/epjd/s10053-021-00155-y`.

Zou, S., J. M. Bowman, and A. Brown (2003). „Full-dimensionality quantum calculations of acetylene–vinylidene isomerization.“ In: *The Journal of Chemical Physics* 118.22, pp. 10012–10023. DOI: `10.1063/1.1571520`.

Danksagung

An dieser Stelle möchte ich mich bei allen Menschen bedanken, die zum Gelingen dieser Arbeit beigetragen haben. Ich danke …

- … **Prof. Dr. Klaus Blaum** für die Möglichkeit, diese Arbeit am MPIK anfertigen zu dürfen und die kurzfristige Bereitstellung eines Ersatzlasers für die Strahlzeit.
- … **apl. Prof. Dr. Andreas Wolf** für die ausgezeichnete fachliche Betreuung und die vielen sehr lehr- und hilfreichen Kommentare.
- … **Dr. Oldřich Novotný** für die exzellente Betreuung und die vielen hilfreichen Gespräche und Kommentare.
- … dem Techniker-Team rund um **Manfred König** und **Max Trebis**. Ohne Euch hätte die Arbeit in der Experimentierhalle nur einen Bruchteil so viel Spaß gemacht!
- … **Dirk Kaiser** für die technische Unterstützung und die vielen netten Gespräche.
- … den Konstruktions- und Werkstatt-Teams rund um **Thorsten Spranz**, **Christian Kaiser** und **Frank Müller** für die umfangreiche technische Unterstützung.
- … **Jannis Himmelsbach** für die tatkräftige Unterstützung des LVAP-Projektes.
- … **Viviane Schmidt** und **Dr. Damian Müll** für die angenehme Büroatmosphäre, die netten und lehrreichen Gespräche und die Unterstützung bei der Strahlzeit.
- … meinen anderen Kolleg:innen für die schöne Zeit am Institut und die Unterstützung: **Aigars Znotiņš**, **Leonard Isberner**, **Dr. Florian Grussie**, **Dr. Lisa Gamer**, **Dr. Manfred Grieser**, **Dr. Daniel Paul** und **Lukas Berger**
- … meinen Freunden nah und fern, die mich auf manchen oder allen Wegabschnitten zur fertigen Arbeit begleitet haben: **Roman**, **Julia**, **Markus**, **Lennart**, **Lukas**, **Chris**, **Sebastian**, **Marta**, **Nica** und **Viktoria**
- … meiner Freundin **Shafigheh** für den seelischen Rückhalt beim Schreiben.
- … meinen Geschwistern **Nicolas** und **Jonas** für die schöne Zeit und die Unterstützung.
- … meinen Eltern **Thomas** und **Gertraud** für die jahrelange, bedingungslose und uneingeschränkte Unterstützung.